

POLITECNICO DI TORINO

**Master's degree
in Biomedical Engineering**

Master's thesis

**Preliminary steps of validation of a vertebral
finite element model including a subject-
specific cortical compartment.**



Supervisor:

Prof.ssa Cristina Bignardi

Master student:

Alessandra Degan Di Dieco

Co-supervisors:

Ing. Fulvia Taddei
Ing. Enrico Schileo

A.A. 2019/2020

Table of contents

Abstract	1
Introduction.....	3
1 Elements of anatomy of the vertebral column	6
1.1 Structure and functions of the spine.....	6
1.2 Structure of the vertebrae	8
1.3 Classification of the vertebral fractures.....	10
1.4 Metastatic spinal lesions and fracture risk	16
1.5 SINS (Spine Instability Neoplastic Score).....	18
2 Background and aims	23
2.1 FE models for intact vertebra.....	23
2.1.1 Patient-specific cortical layer or constant shell.....	25
2.1.2 Material properties	27
2.1.3 Experimental set-ups.....	28
2.2 Metastatic vertebrae models.....	31
2.3 qSINS project overview and aims of the current work	34
3 Material and methods.....	36
3.1 Towards the 3D FE-model	36
3.1.1 Available specimens	37
3.1.2 Images acquisition	38
3.1.3 Segmentation	40
3.1.4 Estimation of the vertebral cortical bone properties.....	41
3.1.5 Patches and NURBS construction	64
3.1.6 Mesh generation	65
3.1.7 Assignment of material properties	68
3.1.8 Cortical and trabecular transversal isotropy	72
3.2 Experimental set up	74
3.2.1 Specimen preparation.....	74
3.2.2 Mechanical testing.....	75
3.2.3 Experimental data recordings	75

3.3	Boundary conditions of the model	76
3.3.1	Registration of the experimental and model reference systems	76
3.3.2	Loading and constraint conditions	77
3.4	Comparison between CBM-model and Shell-model	79
3.5	Polyurethane model	81
4	Results and discussion	83
4.1	Comparison of the CBM-Model with the Shell-Model	84
4.2	CBM-model and Polyurethane model: FE analysis results	90
4.3	DIC data analysis.....	97
4.4	Check of the applied boundary conditions: preliminary validation of the PU model101	
5	Conclusions and future attempts	105
	References.....	108

Abstract

Vertebral metastases affect one third of metastatic patients. They compromise bone integrity, often leading to fracture and neurological damage. The risk of fracture of a metastatic vertebra is currently estimated by the Spinal Instability Neoplastic Score (SINS). However, SINS is mostly qualitative, and lacks assessment of vertebral mechanics. The present thesis is part of the qSINS (i.e. quantitative SINS) project, conceived at the Bioengineering and Computing (BIC) Laboratory of IRCSS Istituto Ortopedico Rizzoli, and funded by the Italian Ministry of Health (RF-2016-02364359). The main challenge of qSINS is to develop subject-specific finite elements (SSFE) models based on computed tomography (CT) images routinely collected to stage the disease. In fact, no reliable SSFE model is available in the literature to quantify the reduction of metastatic vertebral strength over intact conditions. Preliminary studies within the qSINS project identified the modelling of cortical compartment, and a more realistic load distribution over the vertebral endplate as two key modelling steps. Consequently:

- the first aim of this thesis was to develop a SSFE model with a patient-specific cortical layer (CBM-model), using estimates of cortical bone thickness and density from clinical CT images; to assess how a subject-specific cortical compartment influenced stiffness, strain and strength, the CBM-model was compared with a literature-based model that mimicked the cortical bone with a uniform shell;
- the second aim, linked to the currently starting qSINS validation experiment, was to verify the correctness of the model replication of boundary conditions; to exclude the effect of bone inhomogeneity, a polyurethane replica of the vertebra was built, tested and modelled;

- the third aim was to compare SSFE computed displacements and strains with those measured on cadaver vertebrae by Digital Image Correlation technique.

The first goal achieved was the realization of the vertebral model with a patient-specific cortical compartment and the assessment of the significant mechanical role of the latter, compared with a uniform and thin shell. The second one was the development of the whole validation procedure, in order to compare the experimental and the finite element (FE) data, obtained from the mechanical tests and the numerical simulations respectively. During the analysis of the experimental data, a recurrent offset was identified, i.e. we observed a non-zero value of displacement where the vertebra and the polyurethane replica were embedded. Waiting to understand the origin of this noise on the data, a first attempt was made to validate the polyurethane model. A good correlation between the experimental and SSFE data was found ($R^2 = 0.75$).

Introduction

The spine commonly hosts bone metastases, originating from lung, prostate, kidney, breast cancers. These lesions often lead to vertebral fractures, because of the lack of structural integrity and bone quality of the metastatic vertebrae[1], and, as a consequence, to neurological damages too. A patient may therefore find himself in a very precarious state of health. He will not only have to face cancer treatments but he will also be forced to rest, with significant pain.

The prediction of the fracture risk could guide the decisions of the specialists for preventive solutions[1] and lengthen both the patient's life expectancy[2] and quality of life. Currently, the instability of the metastatic spine is assessed by the Spinal Instability Neoplastic Score System (SINS). The scores are assigned according to the location of the lesion and other visually assessed geometric parameters, together with other parameters concerning the status of the patient.

In fact, SINS' major drawbacks are its mostly qualitative nature and the absence of any insight into the mechanical behaviour of the metastatic vertebrae [3], which instead is likely to greatly influence the risk of vertebral fracture or neurological damage. This thesis work is part of a three years project, conceived at the Bioengineering and Computing (BIC) Laboratory of the Rizzoli Orthopaedic institute and funded by the Italian Ministry of Health (RF-2016-02364359). The aim of the project is to develop a so-called quantitative SINS (qSINS), in order to overcome the limits of the SINS, defining quantitative parameters for the diagnosis and the treatment of the patient. Among these quantitative parameters, the most advanced ones would be based on subject-specific finite elements models (SSFE). These SSFE are intended to emulate the actual pathological conditions, determining the response of the vertebra to realistic loads, taking into account vertebral anatomy, bone mechanical properties, and the quality of metastatic bone too. A critical analysis of the literature concerning vertebrae models shows that there have been several attempts to model and reproduce

the vertebral mechanics, both in physiological and pathological conditions, but a consensus on validated models has not been reached. The differences among published models deal with both the construction of the models and their validation. For this reason, researchers in the BIC laboratory are exploring different modelling variables, concerning both material and structural properties, in order to develop a robust modelling procedure to estimate stiffness, strains and strength through finite element models, to be eventually compared with experimental results [4].

My thesis project started from the preliminary results about vertebral SSFE modelling already obtained at the BIC lab, and defined some new goals. The aim of this work was to explore subject-specific modelling of cortical compartment and to conduct the preliminary steps of model validation, i.e. the check of the correct identification of experimentally applied boundary conditions and a first comparison of model results against experimental measurements on real vertebrae. The present thesis is structured as follows. After a preliminary excursus on the anatomy of the spine and the classification and characterization of vertebral fractures (Chapter 1), I reported in Chapter 2 the results of a literature analysis about FE models of intact and metastatic vertebrae, highlighting the modelling choices and their possible limits. This review finally led to the definition of the aim of my work, which due to its complexity deserves here a foreword. One of the most debated issues about vertebral SSFE concerns the modelling of the cortical compartment, as the resolution of the computed tomography images, routinely used for the detection and evaluation of metastases, is typically coarser than cortical bone thickness. So, cortical bone is often not explicitly modelled, or mimicked through uniform and a-priori defined layers. Starting from this observation and from the good results previously obtained in the BIC lab on the femur, the **first aim** of my thesis was the construction of a new model with a patient-specific cortical layer. I will refer to this as to “CBM-model”, after the acronym Cortical Bone Mapping, which refers to the image deconvolution algorithm originally developed at the University of Cambridge for the estimate of cortical bone

thickness and density from clinical CT images, and made available as a freeware to the scientific community. To this purpose, I tried firstly to define a robust analysis protocol to estimate density and thickness of the cortical bone; I then proceeded to FE model generation, including the mesh generation, the material properties definition, the assignment of the boundary conditions. To comparatively assess the influence of a subject-specific cortical compartment on the prediction of stiffness, strain and strength of the vertebrae, the CBM-model was compared with one previously developed, in which according to some literature references, a uniform shell had been introduced to mimick cortical bone (Shell-model). Once defined a suitable protocol for FE model generation, the **second aim** of my thesis, linked to the currently starting qSINS validation experiment, was to ensure an accurate model replication of the boundary conditions applied in the experimental tests, so to avoid bias in model validation. As the experimental setup is novel and tries to overcome the limitations of non-physiological end-cap loading through an ideally hydrostatic load application, the replication of boundary condition is not a trivial step and should be carefully devised and checked. To exclude the effect of vertebral bone inhomogeneity on the actual boundary conditions, a polyurethane replica of the vertebra was built and tested. We therefore built a model that reproduced both the geometry and the material properties of the replica, and verified the accuracy in the identification of boundary conditions. The following step was the comparison of the model with the results obtained by the mechanical tests on the first vertebra of the whole experiment (**third aim** of my thesis). For this purpose, we started registering the experimental and the model reference system to align experimental loads and constraints to the model. Finally, we solved the model and compared the results of the simulations, in terms of displacements and strains with those obtained through Digital Image Correlation technique in the experiment. In Chapter 3, all the steps followed to fulfil these aims are described. In Chapters 4 and 5, results, conclusions and some thoughts about future developments are reported.

1 Elements of anatomy of the vertebral column

1.1 Structure and functions of the spine

The vertebral column, also known as spine or backbone, is the main support for the human body. The spine normally consists of thirty-three vertebrae[5].

Twenty-four vertebrae, located in the upper part of the backbone, are articulated with each other by intervertebral discs. These vertebrae could be assigned to different regions; in particular, there are:

- Seven cervical vertebrae (C1-C7)
- Twelve thoracic vertebrae (T1-T12)
- Five lumbar vertebrae (L1-L5).

In the lower part of the spine, instead, five vertebrae are fused in sacrum and the remaining four are fused in the coccyx [6]. In Figure 1, a division of the vertebrae by region is shown.

The articulating vertebrae (C1-L5) are able move independently, contrary to the sacrum and the coccyx. The regions allow also to distinguish the different curves of the spinal column in anteroposterior direction (Figure 1). In the adult, we can recognize:

- A cervical curvature, anteriorly convex
- A thoracic curvature, posteriorly convex
- A lumbar curvature, anteriorly convex
- A pelvic curvature, antero-inferior concave, that involves the sacrum and the coccyx vertebrae.

There are some other curves, but less marked, on the sagittal plane[2]. These curves have both the role of maintenance of stability at each intervertebral joint and to provide more flexibility and shock-absorbing capacity to spine[7].

The human spine, in addition to be a support for the human body, allows the movement of the head and the trunk and the maintenance of the posture, thanks to the inserted joints and the muscles[8]. Another important function is the protection of the spinal cord, contained in the spinal canal, from trauma, due to shocks and vibration in some cases.

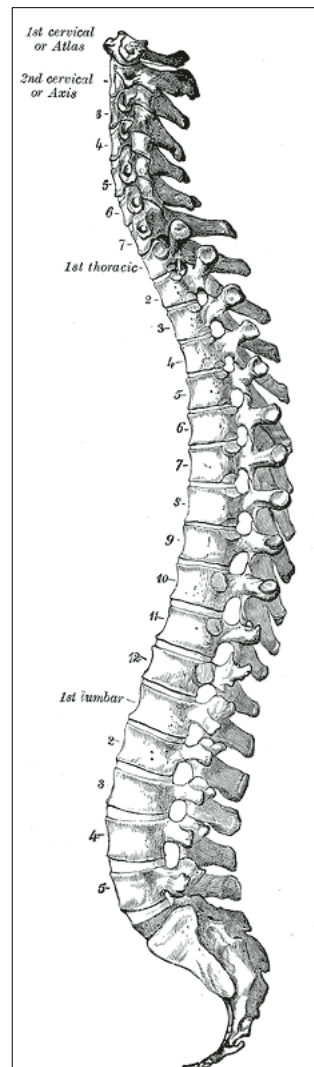


Figure 1: Lateral view of the vertebral column (Henry Gray - Anatomy of the Human Body (1918))

The stability of the spine and the connection between the vertebrae are also guaranteed from the ligaments. The main ones are interspinous ligaments, supraspinous ligaments, intertransverse ligaments, posterior longitudinal ligaments, anterior longitudinal ligaments and ligamentum flavum Figure 2.

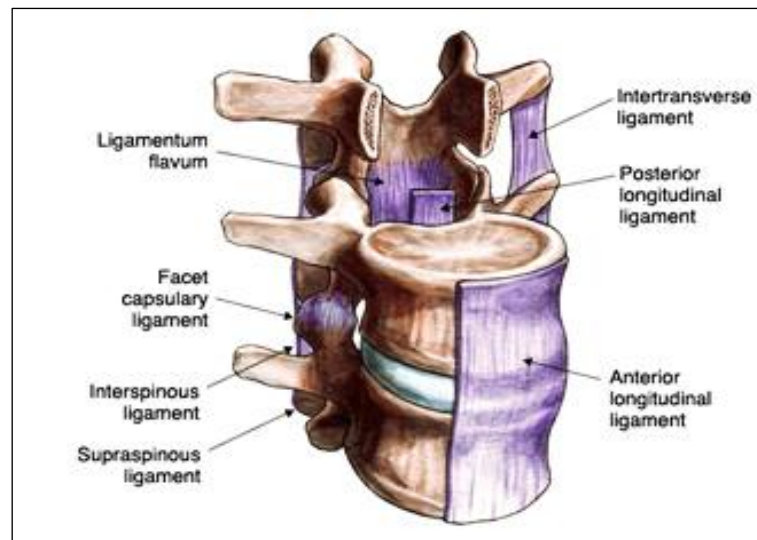


Figure 2: Ligaments extending the vertebral column (<https://www.spineuniverse.com/anatomy/ligaments>)

These ligaments must allow physiological motions and, at the same time, they must limit motions within physiological limits. Another fundamental function is the protection of the spinal cord in the traumatic situations. In these cases, high loads are applied at very high speeds, so the displacement have to be restricted and a lot of energy has to be absorbed and dissipated[7].

1.2 Structure of the vertebrae

The vertebrae are classified as short irregular bones. All the vertebrae are different from each other, but it is possible to identify a typical structure. In particular, the articulating vertebrae of the cervical, thoracic and lumbar regions are substantially similar[9]. Anyway, the size and the mass of the vertebrae increase from the upper part of the spine to the lower one. This feature is linked to the progressive increase of

the loads to which the vertebrae are subjected from the first cervical vertebra to the last lumbar one[7]. The main parts of the vertebra are the vertebral body, anteriorly, and the vertebral arch, in the back of the human body. All the vertebral arches circumscribe the vertebral foramen, that contains the spinal cord, except the vertebrae of the sacrum and the coccyx, which are fused and don't constitute a foramen. The vertebral body is almost cylindrical and it allow to distribute the loads due to the body weight and the movements along the spine axis. This is also guaranteed by the presence of the intervertebral disc, that consists of cartilaginous tissue and allow a complete contact, between adjacent vertebral bodies. It is made of proteoglycans, collagen and elastic fibres. It consists of three parts: the annulus fibrosus, the nucleus pulposus and the cartilaginous end plates. The disc is subjected to many different types of loads[7]. Posteriorly, the vertebral arch, also known as neural arch, consists of two pedicles and two laminae and supports seven processes, as shown in Figure 3.

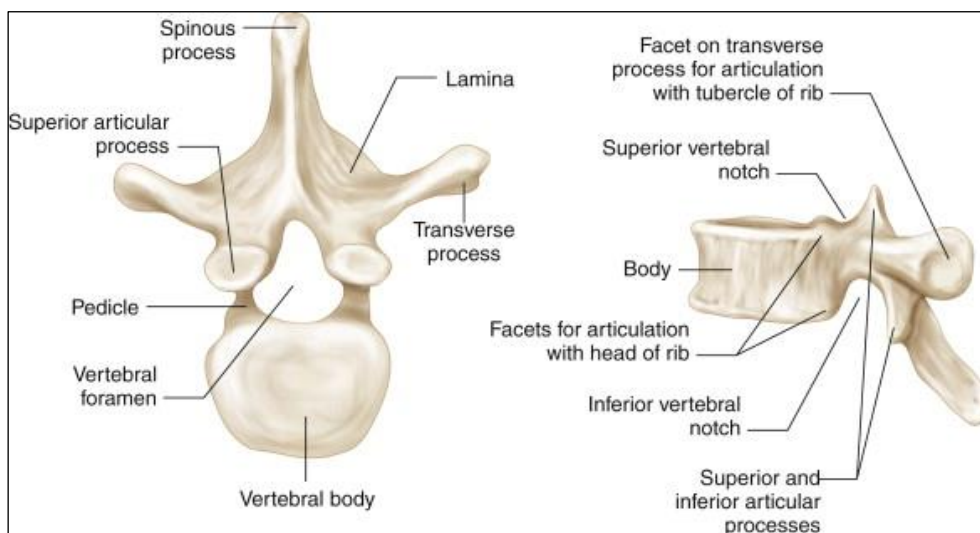


Figure 3: Posterior and lateral view of a vertebra

The processes act as attachment sites for muscles and ligaments. Each vertebra has a spinous process located in the back of the vertebra, in the centre of the arch, and two transverse processes, laterally and posteriorly from the vertebral body. In the thoracic

vertebrae, the transverse processes articulate with the ribs. The pedicles connect the vertebral body to the transverse processes and the laminae connect the transverse and spinous processes. Lastly, thanks to the articular processes, one vertebra can form a joint with the adjacent superior and inferior vertebrae. These processes are located at the intersection of the laminae and pedicles.

1.3 Classification of the vertebral fractures

The spine is a highly complicated structure and, during daily activities, is subjected to complex, dynamic loading conditions. If the vertebral bone was affected from metabolic disorder, such as osteoporosis, or there was a spinal metastasis or following a trauma, a vertebral injury could occur. Osteoporosis is the most common metabolic bone pathology and so it is also one of the main causes of fractures. These injuries are associated with pain, increased mortality and morbidity and decreased quality of life [10]. On the other hand, the spine is one of the most frequent site involved by metastases, associated to a high risk of vertebral fractures [11]. In the past, there have been many attempts to classify the vertebral injuries. The various systems used different features for classification: the inferred mechanisms of injuries, the bone morphology, between distraction and flexions injuries, the neurological status, the anatomic determinants of fracture stability and so on [12], [13]. Anyway, the classification of spinal fractures is fundamental to facilitate communication and allow the realization of an optimal protocol of treatment. In particular, it is possible to classify the fractures of the thoraco-lumbar section of the spine. Nicoll et al. differentiated between stable and non-stable thoracolumbar injuries [14]. On one hand, after a stable fracture, there is an increased degree of deformity and then a crack of the ligaments; on the other hand, after a non-stable fracture, surgery is necessary to reduce the deformity of the ligaments, disrupted because of the trauma. Subsequently, Holdworth et al. presented a different classification, based on

mechanisms of injuries: compression, flexion, extension and flexion-rotation injuries [15]. In 1983, Denis [16] and McAfee [17] introduced the concept of 'three' column, also in the context of thoracolumbar injuries. The Denis' three column system included an anterior column, in which two anterior thirds of the vertebral body and discs are included, a middle column, that consists of the posterior third of the vertebral body and disc including the posterior vertebral body wall and finally a posterior column, which includes the connection of the facet joints on both sides and ligamentous bony complex between the spinal processes[12]. Denis also distinguished major and minor injuries. The latter include spinal process fractures, transverse process fractures, articular process pars inter-articularis fractures. The major fractures are classified in 5 types, indicated by a capital letter: A, B, C, D, E. In the 1990s, a new classification of spine injuries has been presented by the AO Group. They concluded that there was no classification system available and that the Denis three column system had some problems, because the middle column was not an anatomic part but it was only virtual. So, they tried to develop a more logical concept and to provide a classification, not purely mechanistic, but also useful for practical applications [12], [18]. According to Whitesides [19], the AO group based their classification system on three basic functions of a stable spine, that can resist axial distraction forces torsional forces and axial compression forces. Therefore, they distinguished between distraction injuries (Type B), torsional injuries (Type C) and compression injuries (Type A), that represented, respectively, the lengthening, the rotation, the shortening of the spine. The essential characteristics of the three injuries types are resumed in Figure 4. The successive grades, from type A to type C, represent the increasing severity and stability of the injury and the increasing risk of neurological damages [13]. The severity is determined by the amount of the bony, the ligaments lesions, the neurological damage and the mechanical instability. Each type is further divided in three groups. Therefore, they distinguished in nine injury types, which are sub-

divided in totally 27 different injuries. It could be demonstrated that 65% of injuries are Type A injuries, 15% Type B and 20% Type C thoracolumbar injuries [12].

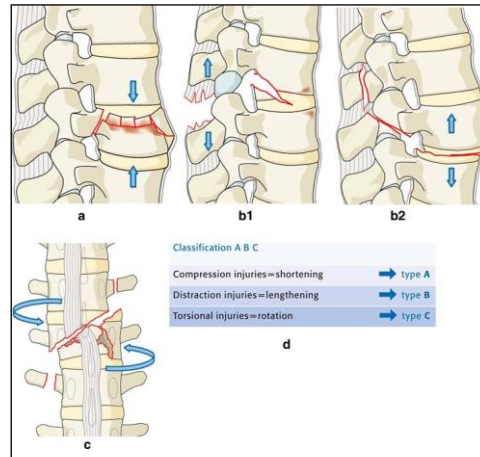


Figure 4: Types of vertebral injuries. a Type A, compression injury of the anterior column. b Type B, two column injury with either posterior or anterior transverse disruption. c Type C, two column injury with rotation. d Classification A B C (according to M. Aebi, V. Arlet, J.K. Webb, in AO-Manual of Spine Surgery, Vol. I, 2008. Thieme Publisher, Stuttgart)

Finally, this classification, proposed by Magerl et al. [18], is systematic and detailed; however, it doesn't take into consideration some other clinical features that could guide the decisions of the surgeon and also about the treatment. Another proposed classification system is the thoracolumbar injury classification system (TLICS). In contrast to the Magerl system, the TLICS uses descriptive categories, considering the neurological status, the integrity of the posterior ligamentous complex (PLC) and the injury morphology. TLICS includes a scoring system, by which it's possible to associate a rank to the morphology, the PLC integrity and the neurologic status. These ranks constitute a total score, thank to which it's possible to choose between different surgical solutions. This system has some flaw, too [13]. In 2013, the Magerl classification has been revised from a workgroup of the AOSpine, i.e. AOSpine Classification Group, in order to assess the reliability and accuracy and to reach the unanimous consensus regarding classification details and applicability. For this purpose, the group carried on different evaluation sessions.

Finally, 3 parameters have been identified for the classification of the fractures:

- Morphology
- Neurological status
- Clinical modifiers

The morphologic classification includes 3 types of fractures (A, B, C), according to the ascending severity[13]. Type A includes compression injuries and may affect a single vertebra or occur with type B or C. The type A fracture also includes 5 subtypes. Type B injuries also includes 3 subtype but these fracture affect anterior or posterior tension band. Lastly, type C causes the failure of all elements. This leads to dislocation and displacement beyond physiological limits of the cranial and caudal parts in any plane. This type of injuries could also produce complete disruption of the soft tissues and separation of the vertebral elements. An overview of the different type of injuries is shown in the following figures.

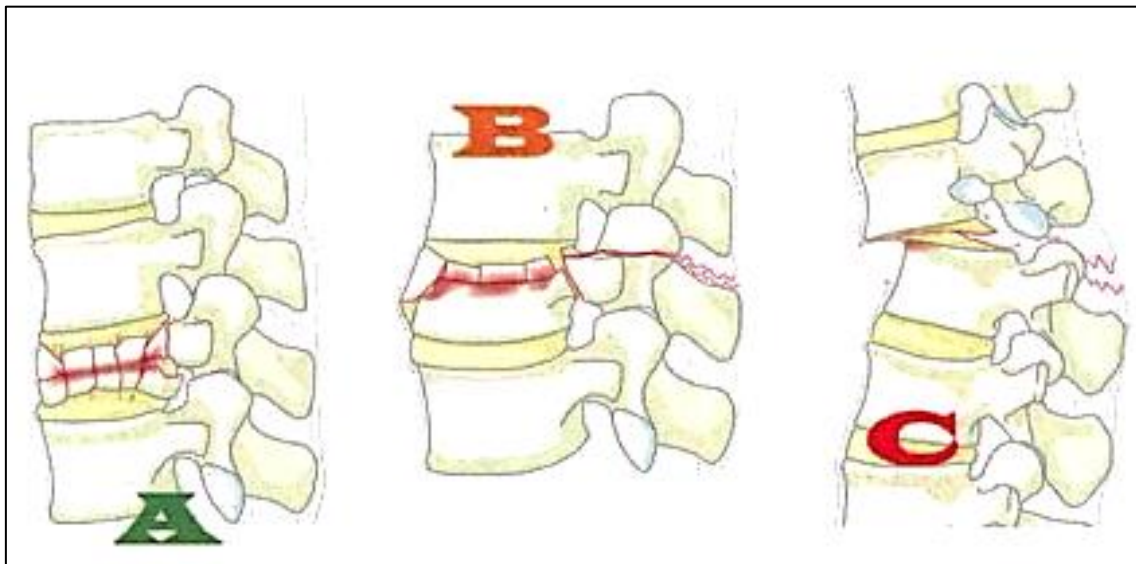


Figure 5: 3 basic types. Type A: compression injuries. Failure of anterior structures under compression with intact tension band. Type B: Failure of the posterior or anterior tension band. Type C: Failure of all elements leading to dislocation or displacement [13].

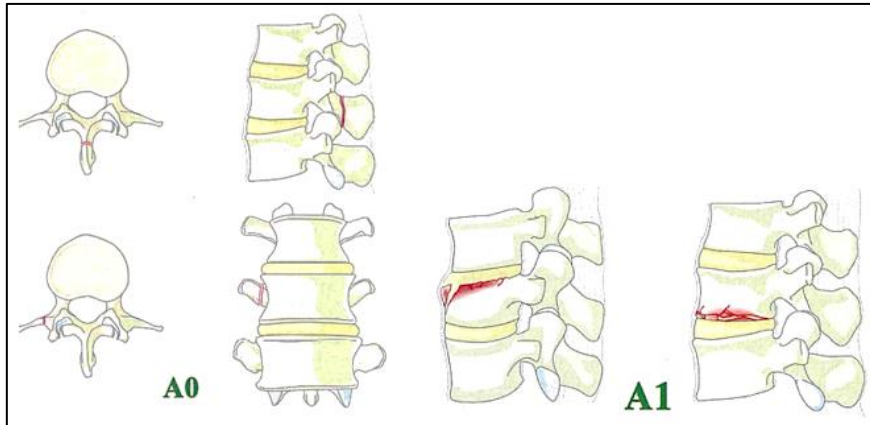


Figure 6: Subtype A0 (left)—Minor injuries: Injuries such as transverse process or spinous process fractures, which do not compromise the mechanical integrity of the spinal column. Subtype A1 (right)— Wedge Compression: Fracture of a single endplate without involvement of the posterior wall of the vertebral body. Vertebral canal is intact.

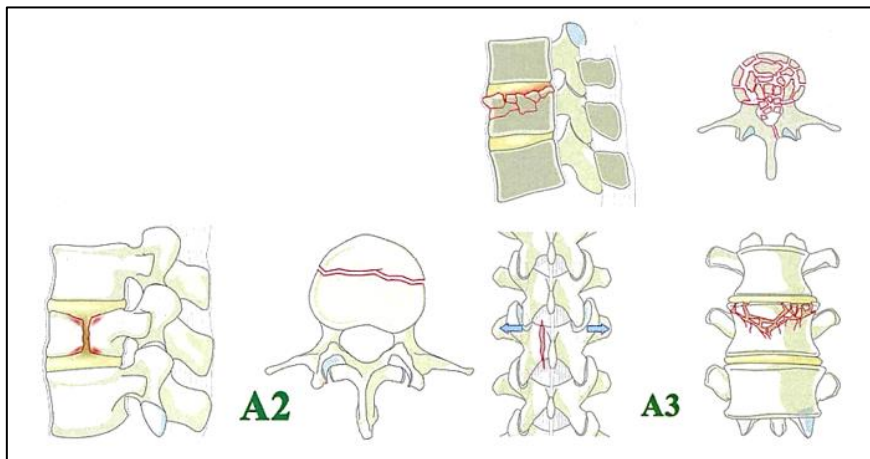


Figure 7: Subtype A2 (left) —Split or pincer-type: Fracture of both endplates without involvement of the posterior wall of the vertebral body. Subtype A3 (right)—Incomplete burst: Fracture with any involvement of the posterior wall of the vertebral body. Only a single endplate fractured. Vertical fracture of the lamina is usually present and does not indicate a tension band failure.

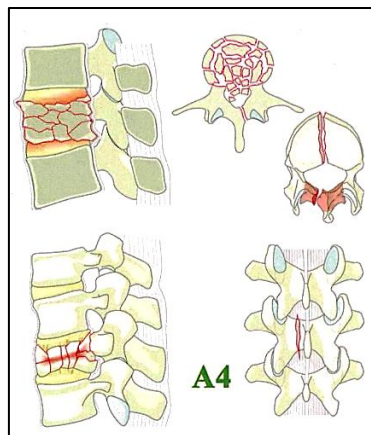


Figure 8: Subtype A4 —Complete burst: Fracture with any involvement of the posterior wall of the vertebral body and both endplates. Vertical fracture of the lamina is usually present and does not indicate a tension band failure.

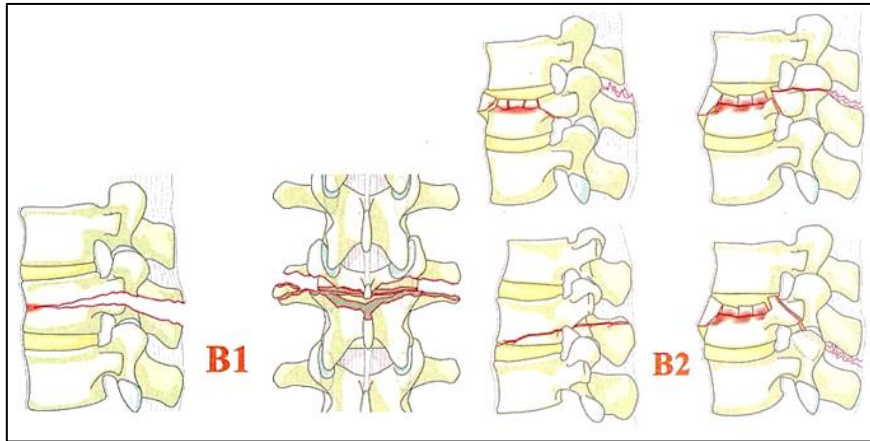


Figure 9: Subtype B1 (left) — Monosegmental bony posterior tension band injury; Transosseous failure of the posterior tension band. The classical "chance fracture." Subtype B2 (right) —Posterior tension band disruption; Bony and/or ligamentary failure of the posterior tension band together with a type A fracture, type A fracture should be classified separately.

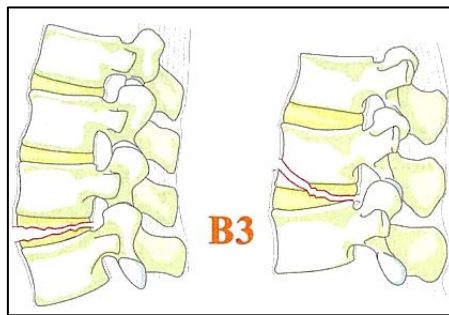


Figure 10: Subtype B3 — Hyperextension injury: Injury through the disc or vertebral body leading to a hyperextended position of the spinal column, which is commonly seen in ankylotic disorders. Anterior tension band, notably the ALL is ruptured but there is a posterior hinge preventing further displacement.

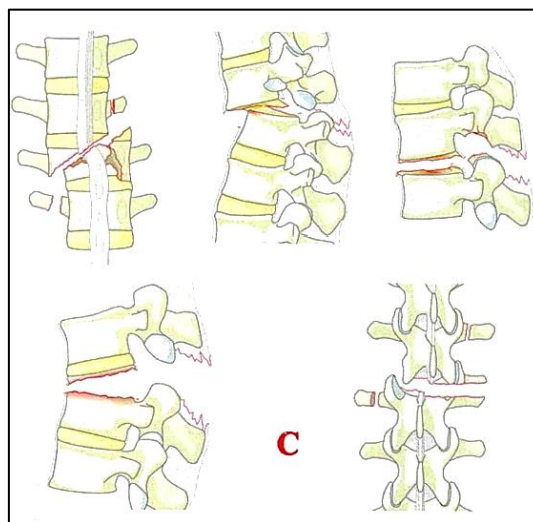


Figure 11: Type C—Translation/displacement: There are no subtypes as because of the dissociation between cranial and caudal segments various configurations are possible in different images, which are not relevant. Is combined with subtypes of A to denote the associated vertebral body fractures if necessary [13].

The grading of neurological deficit includes 5 part, from N0 to N4. The N0 grade include patients without neurological damage, the N4, instead, with complete spinal cord injury. The clinical modifiers are indicated as M1 and M2 and they are not relevant to every case but they are useful to take decisions about the treatment.

1.4 Metastatic spinal lesions and fracture risk

The spine is the third most common part of the human body affected by painful bone metastases. These metastases occur in 65-75% of patients with various other tumours, e.g. tumours of the breast, prostate, lung, thyroid, cancer... Moreover, studies show that these metastases could lead to pathological fractures, that often need a surgical intervention [20]. The metastases derive from the dysregulation of the process of resorption / deposition of the bone matrix, that leads to three phenotypes: osteolytic or lytic, osteoblastic or blastic and mixed metastases. The lythic metastases increase the osteoclasts activity and, as a consequence, a greater bone reabsorption. The blastic metastases induce an abnormal generation of bone matrix, increasing the osteoblasts activity. Lastly, the mixed metastases could simultaneously show both characteristics of lytic and blastic metastases. Some primary tumours, e.g. tumours of the lung, thyroid, kidney, colon, melanoma, breast, multiple myeloma, mesothelium, lead to lytic metastases. On the other hand, tumours of the stomach, bladder and prostate induce the formation of blastic metastases [21]. An accurate classification of the metastases according to the different tumour types is still not available, because some of them could lead to different types of metastases [22]. Anyway, the mechanical properties of a metastasis change according to the body region and tissue where it develops. The properties of the metastases and the tissue where a tumour develops, indeed, seem to have some similar features. The presence of osteolytic metastasis impacts microarchitecture of trabecular bone and alters the disposition of the collagen fibres and reduces the number and the thickness of the trabeculae[21]. The organization of the fibres and their morphology influence the mechanical

performances of the bone, such as the toughness, and also the fracture risk increased in presence of lytic metastases. Osteoblastic lesions lead also to elevated fracture risk, despite the bone volume increasing[21]. Therefore, it is important to observe how the organization of the fibres and their shape changes. Moreover, the mechanical behaviour and the failure risk are correlated to the bone mineral density (BMD). Normally, the trabecular bone density, in a healthy tissue, could be related to both the mechanical properties and the quantitative computed tomography (QCT) data [23]–[25]. Similar relationships between trabecular bone and metastases may be useful for clinical issues and for evaluating the fracture risk. Stechow et al. [26] showed that trabecular bone with metastases can be modelled as porous foams and so the same constitutive relationships can be used. Hipp et al. [27] observed that metastases in trabecular bone induced degradation of the elastic modulus but could not demonstrate if the relationships between density and mechanical properties changed in presence of a metastasis. Finally, Kaneko et al. [28] tried to improve the understanding of the influence of metastases on trabecular bone and to find a relationship between the mechanical properties, the apparent ash density (ρ_{ash}), i.e. the density of the mineral part of the bone, and the QCT data. The study has been conducted on trabecular bone of distal femur, on samples of human donors. They showed that the QCT can be used for the ρ_{ash} estimation, both for a healthy and metastatic trabecular bone. The ρ_{ash} value could then be used for the estimation of other mechanical properties, such as the elastic modulus and the compressive strength. So, the metastatic disease does not significantly compromise the ability of QCT to provide a ρ_{ash} value. However, Hipp et al. [27] conducted a study, of both healthy vertebral trabecular bone and with lesions, that show a contrasting result, i.e. the dependence of the mechanical properties on density is altered by the presence of metastasis. Therefore, they showed that fracture risk predictions have to be adjusted when the bone density is included in the estimation of the stiffness or strength. In contrast, Kaneko et al. [28] measured a strong correlation between QCT and ρ_{ash} . The different results in findings are probably due

the different use of ρ_{ash} . These findings were instead consistent with those of von Stechow et al. [26]; their relationships were pretty similar. Kaneko et al. [28] concluded that QCT can be also used in other sites, like the proximal femur and the vertebral body. Studies like these may be useful for a better understanding of the effect of metastases on mechanical properties of the bone tissue and also for an improving of the fracture risk assessment.

1.5 SINS (Spine Instability Neoplastic Score)

When the patient is subjected to spinal metastasis, it is difficult to decide the treatment and the need for surgery. One of the critical factor that influences the decisions about a surgery intervention is the probable neurological damage. Other factor that influence the decision are the spinal instability, the general health of the patient and the histology of the tumour. The spinal instability is not well defined by certain criteria. The Spine Oncology Study Group (SOSG) gave a definition of the spine instability as 'loss of spinal integrity as a result of a neoplastic process that is associated with movement-related pain, symptomatic or progressive deformity, and/or neural compromise under physiological loads' [2]. As a consequence, there are not guidelines to evaluate the risk of instability in the spine involved by metastases. Therefore, surgeons rely on their past experience to choose if surgery is or is not indicated for that patient. Despite this, the diagnosis of instability is challenging for the nonsurgeon. This often lead to wrong decisions of the patient treatment, that sometimes is postponed or insufficient. The Spine Instability Neoplastic Score is a scoring system developed for the assessment of the instability, starting from radiographic and patient factors, both for diagnosis and for facilitating the communication between oncologists, radiologists, orthopaedic and neurosurgical surgeons in order to optimize the treatment plans. The SINS is made up of six components[2]. Each component is scored individually. Finally, this scores are summed. The minimum final score is 0, the maximum one is 18. Scores from 0 to 6

denote 'stability'. Scores from 7 to 12 indicate 'indeterminate stability' and so it is possible that the patient will be soon affected from instability of the spine. Lastly, scores greater than 13 imply 'instability'. Anyway, when scores are greater than 7, surgical consultation is required. The 6 components are described below.

- **Spine location**

The spine location is quantified with a number by 0 to 3. It considers if the lesion is in an instable position. The score '0' is assigned when neoplasm is in 'rigid' segments, i.e. the parts of the nonjunctional sacral spine (S2-24). When the lesions are in the 'semirigid' segments, instead, are classified by '1'. These segments include the nonjunctional segments in the thoracic region (T3-T10), in which vertebrae are articulated with the rib cage. The 'mobile' segments include the nonjunctional and not articulating with the rib cage, i.e. C3-C6 and L2-L4 vertebrae. The score '2' is associated to these segments. Lastly, the junctional regions, which include the occipitocervical (C0-C2), cervicothoracic (C7-T2), thoracolumbar (T11-L1) and lumbosacral (L5-S1) compartments, are classified as a '3' [2].

- **Mechanical pain**

Mechanical pain is scored by 0, 1 or 3. If the patient with neoplasm have mechanical, or postural, pain, is classified as a '3'. In this cases, patients are affected by pain with movement, vertical posture or supporting loads etc. Pain-free lesions are instead classified as '0'. The '1' score is associated with occasional pain, but the latter isn't mechanical[2].

- **Bone lesion quality**

This component could be better defined by computed tomography scans. The assigned scores range from 0 to 2. Blastic and lytic lesions receive a score of 0 and 2 respectively. In the presence of a mixed lesion, the score given is 1[2].

- **Spinal alignment**

This component quantifies by scores the spinal alignment between motion segments. De novo deformity, such as kyphosis and or/scoliosis, i.e. deformity in the sagittal or coronal plane, can be firstly evaluated by a series of radiographs or by the comparison between supine and vertical radiographs. Patients with these deformities receive a score of 2. In presence of subluxation or translation, the score is 4. If the alignment is normal, the patient receives a score of 0[2].

- **Vertebral body collapse**

The scores assigned for this component are associated to the percentage of vertebral body height collapse. However, this component involves only the anterior and middle column affected by tumour. The scores range from 0 to 3, associated to an increasing percentage of collapse. '0' indicate, indeed, the absence of collapse; while '3' indicates that more than 50% vertebral body collapsed[2].

- **Posterolateral involvement of spinal elements**

The scores associated to this component can be 0, 1 or 3 and allow to quantify the contribution of the posterior elements, including pedicles, facets and costovertebral joints, in the tumour. When these elements are not involved in tumour, the score is

‘1’. Bilateral involvement is scored as ‘3’. This score is more than double the contribution of unilateral involvement, which is scored as ‘2’, because it is destabilizing[2].

Table 1 reports a summary of all the elements included in the SINS, with their scores.

Element of SINS	Score
Location	
Junctional (occiput-C2, C7-T2, T11-L1, L5-S1)	3
Mobile spine (C3-C6, L2-L4)	2
Semi-rigid (T3-T10)	1
Rigid (S2-S5)	0
Pain relief with recumbency and/or pain with movement/loading of the spine	
Yes	3
No (occasional pain but not mechanical)	1
Pain free lesion	0
Bone lesion	
Lytic	2
Mixed (lytic/blastic)	1
Blastic	0
Radiographic spinal alignment	
Subluxation/translation present	4
De novo deformity (kyphosis/scoliosis)	2
Normal alignment	0
Vertebral body collapse	
>50% collapse	3
<50% collapse	2
No collapse with >50% body involved	1
None of the above	0
Posterolateral involvement of the spinal elements (facet, pedicle or CV joint fracture or replacement with tumor)	
Bilateral	3
Unilateral	1
None of the above	0

Table 1: Summary table including elements of SINS [2]

In conclusion, this scoring system provides objective criteria to assess the instability of metastases. We need to remember that instability is just one of the factors that have to be considered during the management of a patient involved by metastases in the spine, but it is one of the most difficult to assess. Indeed, metastatic lesions usually involve different patient factors, as said before. In patients with this disease but without neurologic deficit, it is fundamental to recognize the instability entity or whether instability could impend, in order to stabilize the patients. On the contrary,

for patients with neurological deficit, the role of surgery is well defined. Therefore, the scoring system could aid to define the spinal instability and to take better decision during the treatment of the patient [2].

2 Background and aims

The evaluation of the bone strength can be performed non-invasively by FE models, both in case of healthy and pathological tissue conditions. The available literature about FE models of vertebrae affected by metastases is non conclusive: there are some dated works, which are interesting but poorly validated; others, more recent, are often not validated and with few conclusions. Most of all, even the available studies about FE models of healthy vertebrae do not seem to highlight a consensus, and show several limitations. In the next sections, some published FE models will be described. As the presence of metastases influences the mechanical properties of the bone, this will also be an aspect to be kept under control in the models. For this reason, we chose to analyse, first of all, models of intact vertebrae, and then move on to the analysis of models of metastatic vertebrae. So, the following paragraphs (from 2.1.1 to 2.1.3.3) will deal with the non-pathological vertebrae models, in order to define their features and their contradictions. Then, paragraph 2.2 will include the analysis of metastatic vertebrae models. In this part, some studies on thoracolumbar vertebrae, affected by lytic metastases, were selected to highlight the factors most closely related to the risk of fracture. This analysis of the literature state of the art will finally lead us to formulate the aim of the present thesis project (paragraph 2.3).

2.1 FE models for intact vertebra

The construction of a FE model requires several choices, which need to be properly justified and controlled. The first choice to make concerns the images source, from which geometry is reconstructed. Usually, the devices used for scanning images are magnetic resonance imaging (MR), for soft tissues, such as the intervertebral disc, and computed tomography (CT) for hard tissues, such as bone[29]. Therefore, CT images

are frequently used for vertebra studies, as they provide quantitative data on geometry and mechanical properties. There are three most used CT types:

- Quantitative computed tomography (QCT)
- High resolution peripheral computed tomography (HR-pQCT)
- Micro computed tomography (μ CT).

The HR-pQCT is a non-invasive method for assessing volumetric bone mineral density and microarchitecture. This technique allows to get scans with accuracy and relatively low-dose radiation. In the last years, its application in clinical research increased. It is used for better understanding age-related and sex-related differences in bone microarchitecture and differences in presence of metabolic disorders. Moreover, it is coupled with FE modelling, to assess bone strength [30]. Pahr et. Al validated against experiment models realized from HR-pQCT and from μ CT [31]. Their approach gave good estimates for apparent stiffness and strength. Models turned out to be equally accurate. These results provided support of the usage of HR-pQCT usage for the prediction of human bone stiffness and strength. On the other hand, μ CT is an important tool for research for acquiring quantitative 3D information. It allows the non-invasive inspection in small animals with high spatial resolution and sensitivity. However, the use is limited also because of the high radiation dose, that could be harmful[32]. Anyway, clinical use is not intended. Fields et al. [33] used μ CT-based finite element modelling to investigate the role of the trabecular microarchitecture and the cortical thickness on the vertebral biomechanics, or rather on strength and stiffness, and their relations. Lastly, the QCT allow to measure bone mineral density, using a computed tomography scanner and to get a 3D image. QCT can indeed determine the volumetric density (mg/cm^3) of trabecular or cortical bone at any skeletal site. Moreover, it is an established technique for this measurement in the spine [34]. It distinguishes between cortical and cancellous bone and it is widely

used in the research, although the resolution is lower than the previous ones, also because of the low radiation exposure, when correctly performed[35]–[38]. Anyway, model based on QCT images, present in literature, gave good results. So that, it could be a good choice both for the faster availability and the simple clinical use.

The three-dimensional reconstruction, in turn, will require the choice of a technique to be used, such as segmentation or voxel mesh.

The subsequent modelling step is the generation of a volume mesh. Generally, a volume mesh is generated for both the cortical and trabecular compartments. However, researchers modelled cortical bone in several ways (paragraph 2.1.1).

Next step is usually the assignment of the material properties to the elements of the mesh. In particular, this step includes many measures. A careful study of the current literature, for example, is necessary to resort to laws, suitable for the type of bone tissue to be modelled (paragraph 2.1.2).

2.1.1 Patient-specific cortical layer or constant shell

In the last 70 years, trabecular bone loss and fractures of the trabecular vertebral bodies have been a central topic in research; therefore, attention has shifted from cortical bone. Despite the contribution of the cortical bone on biomechanics and bone strength [39] is now evident, it is often not modelled appropriately. Indeed, the vertebral cortical bone consists of a really thin structure. In this case, it is hard to reconstruct the geometry accurately because the resolution of the CT imaging devices is of the same order or higher (>0.25 mm for research scanner and >0.9 mm for clinical scanner[40]), that the cortical thickness. Due to the partial volume effect, the CT values will be altered and therefore the assigned material properties will be inaccurate. Finally, this could lead to a wrong prediction of the biomechanical properties, such as the distributions of the stress and strain distributions in the FE models [40], [41]. For these reasons, some researchers used to simulate the cortical

bone compartment with a thin shell with constant thickness and elasticity, independent of QCT data [36]. Liebschner et al. [40] modelled vertebral shell as an isotropic continuum with constant thickness (0.35 mm). the vertebral shell elastic modulus was calibrated, matching the stiffness measured in the experiment with the stiffness obtained from the modelled vertebrae. Then, the mean value has been calculated and assigned to the shell. Imai et al. [36] realized a 0.4 mm thick shell to model the cortical compartment, setting the Young's modulus to 10 GPa. So, in these cases, the cortical shell was considered as a homogeneous material and this is a limitation, because it alters the specimen-specificity, since material properties and geometrical data of the cortical shell are not obtained from QCT scans[42]. On the other hand, some researchers don't explicitly model the cortical compartment. For example, Crawford et al. [35] decided to not model the cortical shell because their previous FE analyses concluded that the shell has only a minor structural role and because of the reasons described previously. Thus, material properties of the finite elements on the periphery of the model have been assigned by integration of mineral density of the shell or endplate and the adjacent trabecular tissue. Buckley et al. [38] also treated elements along the interface between the cortical and trabecular compartment as trabecular bone elements in assigning material properties with the density-elasticity laws chosen for the trabecular component. In conclusion, the low spatial resolution of QCT systems do not permit to model the cortical shell explicitly. On the other hand, modelling the cortical shell with constant thickness and material properties exclude the sample specificity and cannot reflect the real mechanical behaviour of specimens [42]. Including a subject-specific cortical shell in the CT-based models could improve the accuracy of the prediction of the mechanical behaviour of the vertebral bone tissue. This is really challenging.

2.1.2 Material properties

Elastic properties of bone are usually correlated to the bone density to obtain density-elasticity relationships, i.e. mathematical relationships between the density measurements and the Young's modulus, that could be used for deriving the bone mechanical properties starting from CT-data. Over time, many relationships have been adopted in the construction of FE models [24], [28],[43],[44]. The trabecular bone is highly porous and anisotropic, so complex experimental techniques are needed to measure the mechanical properties. This leads to a large number of relationships and also to a large spread in the predicted elastic modulus [45]. Helgason et al. reviewed all relevant literature about the relationships, including those derived from similarly controlled experiments [45]. Substantial inter-study differences exist and they can only be partially explained by the methodological differences between studies. So, it is important to define a standardized methodology to identify the relationships suitable for subject-specific FE models. The reports currently available have been obtained with different experimental set ups. For this reason, different artefacts and sources of errors may have influenced the result. Other extensively methodological features, that can affect the estimation of the elastic modulus, are the size and geometry of the bone specimens, together with the set loading rate during the stiffness calculation. Anyway, Helgason et al. [45] observed an unclear effect of the anatomic site, with the partial exception of the vertebral bone specimens. For example, Morgan et al. [46], cited in the review, show a significant variation of the density-elasticity curve with the anatomical site. Many other researchers agree about this topic and this seems to be due to differences in trabecular architecture, and possibly even tissue modulus, which are not considered in the simple density-elasticity relationship. So, it is important to choose the relationship in the FE subject-specific model according to the anatomical site [45]. In addition, it should be considered that, compared to the trabecular compartment, for which there are over

20 reports in the previously cited review [45], only few studies were dedicated to cortical bone in the last 40 years [47]. Schileo et al. analyze the available works, showing some inconsistencies. For example, in their work, they excluded the relationships derived from compressive tests carried on with the platen technique, that leads to an error of overestimation of the specimen response [43], [48], as reported in the review [45]. Furthermore, they excluded two other relationships [49], [50], because they produced unrealistic elastic moduli at density values still viable for cortical bone.

2.1.3 Experimental set-ups

To verify the simulations, the model must undergo an experimental validation process. This deals with the comparison between the results obtained solving a model and the experimental measurements. Moreover, the latter need to be carried on simulating the physiological conditions. However, replicating boundary conditions and physiological loading conditions is often complex. Also in this case, different researchers make different choices, more or less consistent. Different specimen types are used and the choice of the testing conditions depends on the simulated action. Furthermore, researchers treat the specimen with different approaches. Finally, in vitro loading conditions should be based on in vivo data but this is challenging because of the complexity of the spine[51].

2.1.3.1 Preparation of the specimens

According to the aim of the study, different types of specimens are used. Isolated vertebrae are used to investigate structural properties[51]. Studies use whole vertebra, isolated vertebral body or vertebral body without endplates. Recurrently, single vertebrae are used. Posterior processes are often excised by cutting through the

pedicles[35]–[37], [40], [42], [51], [52]. Moreover, clinically, the vertebral fractures occur mostly at the vertebral body. Since the posterior processes could share axial load, the conditions of loading in vivo could be different. For these reasons, posterior processes should be included to predict the in vivo behaviour of vertebral bones[36]. Some studies include another simplification, i.e. the removal of the endplates [42], [53], [54]. The aim was to obtain vertebral sections with parallel surfaces. This choice don't mimic exactly the in vivo condition, because the physiological loadings are shared by the vertebral disc and the endplates too[55]. In absence of the load contribution of the posterior elements, instead, the load could be all transferred to the anterior part [40]. Moreover, the integrity of the vertebral body is compromised [51]. On the other hand, core specimens are sometime extracted to test the mechanical properties of the trabecular compartment [51]. Lastly, spine segments are sometime used to investigate the spine kinematics. The latter are usually composed from two or three adjacent vertebrae. These sets have sometimes been used to transfer load in physiological way through the intervertebral discs and to explore the spinal instability [51], [56]. For example, Ahn et al. [57] investigated the instability due to a simulated metastasis in a thoracolumbar spinal segments. While testing single vertebrae allow to simplify the in vivo scenario and to focus on the structural properties of the vertebral bone, testing segments has the advantage to better simulate physiological conditions [51].

2.1.3.2 Boundary conditions

The definition of boundary conditions is also accomplished in different ways. This step requires attention during the experimental tests. When isolated vertebrae are tested, the surrounding soft tissue, such as intervertebral discs, ligaments, spinal cord and cartilage, are removed. So, loads could be applied to endplates or to a layer of embedding material, used to hold the sample during the tests[51]. One of the most

common procedure include the moulding of the vertebral bodies to the concave endplates using a layer of polymethylmethacrylate (PMMA) [35], [37], [40], [52], [58]. This could ensure plano-parallel ends and that the sample is uniformly compressed through endplates[59]. Obviously, the application of the loads through PMMA, rather than the intervertebral discs, differ from in vivo conditions. Maquer et al. [60] showed, for example, that the PMMA layer on the superior endplate tends to overestimate the failure load in axial compression loading condition. Some other studies used other materials , such as resin [36] or rubber [42], [59], introducing an undetermined deformation component during the test [55]. Furthermore, the interposed material could give complications in modelling its behaviour. On the other hand, Dall'Ara et al. didn't interpose any material between the vertebral body and the loading plates, however they removed a slice of the endplates to load the vertebra between two parallel planes. Anyway, the material layer interposed between the tested vertebra is likely to constrain the vertebral body non-physiologically. Therefore, it would need to be designed to best match the material properties of the disc [51].

2.1.3.3 Loading conditions

The definition of the loading conditions is one of the most difficult steps. The spine is always subjected to loads during the daily life activities. The in vivo loads pattern is very complex and, consequently, it is really hard to measure it. Usually, a combination of measurements of vivo kinematic parameters and mathematical models is needed to derive the information[51]. Then, this pattern should be implemented in the FE models. According to the review of Brandolini et al. [51], the most commonly implemented load condition is axial compression [33], [36], [38], [40], [59], [61]–[69]. In some cases, the compressive load is applied on bone cement layer. However, this condition represents a simplified scenario. In vivo, vertebral fractures are associated

with eccentric compression and bending loads[58]. So, they can't be reproduced by loading the vertebra between two parallel planes[61]. Although the performance for uniform compression is well known, it needs to have a model that could predict vertebral strength in bending, as well as compression. Some studies reached some premature conclusions also with anterior bending condition but the ability of prediction is not well established yet[58]. However, loading the vertebra through the PMMA has consequences, such as the inability to visually evaluate the failure pattern of the endplates after the test. Moreover, this load condition can lead to an unwanted bending moment. Therefore, there is an high risk of other load components besides pure compression[59]. A limitation of other studies (such as [62]) has been the use of rubber as inserted material to simulate the intervertebral disc. The rubber is indeed not able to 100% simulate the deformation of the intervertebral disc and to distribute the loads.

Anyway, the response to combined compression and anteroposterior bending is of clinical interest[66]. Studies focused on compressive loading. This is comprehensive because functional loads on spine are primarily compressive and under compression, the stresses in the vertebra are vertical. However, since many osteoporotic vertebral fractures are wedge fractures, the response to forward flexion may have additional clinical relevance[68].

2.2 Metastatic vertebrae models

The presence of metastases, in one or more vertebrae, compromises the integrity of the spine, as well as its stability. For this reason, there is an increased risk of fracture, even during daily life activities, during which the spine is subjected to physiological loads. So, the prediction of the fracture risk could be really useful to guide the clinical decisions, both with prophylaxis and surgery interventions[1]. As said before, actually the SINS is used as scoring system to determine the risk of fracture. However, these

scores are only qualitative. This limit could be compensated with the use of a quantitative method. A combination of these method could improve the reliability of a scoring system in determining the risk factor and so could help in the calculation of the structural integrity of the spine. Finite elements could be a good tool for this aim. Some FE models, including metastatic lesions, have been developed. Two studies [11], [70] laid the foundation for calculating fracture risk through equations that include parameters such as tumour size, bone density, pedicle involvement, applied load, loading rate and disc generation. However, the anatomy and the material properties were very simplified. Therefore, these models could not simulate many of the possible conditions. Whyne et al. [70] removed a sample laterally from the trabecular vertebral bone to create a defect. This void was then filled with a solution of agarose gel, in order to simulate the properties of the lytic metastasis. They loaded both the specimen and the model in axial compression. Their aim was to develop and validate a model of metastatic vertebrae for investigating the parameters that influence the fracture risk prediction. The lesion size was found to more contribute to the risk of fracture initiation and consequent neurological damages. This result was in accordance with other previous studies. The study lead to the development of equations able to assess the risk of burst fracture in metastatic spine. The model was well conceived, although validation was limited to few data points and they didn't consider bending and torsion. The equations must be applied to clinical data to determine the validity and utility[11]. Starting from these models, Roth et al, [71] investigated about their ability in prediction of the vertebral stability and clinical thresholds for burst fracture risk. Moreover, they tried to find methods to get information useful for the burst fracture risk estimation. Galbusera et al. [1] investigate the influence of the location and the size of the metastasis and the bone quality on the vertebra stability. They built a series of FE models, adding tumour lesions with different size, pseudo-spherical shape and in random positions. They concluded that the size has a fundament role, rather than the other analysed features. Anyway, these latter have a not negligible role in the

loading conditions they chose. In general, the predictions of the models were in accordance with other studies. Also in the previous studies, ‘the critical importance of the tumour size in determining the mechanical response of the vertebrae under compression loads, in terms of axial collapse and deformation in the transverse plane’, was shown [1]. Several studies focusing on bone metastases used a poroelastic model. Starting from the model presented by Whyne et al. [72], Tschirhart et al. [73], [74] also investigated about the fracture risk in metastatically involved vertebrae, In one study, they compared two techniques by which model and represent the lytic metastases. In another one, they explored the effects of vertebral level, in thoracic compartment of the spine and geometry and the effects of tumour lesion on the cortical compartment on initiation of burst fracture in metastatic vertebrae. Also this group chose to model the vertebrae using poroelasticity with the aim of better representing the biomechanical behaviour of the burst fractures in metastatic spine. In summary, the studies provided a quantitative method to calculate the effects of vertebral level, geometry and transcortical tumours. Upper thoracic vertebrae, in presence of metastases, were found to be at increased risk of burst fracture. Transcortical tumour scenarios investigated in the study resulted in decreased risk in initiation of burst fracture. The results also indicated that burst fracture risk depends on location and shape of the tumour lesion. Compared to the studies described above, this study shows that the most critical factor is the location, rather than the tumour size. The impact of tumour location seems to be greatest in the posterior part of the vertebral body.

‘These findings should aid in the development of improved modelling and ultimately more accurate neurologic risk assessment criteria. A more comprehensive understanding of factors contributing to the risk of burst fracture may improve clinical decision-making and treatment options for patients with vertebral metastases’ [73].

2.3 qSINS project overview and aims of the current work

Currently, the instability of the spine involved by metastatic lesions is assessed by the SINS (section 1.5). However, this scoring system is qualitative. Starting from this considerations, the project about the quantitative Spine Instability Neoplastic Score (qSINS) started in the Bioengineering and Computing Laboratory (BIC) of the Rizzoli Orthopaedic Institute, in order to improve the SINS. The aim was to introduce the patient-specific vertebral biomechanics in the assessment of the instability of the spine, affected by tumour lesions. For this purpose, FE subject-specific (SSFE) models could be constructed, then used to evaluate the strength of the vertebra in a non-invasive way and finally to guide the treatment of the patient or the decision about a possible surgery. As described before, these models can be realized starting from CT images, that are commonly collected when patient is affected by bone tumours. However, many other variables have to be considered during the construction of the models. Actually, there isn't a well validated model of metastatic vertebrae. One of the greatest problem of the construction of these models is the modelling of the metastases, both for their material properties and their contribution on the changes of the mechanical properties of the bone. Moreover, there are not clear information about the parameters of the lesions that more influence the vertebral biomechanics. Anyway, also models of intact vertebrae are often not completely realistic and have some limits, there are many different modelling and validation approaches and there are not coincident results. So, these models are not suitable for clinical applications. For all these reasons, the project started with the realization of a model of healthy vertebrae but the final aim will be to build a realistic metastatic vertebral model. This thesis is part of the qSINS project. The work started from the considerations previously collected by Pierpaolo Romano [75] and Giulia Fraterrigo [4], that performed their thesis work in the BIC laboratory too.

The final aims of this work were:

1. the construction of a FE model of an intact vertebra with a patient-specific cortical compartment (CBM-model). In absence of experimental data, we started comparing the CMB-model with the Shell-model, previously developed by the BIC team, in which a uniform shell mimics the cortical compartment;
2. the check of the suitability of the loading conditions, applied both in the models and in the experimental test by the realization of a polyurethane replica;
3. the comparison of the CBM-model with the experimental results.

3 Material and methods

The preliminary purpose of the work was the estimation of the vertebral cortical bone properties, i.e. density and thickness, starting from clinical images, and to get a patient-specific cortical layer by the Stradview software (section 3.1.4). The estimation has been carried out on seven specimens, after their scanning and segmentation. Starting from the considerations and the results of the preliminary estimation, the next aim was the construction of the model of an intact vertebra. The main feature of this SSFE model is the patient-specific cortical compartment.

Next step was the comparison of this model with the model realized by Giulia Fraterrigo in a previous master thesis work [4] at the BIC laboratory of the Rizzoli orthopaedic institute in Bologna (section 3.4). This previous model presented a shell, with uniform thickness and material properties, to mimic the cortical layer. So, the aim of the comparison was to analyse the influence of the patient-specific cortical compartment, rather than a constant shell, on the mechanical behaviour of the modelled vertebra.

For both the models, we set the loading and boundary conditions, according to the experimental set up (section 3.2).

In order to ensure that the hydrostatic pressure, chosen as loading condition, was uniformly distributed on the basis of the specimen, the team of the Medical Technologies Laboratory of the Rizzoli Orthopaedic Institute constructed and tested a homogenous polyurethane sample. Thus, we constructed a model to replicate the experiment and to understand if the boundary conditions were correct (section 3.5).

3.1 Towards the 3D FE-model

We realized the finite element (FE) model in different steps, resumed in Figure 12.

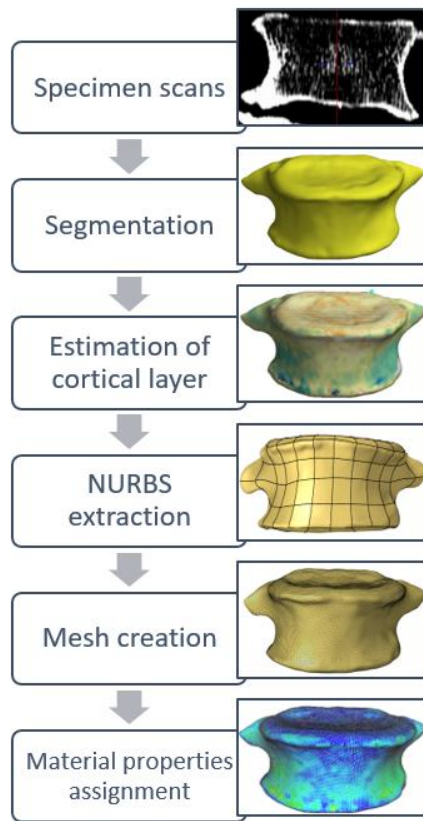


Figure 12: Construction of the model

After these steps, we proceeded with the application of the loads and constrains and the solving of the simulations, using ANSYS Mechanical APDL (ANSYS Inc., Canonsburg, PA).

3.1.1 Available specimens

Seven human vertebrae, from two donors, were available to build new FE models. We relied on two lumbar vertebrae (L4-L5) of the first donor (Donor #1) and five thoracic vertebrae (T6-T10), from the other one (Donor #2). Table 2 includes some details about the donors.

<i>Donor #1</i>	
Donor number	#4793
Sex	Male
Height	175 cm
Weight	70 kg
<i>Donor #2</i>	
Donor number	#5601
Sex	Male
Height	198 cm
Weight	71 kg
Cause of death	Heart attack

Table 2: Donor information

All the vertebrae have been used to obtain the cortical compartment properties, i.e. thickness and density. In particular, the aim was to explore the parameters in Stradview (version 6.03, developed from Stradwin, University of Cambridge, UK [76]) and their influence on the estimation of the properties (section 3.1.4). Only the L5 vertebra from the Donor #1 has been used to construct the Finite Element (FE) model, because these will be the first mechanically tested specimens.

3.1.2 Images acquisition

All the vertebrae were scanned, with different devices and kernels. A summary of the available collections of clinical images is shown in Table 3.

In order to compare the results of the computed tomography (CT) scans, indeed, the unit of measure is the Hounsfield units (HU), i.e. numbers that vary on the Hounsfield quantitative scale and describe radiodensity. The HU scale allows to transform the original linear attenuation coefficient in a HU value, thanks to a linear law which includes the attenuation coefficient of the distilled water and of the air. This scale can provide an accurate absolute density for the scanned tissue. On the other hand, it is not possible to have a correlation between grey values and absolute values of density of the tissues in the cone beam CT (CBCT) scans. A value of density will correspond to a grey level but the relationship between density and colour is not univocal.

Different parts of the scans in different positions of the organ could have different grey values, despite they have the same densities [77].

	Set	Device	Kernel	Voxel size	Notes
<i>Donor #1</i>					
L4	1	CT	BONE2	0.2734 x 0.2734 x 1.25 mm ³	
	2	CT	STD2	0.2734 x 0.2734 x 1.25 mm ³	
	3	CBCT Carestream		0.26 x 0.26 x 0.26 mm ³	
L5	5	CBCT Newtom		0.09 x 0.09 x 0.09 mm ³	<i>Reference</i>
	6	CBCT Newtom		0.24 x 0.24 x 0.24 mm ³	
	7	CT	BONE2	0.2734 x 0.2734 x 1.25 mm ³	
	8	CT	STD2	0.2734 x 0.2734 x 1.25 mm ³	
<i>Donor #2</i>					
T6	9	CBCT Newtom		0.15 x 0.15 x 0.15 mm ³	<i>Reference</i>
	10	CT	STD1	0.3516 x 0.3516 x 0.6 mm ³	
T7	11	CBCT Newtom		0.09 x 0.09 x 0.09 mm ³	<i>Reference</i>
	12	CT	STD1	0.3516 x 0.3516 x 0.6 mm ³	
T8	13	CBCT Newtom		0.09 x 0.09 x 0.09 mm ³	<i>Reference</i>
	14	CT	STD1	0.3516 x 0.3516 x 0.6 mm ³	
T9	15	CBCT Newtom		0.09 x 0.09 x 0.09 mm ³	
	16	CT	STD1	0.3516 x 0.3516 x 0.6 mm ³	
T10	17	CBCT Newtom		0.09 x 0.09 x 0.09 mm ³	
	18	CT	STD1	0.3516 x 0.3516 x 0.6 mm ³	

Table 3: Image sets

Studies are ongoing to correlate HU units and grey levels of the CBCT but at the moment the HU units in CBCT cannot be considered reliable for the determination of site-specific bone density. Only the CT-scans have been considered for the construction of the models, because of the limitation of the CBCT scans in the determination of the tissues densities, described above.

The CT-scans have been performed together with a hydroxyapatite phantom, thanks to whom the values of Hounsfield Units (HU) have been converted in radiological density values.

3.1.3 Segmentation

The first step was to extract the contours and to get a surface of the vertebra. The used software is the freeware Stradview (version 6.03, developed from Stradwin, University of Cambridge, UK [76]). Starting from the CT data, the exterior cortical surface was extracted by a semi-automatically segmentation, i.e. by setting a grey threshold to an appropriate value and then proceeding with a manual control of the contours generated by the software, where necessary[78]. For each set of images, osteophytes were excluded, and posterior processes were cut. The entire set of contours was used to create a 3D geometry of the vertebra, generating a surface made of triangles, with a certain level of resolution and smoothing, selectable in Stradview. At first, the smoothing strength was set on ‘medium’, then it was increased to ‘very high’, to evaluate the influence on the estimates with a little change of the segmentation. The resolution was always set on ‘high’; indeed, high resolution values generate surfaces with smaller triangles. The result was a surface with typically up to 20,000 vertices for typical low-resolution data. Surfaces extracted from high resolution data were more detailed [78]. An example of segmented surface is shown in Figure 13.



Figure 13: Example of segmented surface.

The estimation of cortical bone density, and then of cortical thickness, were done on these 3D-reconstructions, that act as initial estimate of the external surface of the vertebra.

3.1.4 Estimation of the vertebral cortical bone properties

The definition of the trabecular and cortical bone distribution is critical for the assessment of the bone mechanical properties. Currently, the resolution of clinical CT images is limited and images are affected by blurring. Consequently, the thickness of the cortical bone, especially in the submillimetre range, is often overestimated and, therefore, the density is underestimated[79]. Because of this, thin structures, such as the vertebral cortex, are not well represented and modelled.

Then, the first aim of the work was to measure the vertebral cortical bone density and thickness. The software used is Stradview. The selectable parameters have been changed, in order to get a protocol, whereby the bone properties could be estimated, without having large errors by slightly varying the parameters. This goal required some previous steps, described in the following sections and resumed in the Figure 14.

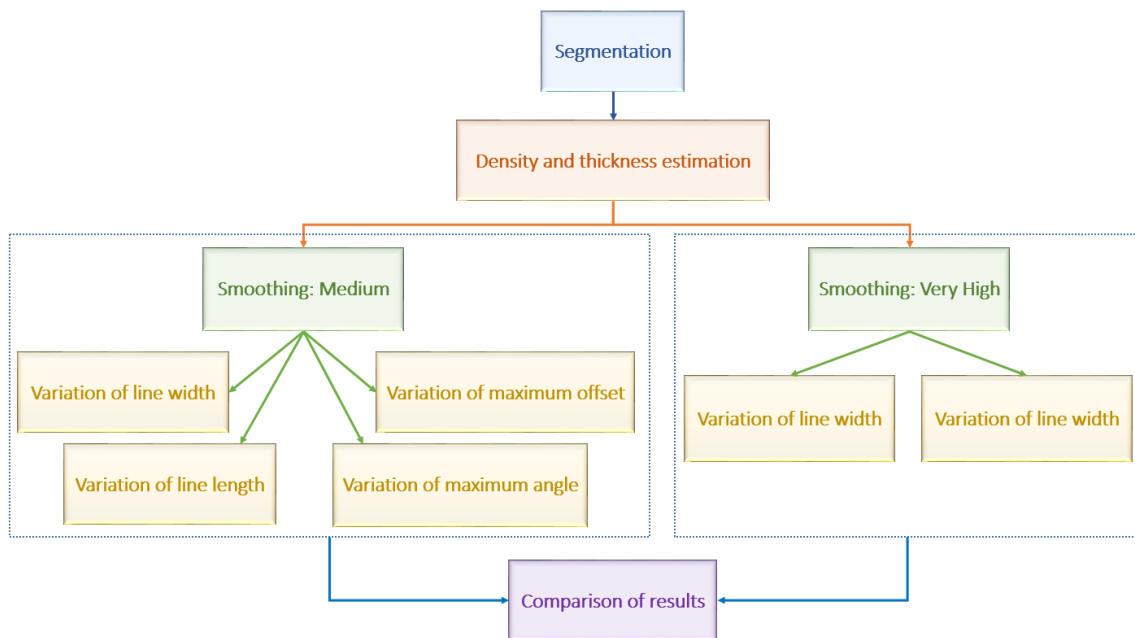


Figure 14: Workflow - Exploration of the Stradview parameters

3.1.4.1 Cortical Thickness Mapping

Once a surface has been created by segmentation, Stradview allows to map the properties of the cortex, such as density and thickness, on the surface of the bone. The coloured map is the result of a previous estimation of the parameter. The cortical thickness is derived from a cortical density estimation. The chosen algorithm for this purpose is defined 'Cortical Bone Mapping v2' (CBMv2) in the latter version of Stradview. The CBMv2 algorithm calculates the estimated density by looking at the actual HU values, along a line through the data [76]. The line lays in the imaging plane and it is normal to the cortical layer, supposed to be locally flat. CBMv2 permits to get the deconvolved cortical thickness and density, through non-linear optimization [79]. The estimation is performed in the points used to define the contours of the vertebra, together with the corresponding normal [78]. Thus, the cortical thickness estimate is based on the fitting between the function used to model the variation of the CT data through the cortex and the actual CT data, at each measurement point. The line has also to be length enough to pass through both the cortical layer and any blurred prolongation, due to the imaging process [78]. The user manual of the software suggests using a line at least three times the maximum thickness to be measured, including any extension caused by blurring. The user could also set a certain line width (W). If this is set to anything other than zero, then the data will be averaged in a direction orthogonal to the line before anything is estimated. This can be useful for very high resolution data, since it preserves the resolution through the cortex, whilst averaging data over the cortical surface [76]. The outer cortical edge is automatically aligned before this averaging takes place, in order to preserve as much resolution as possible through the cortex. Having completed the estimation process, cortical thickness could be shown as a colour wash over the surface. An example is shown in Figure 15.

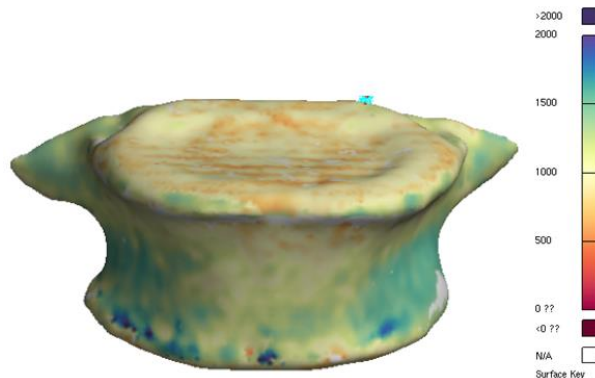


Figure 15: Example of coloured density map [HU]

3.1.4.2 Creating the entire cortical surface

Starting from the density estimation, and then the thickness estimation, a new object can be created. In the process of calculating cortical thickness it estimates the exact locations of various outer and inner surfaces. So, it is possible to create a new object from these measurements which exactly defines both inner and outer surfaces of the cortex[76]. Before creating this alternative surface, the user can set the smoothing strength and the resolution. If the smoothing strength is set to 'Very low', only the outliers are filled; otherwise, with higher smoothing levels, all data will be smoothed. A 'medium' strength has been always chosen, except when evaluating the influence of the smoothing level. The anomalous values are detected on the basis of the difference between the most external cortical surface detected and the original surface, that is generated starting from the segmentation. In particular, there are 2 ways to define an outlier:

- a) Slider '*Reject angle above ...*' allows you to select the maximum acceptable angle from the normals to the triangles on the surfaces in comparison;
- b) Slider '*Reject distance beyond ...*' allows you to select the maximum acceptable distance between the surfaces in comparison [76].

Finally, the new object will consist in an outer surface, i.e. the periosteal surface, and an inner surface, i.e. the interface surface between the cortical and the trabecular bone. An example is shown in Figure 16.

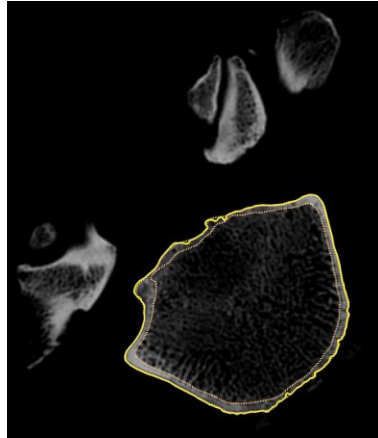


Figure 16: Example of extracted cortical layer (orange)

So, in order to find some guidelines for estimating the properties of the vertebral cortical bone, we varied both 'pre-processing' parameters, which affect the estimation of properties, and 'post-processing' parameters, i.e. the maximum acceptable angle and distance values and the smoothing level. Then, we compare the obtained surfaces with a reference object. In absence of a reference result, we varied the parameters and we verified if the trend of the cortical properties was the same.

3.1.4.3 Variation of the line width

The line width (W) was the first analysed parameter. The line width has been set on 0, 2 and 4 pixels, while the line length has been fixed on 20 mm. The maximum acceptable offset and angle were set on default values (40 pixels and 37° respectively). After a comparison between the objects, an optimal thickness has been chosen, i.e. the value for the differences between the estimates, in terms of cortical thickness, appeared smaller

3.1.4.4 Variation of the line length

Next step was to check the influence of the line length (L) on the estimate. For this purpose, this parameter has been varied between 8, 12, 16, 18, 23 and 26 mm. At this stage, the parameters of line width, smoothing strength, maximum acceptable angle and distance have been kept constant.

3.1.4.5 Variation of the maximum acceptable offset and angle

The maximum acceptable angle (A_{MAX}) and offset (O_{MAX}) have been also varied to evaluate the effects on the results. The A_{MAX} has been changed between 10° , 20° , 30° , 50° , the O_{MAX} between 0 and 40 pixels. Keeping constant the maximum acceptable angle, there were no differences between the objects obtained by varying the maximum acceptable distance. As regards the variation of the maximum acceptable angle, it was observed that, increasing the value of A_{MAX} beyond the default value, there were no evident differences compared to the object obtained with the default value (37°). On the contrary, for lower values of the A_{MAX} , the increase in thickness in one area and the reduction in another have been observed, compared to the object obtained with the default value. However, these changes did not lead to an object more similar to the reference object. Therefore, not deducing a continuity line between the results obtained, it was decided to continue the estimates with $A_{MAX}=37^\circ$.

3.1.4.6 Variation of the smoothing strength

For further considerations, other tests, equal to the previous ones, have been carried out, setting smoothing level on 'Very high'. The aim was to evaluate the influence of the smoothing level on the estimate of the properties.

3.1.4.7 Comparison of results

At each step, the results were compared with the object chosen as a reference, when it was possible. For this purpose, the objects, obtained from the estimate, have been imported into the AlbaMaster® software (developed in the BIC laboratory) and placed with respect to the same reference system, i.e. that of the reference object. Then, the cortical thickness has been measured to compare it with the reference object one. The thickness measurements were carried out in non-critical points, i.e. points far from osteophytes, posterior processes and gaps on the posterior wall of the vertebra, where the estimate could be compromised by the geometry and particular properties of the bone.

- **First exploration**

- **L5 vertebra**

We started with the analysis of the L5 vertebra. In this case, the measurements points can be viewed in Figure 17 and Figure 18.

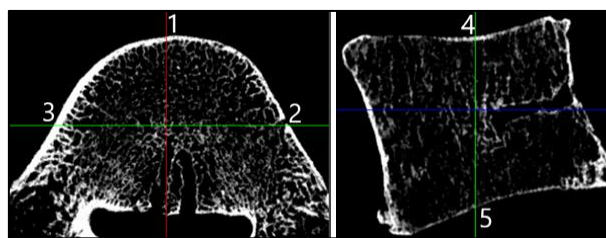


Figure 17: Cross section (left) and sagittal section (right). $X=0, Y=-7, Z=0$. X: Red, Y: Green, Z: Blue.

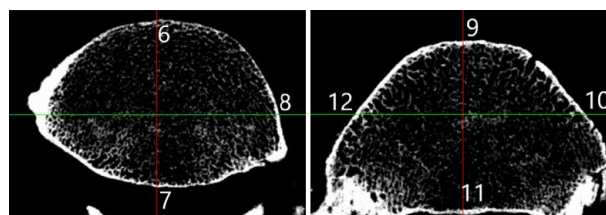


Figure 18: Cross section. Left: $X=0, Y=7, Z=6.1$; Right: $X=0, Y=7, Z=-6.1$. X: Red, Y: Green, Z: Blue.

The coordinates indicated in Figure 18 refer to the intersection point of the coloured axes, but the measurements were made at the points indicated by the numbers, with segments parallel to the axis that intersects the cortical bone at that point. The results of thickness measurement are shown in Table 4.

In addition to these thickness measurements, the surfaces were observed to evaluate the overall trend of the edges of the objects obtained with Stradwin with respect to the reference. In Figure 19, Figure 20 and Figure 21, the comparisons between the objects obtained for different line width are reported.

	Rif.	W0			W2			W4		
	90 μm	240 μm	BONE2	STD2	240 μm	BONE2	STD2	240 μm	BONE2	STD2
1	0.8	0.94	1.27	1.2	0.85	1.06	1.27	0.79	1.2	1.35
2	0.7	0.8	1.13	0.92	0.96	0.78	0.96	0.95	0.86	0.96
3	1.56	0.28	1.24	1.7	1.74	1.56	1.79	1.91	1.68	1.85
4	0.5	0.43	0.92	0.32	0.49	1.11	0.64	0.55	0.33	0.59
5	0.26	1.54	1.24	1.93	0.3	0.62	1.41	0.24	0.7	0.62
6	0.74	0.95	1.41	1.09	0.67	0.88	1.35	0.59	1.16	1.69
7	0.38	0.46	2.63	0.6	0.5	0.6	0.62	0.52	0.65	0.59
8	0.48	0.73	1.6	0.6	0.64	0.53	0.6	0.51	0.5	0.55
9	0.79	0.86	1.26	1.27	0.89	1.24	1.3	0.86	1.24	1.31
10	0.44	1.74	2.62	0.81	0.9	0.77	0.82	0.79	0.82	0.83
11	0.57	0.93	1.38	0.7	0.68	1.26	0.68	0.55	0.66	0.69
12	0.79	0.28	1.52	1.82	0.95	1.56	1.83	0.95	1.84	1.99

Table 4: Thickness measurements [mm] of the cortical bone layer of the L5 reconstruction obtained with 20 mm long line. W = line width.

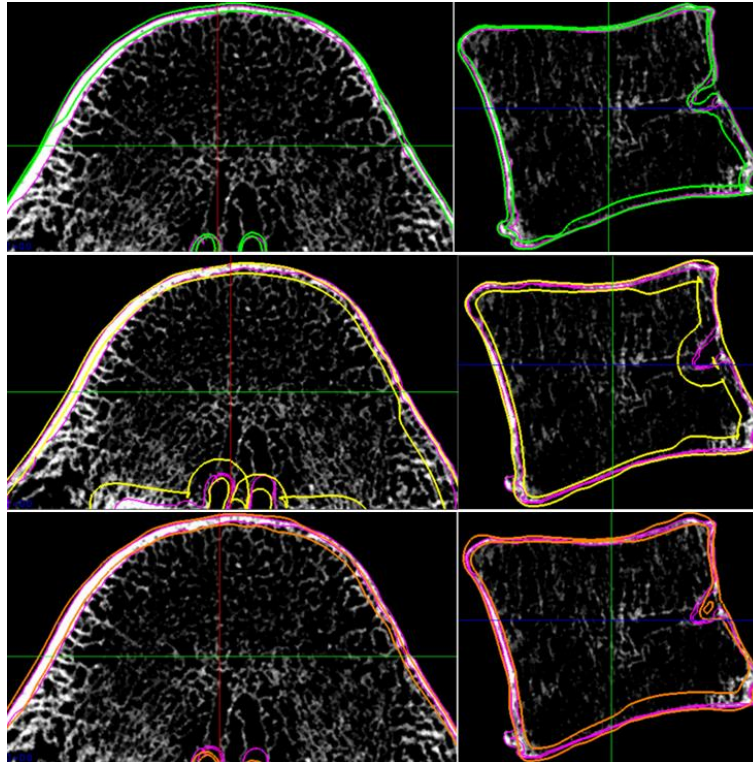


Figure 19: Line width: 0. Cross section (left) e sagittal section (right). Magenta: 90 um, Green: 240 um, Yellow: BONE2, Orange: STD2

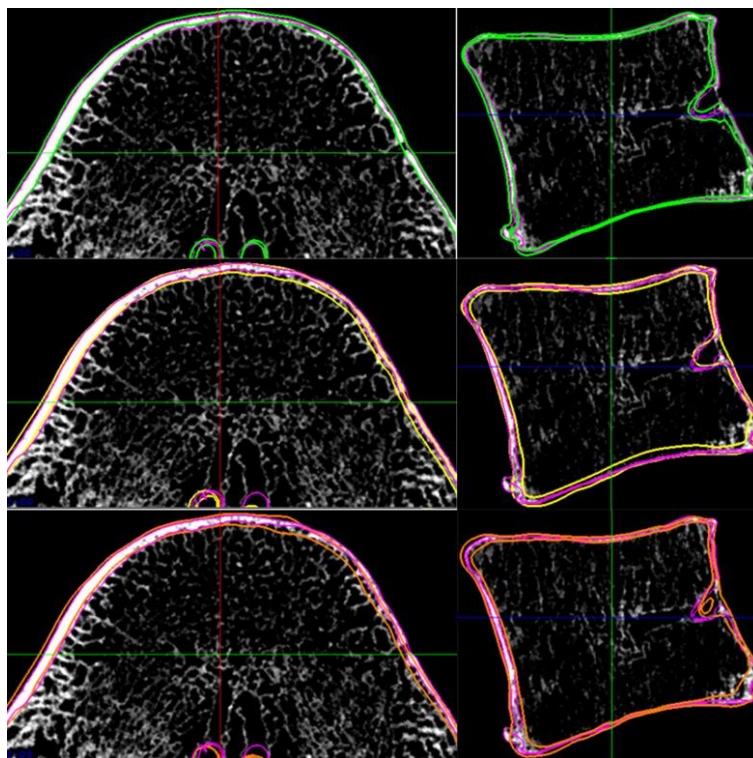


Figure 20: Line width: 2. Cross section (left) e sagittal section (right). Magenta: 90 um, Green: 240 um, Yellow: BONE2, Orange: STD2

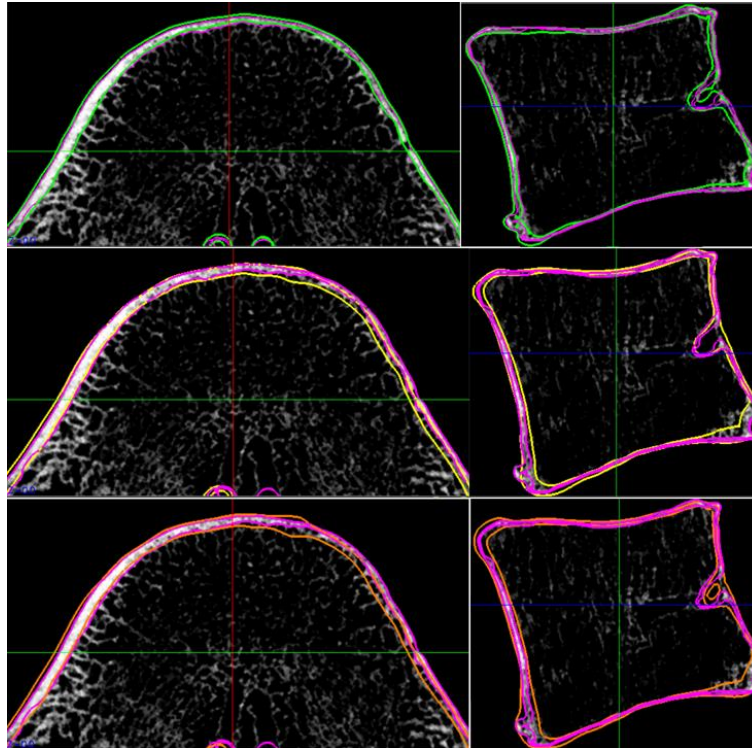


Figure 21: Line width: 4. Cross section (left) e sagittal section (right). Magenta: 90 um, Green: 240 um, Yellow: BONE2, Orange: STD2

Comparing the results, it was observed that with a line with zero thickness, big errors occurred on the endplates. With a line thickness of 2 or 4 pixels, there were no major differences in the estimate, except around the osteophytes, the processes cutting area and the posterior gaps. Overall, since greater differences are observed on the object obtained from CT-BONE2 images (set n. 7) with a thickness of the line equal to 2, compared to that obtained with a thickness of 4 pixels, we have chosen to continue in the following steps with 4 pixels' thick line.

Note that the external contour in different cases is not superimposed perfectly on the external contour of the reference object. This is due to the registration of the various external surfaces the external surface of the reference object through the Albamaster software, that uses the iterative closest point (ICP) algorithm.

In the next step, we assessed the influence of the line length on the estimates. However, it was observed that, by choosing a line length of 26 mm, the estimate failed on the object reconstructed from one of the images set n. 6 (CBCT-Newton with

0.240x0.240x0.240 mm³ resolution). For this reason, we didn't compare the objects obtained with line length of 26 mm.

We didn't observe notable differences between the various objects as the length of the line varied between 18, 20 and 23 mm, unless there were more evident differences in the area of osteophytes, gaps on the posterior wall of the vertebra and in the cutting area of the posterior processes. Anyway, differences in these areas are not of particular interest to our study and, moreover, they are very dependent on the initial segmentation, on the plan chosen for cutting the processes and, finally, on the specific properties of the bone at those points. However, by varying the length of the line from 18 mm to 23 mm, we observed that, in objects obtained from CT BONE2 and STD2 images (set n. 7-8), there is a recurrent error in the anterior area of the vertebra. In particular, there is a rough estimate, which leads to an object whose outermost edge widens beyond where it is expected to still find cortical bone. This evidence can be seen in the blue box.

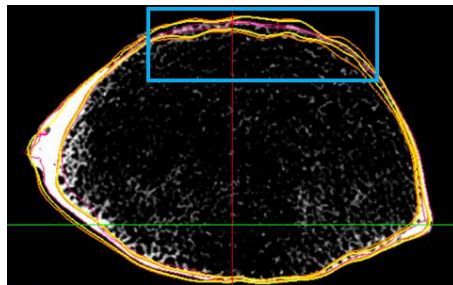


Figure 22: L5 - Cross section. Line width: 4 pixels, Line Length: 20 mm, Magenta: 90 μ m, Yellow: BONE2, Orange: STD2

By reducing the length of the line, this phenomenon is reduced. Figure 23 and Figure 24 show the comparison between objects obtained from CT-BONE2 images (set n. 7) with a line length of 12 mm and those obtained with a length of 20 mm.

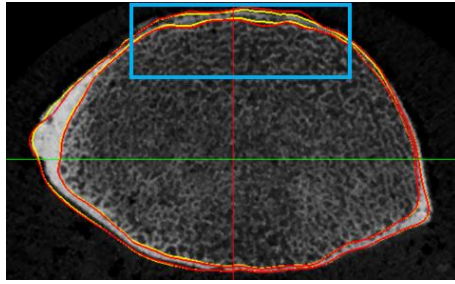


Figure 23: L5 - BONE2 - Cross section, Yellow: line length: 12 mm, Red: line length: 20 mm

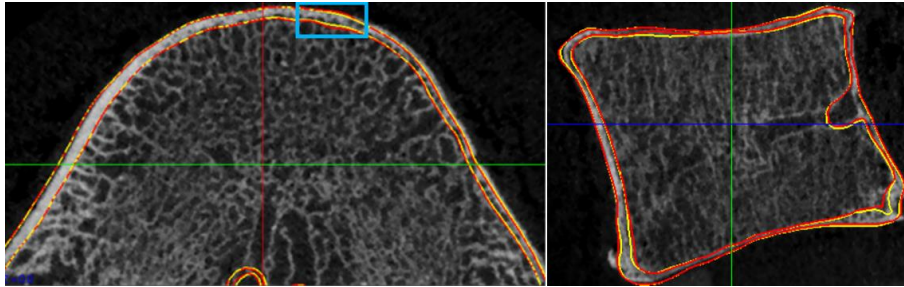


Figure 24: L5 - BONE2. Cross section (left) and sagittal section (right), Yellow: line length: 12 mm, Red: line length: 20 mm

Figure 25 and Figure 26 show the comparison between objects obtained from TC-STD2 images with a line length of 12 mm and those obtained with a length of 20 mm, in the same section observed previously.

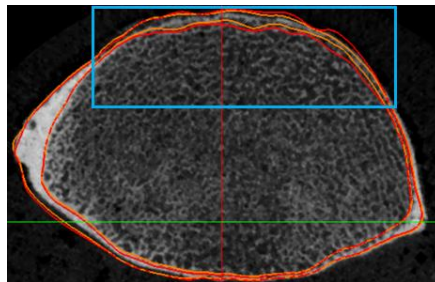


Figure 25: L5 - STD2 - Cross section, Yellow: line length: 12 mm, Red: line length: 20 mm

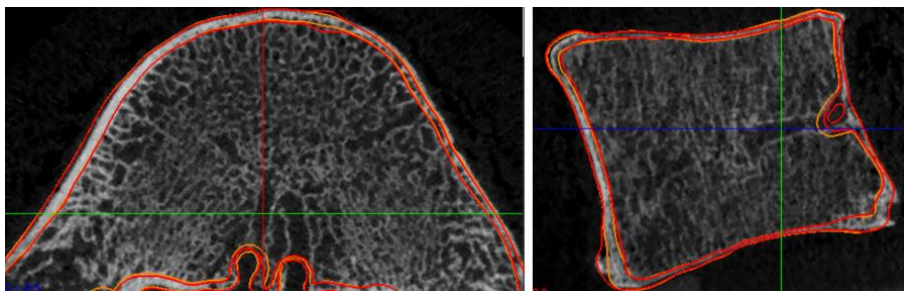


Figure 26: L5 - STD2. Cross section (left) and sagittal section (right), Orange: line length: 12 mm, Red: line length: 20 mm

The results obtained for CT-240 μm are also reported in Figure 27, although there was no problem in the anterior area. In this case, an almost complete overlap is observed, passing from the estimate with 12 mm to that with 20 mm line length, except in the area of osteophytes or posterior gaps.

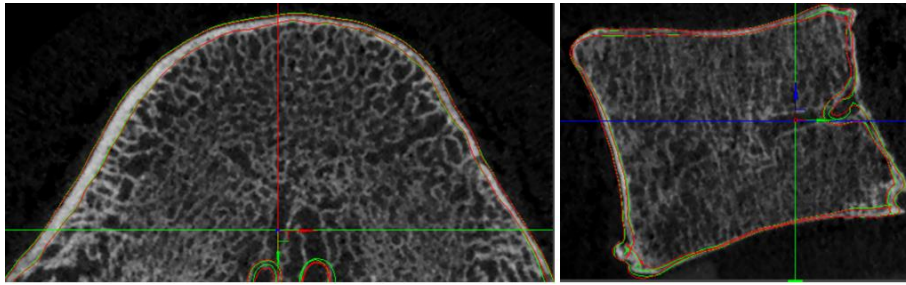


Figure 27: L5 – 240 μm . Cross section (left) and sagittal section (right), Green: line length: 12 mm, Red: line length: 20 mm

Subsequently, we repeated the tests by adopting a 'Very high' level of smoothing. For these tests, line length of 12 mm was used. The results were compared with those obtained with the 'Medium' smoothing level. The objects obtained from CT-240 μm images (set. 6) don't show great differences when the line thickness is 2 or 4 mm, except next to the posterior cut processes, posterior lacunae and osteophytes (Figure 28). Setting a zero thick line, on the other hand, we observed that, with 'very high' smoothing, the estimate is good in the lower endplate, i.e. results are closer to the reference object, but worse in the upper one (Figure 28).

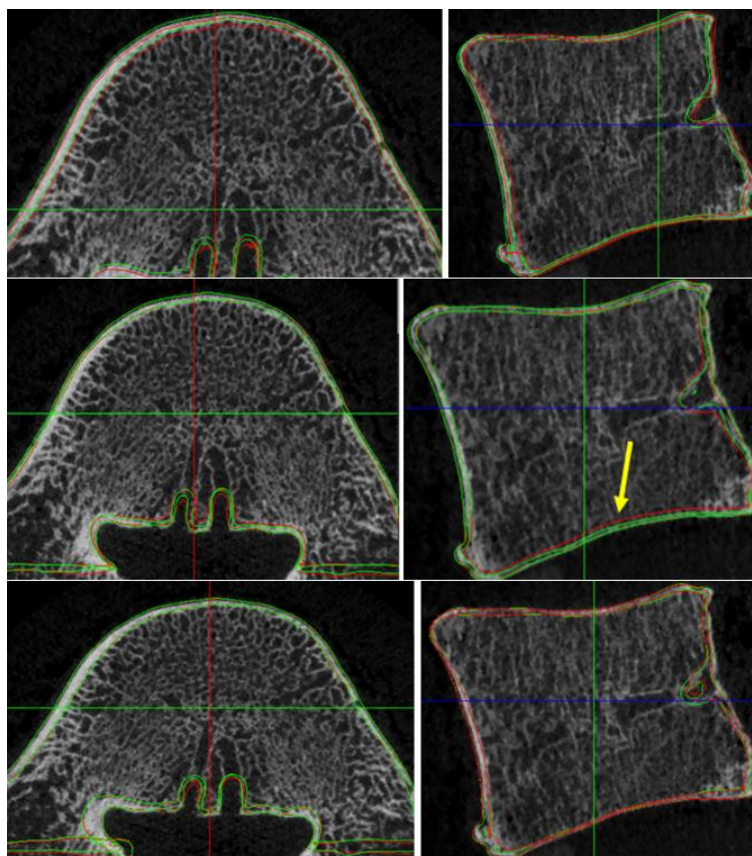


Figure 28: L5 - 240 μm . Cross section (left) and sagittal section (right). Line width: 0 (upper), 2 (middle), 4 (lower). Red: smoothing 'very high', Green: smoothing 'medium'.

The objects obtained from CT-BONE2 images are quite similar with different smoothing levels when the thickness of the estimate line is zero, with the exception of the processes cutting area, the posterior gaps and the lower endplate (Figure 29). A comparison with the reference object can be seen in the lower part of the Figure 29. With a 2 pixels thick line, the objects show obvious differences on the endplates (Figure 30) by comparing them with each other. Overall, there are obvious differences in the same areas with the reference object (Figure 30). With a 4 pixels thick line and a 'very high' smoothing level, the estimate is closer to the reference object, in particular on the lower endplates (Figure 31). A comparison can be observed in Figure 32.

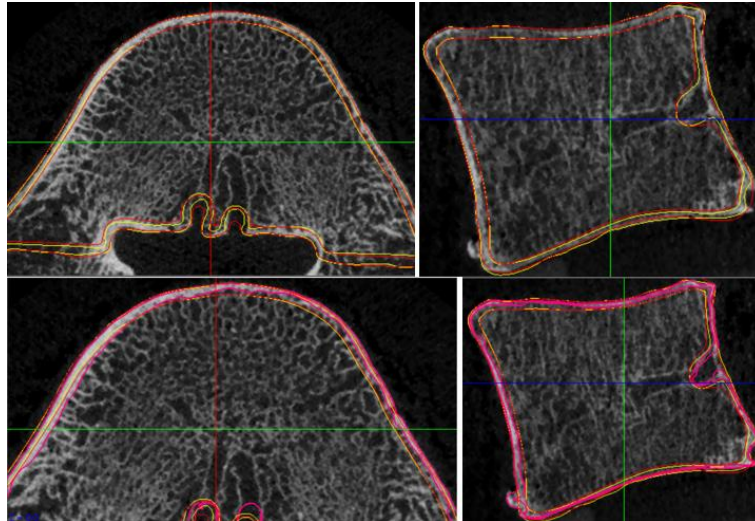


Figure 29: L5 - Cross section (left) and sagittal section (right), line width: 0.
Red: BONE2 Smoothing Very high, Yellow: BONE2 Smoothing Medium; Magenta: 90 μ m.

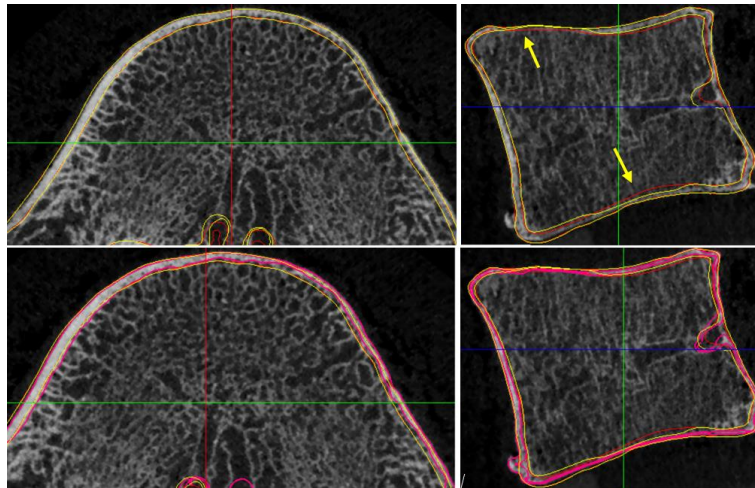


Figure 30: L5 - Cross section (left) and sagittal section (right), line width: 2.
Red: BONE2 Smoothing Very high, Yellow: BONE2 Smoothing Medium; Magenta: 90 μ m

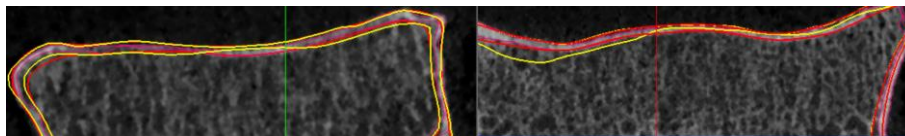


Figure 31: Lower endplate, line width: 4. Red: BONE2 Smoothing Very high, Yellow: BONE2 Smoothing Medium;
Magenta: 90 μ m.

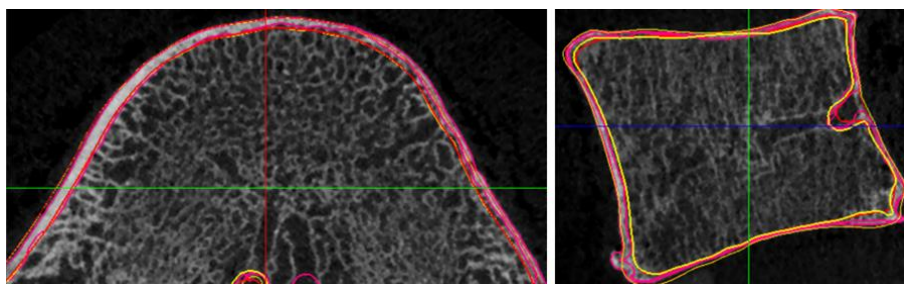


Figure 32: L5 - Cross section (left) and sagittal section (right), line width: 4.
Red: BONE2 Smoothing Very high, Yellow: BONE2 Smoothing Medium; Magenta: 90 um

Overall, we observe an object closest to the reference one when the line thickness is set on 4 pixels and the smoothing is 'Very high', compared to that obtained with a line thickness equal to zero or equal to 2 pixels with 'medium' or 'very high' smoothing level.

The objects obtained with CT-STD2 images (set n. 8) didn't show significant differences changing the smoothing level when the line width used for the estimate is 0, 2 or 4 pixels. We noticed an exception near the osteophytes, the posterior lacunae and the cutting of the posterior processes (Figure 33), but these areas are not of great interest.

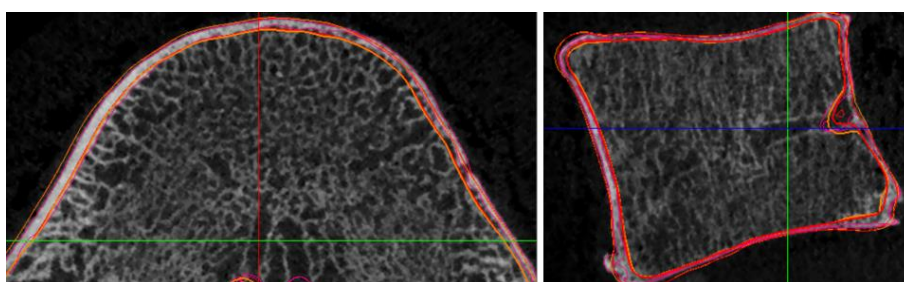


Figure 33: L5 - Cross section (left) and sagittal section (right), line width: 4.
Red: STD2 Smoothing Very high, Orange: STD2 Smoothing Medium; Magenta: 90 um

- L4 vertebra

Starting from the results obtained with the L5 vertebra, we proceeded carrying out evaluations on the L4 vertebra. In absence of a reference object for this vertebra, our main aim was to verify if, varying the Stradview parameters as we did for L5, the

same trends of cortical properties were observed for L4. The cortical bone thickness variation between the objects obtained from the different image sources available for L4, as the parameters changed, has been assessed. Also for the L4 vertebra, thickness measurements were made at the points indicated in Figure 34 and Figure 35.

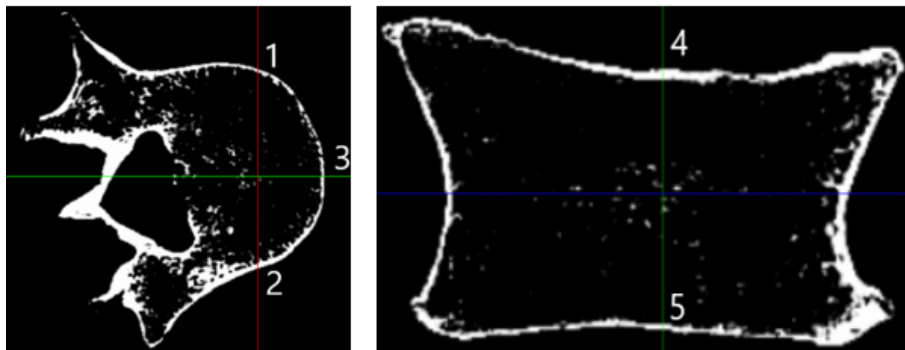


Figure 34: Cross plane (left) and sagittal plane (right). $X=92, Y=50, Z=15$. X: red, Y: green, Z: blue.

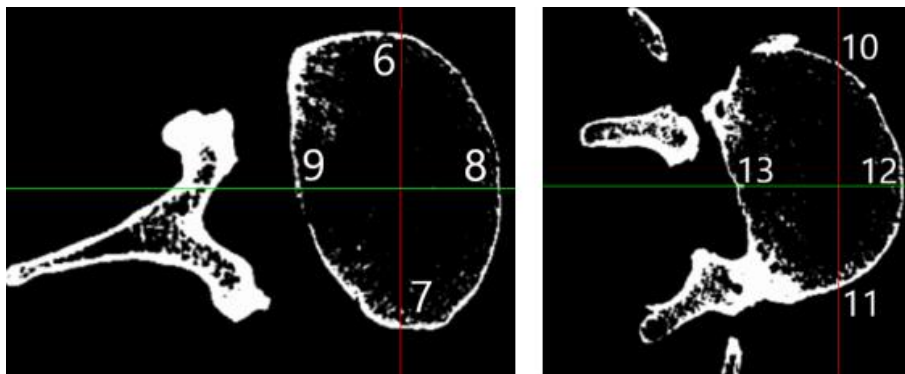


Figure 35: Cross plane. Left: $X=92, Y=50, Z=22$. Right: $X=92, Y=50, Z=7.5$. X: red, Y: green, Z: blue.

In the latter case, the reference system used is the absolute system of the image set n. 3 (L4-CBCT) in Table 3. In Table 4, thickness measurements are resumed.

We observed that for $W = 0$, there are sharp differences between the cortical bone thickness measurements. By increasing the thickness of the line up to 4 pixels, the differences are reduced. As for L5 vertebra, therefore, it seems appropriate to use a line with a non-zero thickness. In Figure 36, Figure 37 and Figure 38, there is a comparison between the objects obtained from different image sources and with different thicknesses of the line.

	W0			W2			W4		
	CBCT	BONE2	STD2	CBCT	BONE2	STD2	CBCT	BONE2	STD2
1	0.58	0.62	0.93	0.47	0.65	1.12	0.46	0.75	1.14
2	1.05	1.13	0.97	0.96	0.81	0.98	0.99	0.68	0.96
3	0.31	0.45	1.26	0.43	0.91	1.44	0.41	1	2.1
4	0.32	0.81	0.81	0.81	0.74	0.86	0.7	0.73	0.91
5	0.96	0.58	0.56	0.21	0.48	0.6	0.46	0.45	0.61
6	0.62	0.72	0.76	0.45	0.62	0.85	0.37	0.58	0.8
7	0.41	1.11	0.66	0.54	0.58	0.67	0.52	0.48	0.64
8	0.35	1.25	1.21	0.2	1.07	1.49	0.21	1.88	2.95
9	0.48	1.16	0.46	0.6	0.39	0.47	0.47	0.33	0.46
10	0.77	1.27	1.18	0.33	0.98	1.21	0.3	0.97	1.16
11	0.94	1.25	1.14	0.92	1	1.18	0.9	0.88	1.16
12	0.99	0.45	1.38	0.38	0.6	1.29	0.36	0.93	2.31
13	0.37	0.99	0.39	0.4	0.29	0.39	0.35	0.25	0.37

Table 5: Cortical thickness [mm] of L4 vertebra. Line length. 20 mm. W: line width [pixels]

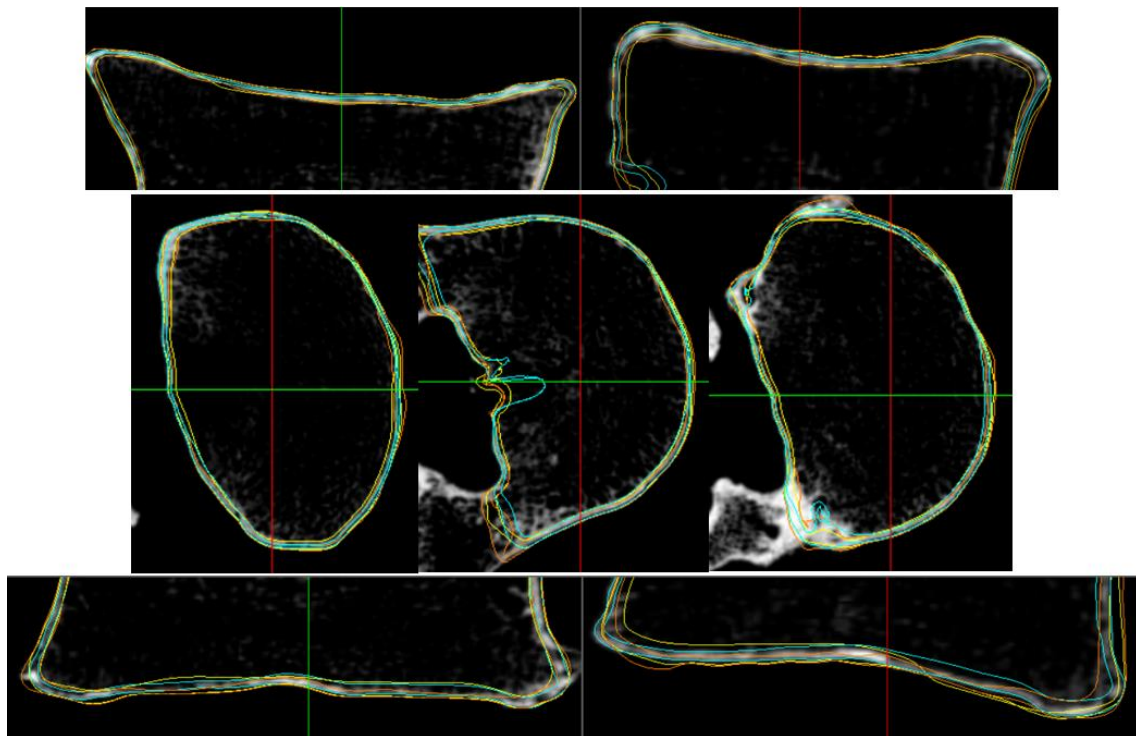


Figure 36: L4 – Line width: 0, Line length: 20 mm, Ciano: CBCT, Orange: STD2, Yellow: Bone2. Above: lower Endplate, Middle: cross sections, below: upper endplate

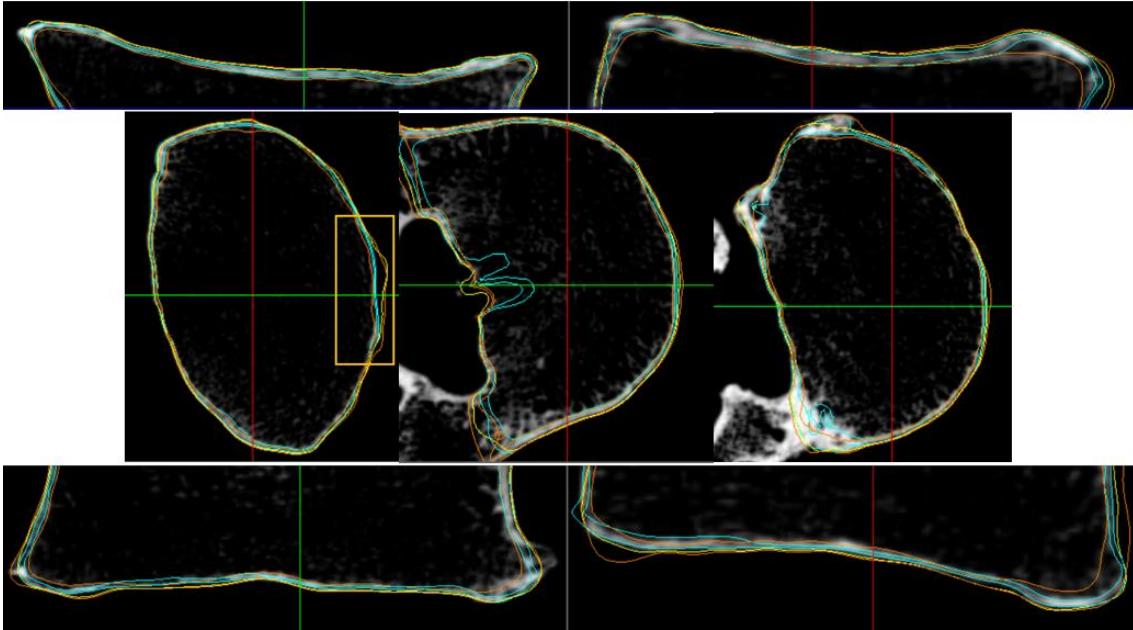


Figure 37: L4 – Line width: 2, Line length: 20 mm, Ciano: CBCT, Orange: STD2, Yellow: Bone2. Above: lower Endplate, Middle: cross sections, below: upper endplate

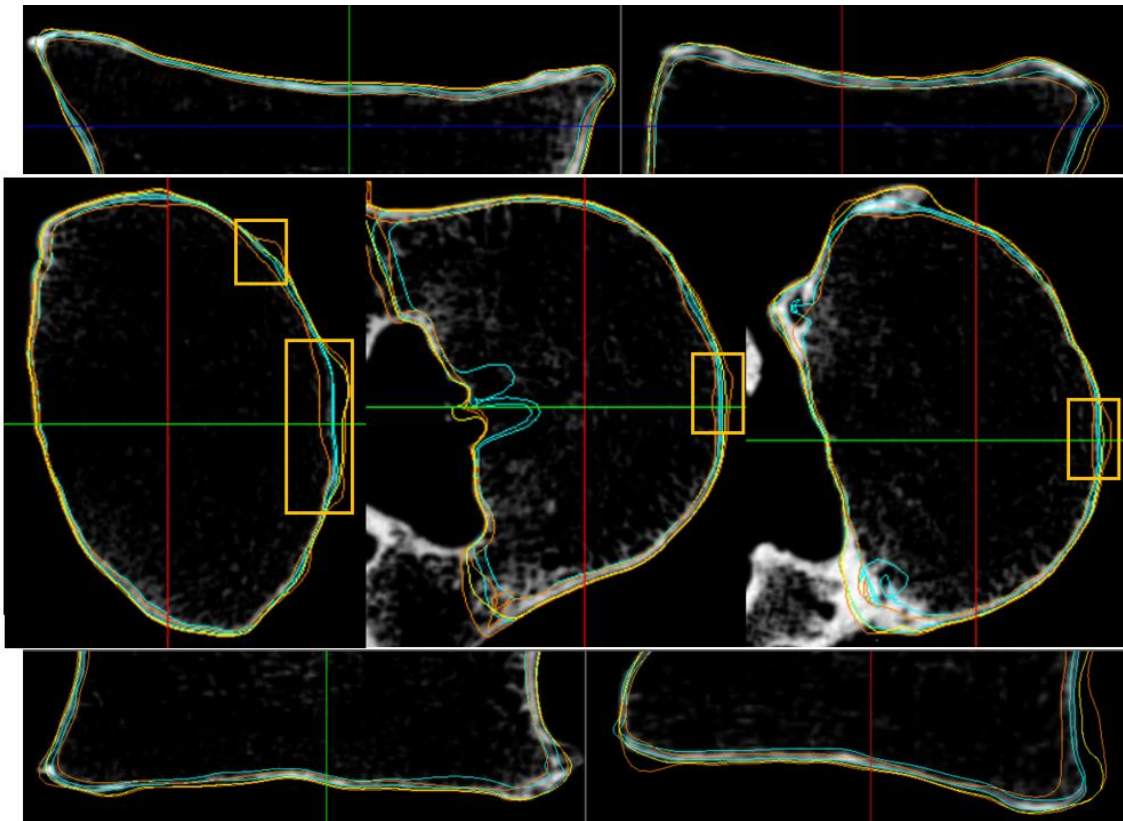


Figure 38: L4 – Line width: 4, Line length: 20 mm, Ciano: CBCT, Orange: STD2, Yellow: Bone2. Above: lower Endplate, Middle: cross sections, below: upper endplate

Also in this case, we observed a recurring error on the anterior area of the L4 vertebra when the thickness of the line is greater than 0. On the other hand, with a 12 mm long line. there is a reduction in the burrs, as shown in Figure 39.

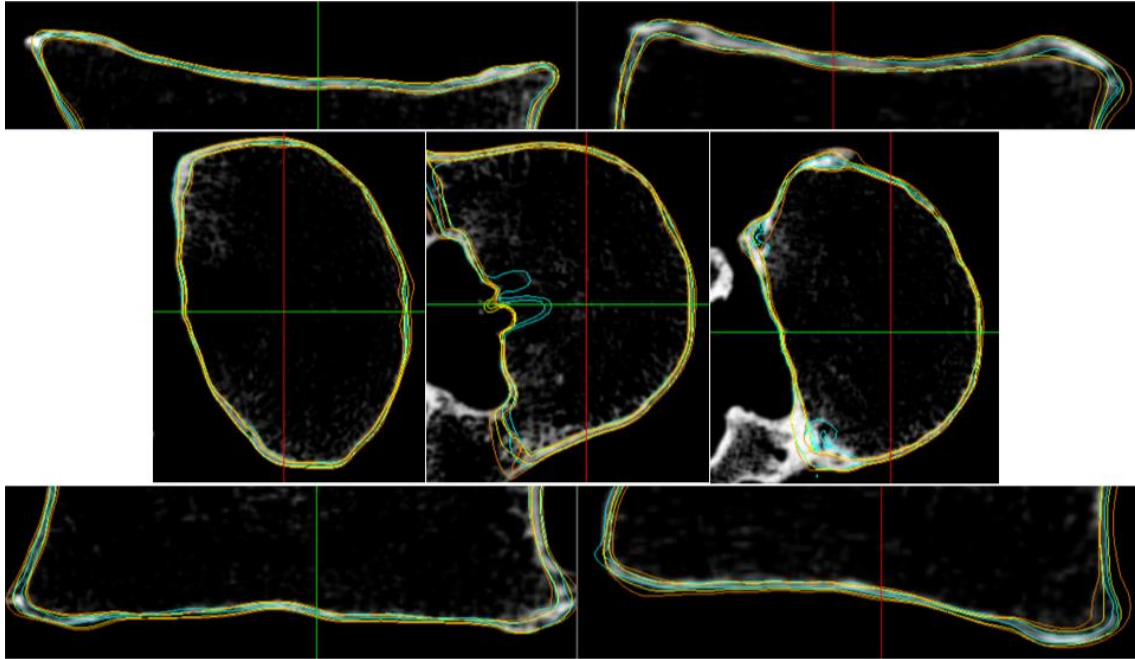


Figure 39: L4 – Line width: 4, Line length: 12 mm, Ciano: CBCT, Orange: STD2, Yellow: Bone2. Above: lower Endplate, Middle: cross sections, below: upper endplate

Furthermore, there is a lesser difference between the surfaces obtained from different images sources, when the line length is set on 12 mm. In the next step, we assessed the influence of the smoothing level. In the objects obtained from the estimate on CBCT images (set n. 3), we didn't observe differences with varying the level of smoothing from 'medium' to 'very high', with the exception of the areas near the rear holes (Figure 40).

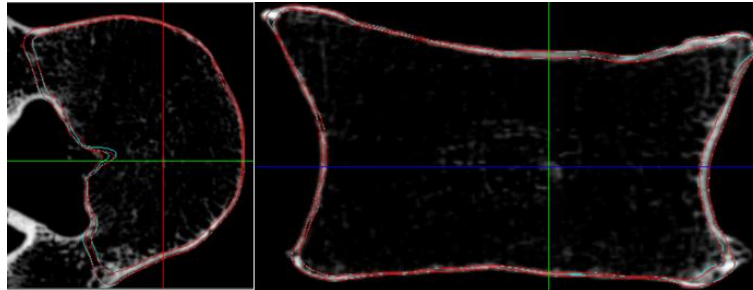


Figure 40: L4 - CBCT – Cross section (left) and sagittal section (right), Line width: 4, Length: 12 mm, Ciano: medium smoothing, red: very high smoothing.

In the objects obtained from the estimate on STD2 images (set n. 2), we observed more differences especially on the upper endplate, where there is even an intersection of the outer edge with the inner one when the level of smoothing is set on 'very high' (Figure 41).

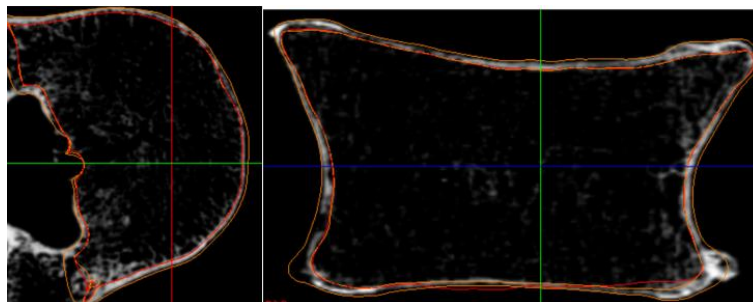


Figure 41: L4 – STD2 – Cross section (left) and sagittal section (right), Line width: 4, Length: 12 mm, Orange: medium smoothing, red: very high smoothing.

Finally, in the objects obtained from BONE2 images (set n. 1), there are no noticeable differences when we change the level of smoothing (Figure 42).

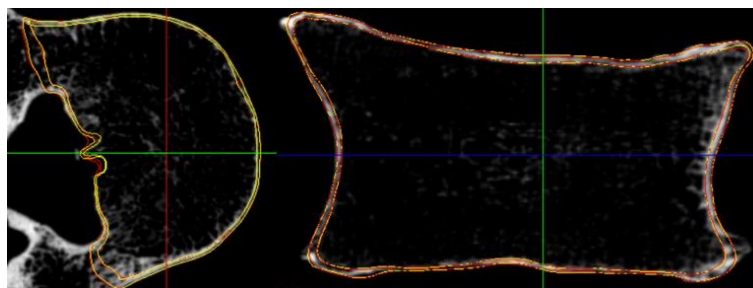


Figure 42: L4 – BONE2 – Cross section (left) and sagittal section (right), Line width: 4, Length: 12 mm, Orange: medium smoothing, red: very smoothing

- **Inter-subject variability and vertebral level**

The second part includes the evaluation of the influence of the donor on the estimation and also of the vertebrae position. We used the same approach and we drew similar conclusions. In this case, we compared the object got from the estimation on 3 coupled DICOM sets (n. 9-10, 11-12, 13-14). The first one of the couple was the reference one, because of the better properties of the scans. This data set include the scans of 3 thoracic vertebrae. So, we also investigated about the influence of the vertebral level. We started again investigating the effect of the line width, with a line length set to 20 mm. In this case, the improvement in the estimate with a greater line thickness was not immediately evident. An example is shown in Figure 43.

For this reason, we tried to reduce the line length, from 20 mm to 8 mm, looking, at the same time, at the changes with the line width too. After a first observation, it was quite obvious that the line length had to be reduced to avoid the bulges (Figure 44).

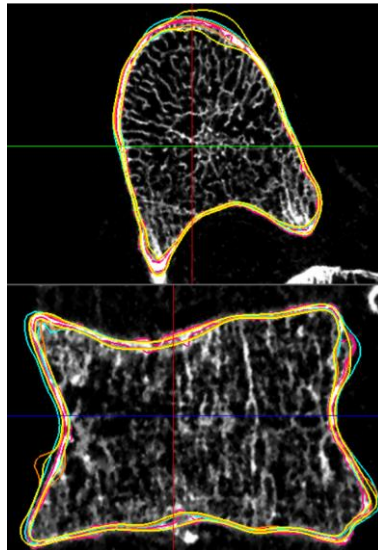


Figure 43: T7. Magenta: CBCT (reference), Ciano: $W=0$, Orange: $W=2$, Yellow: $W=4$

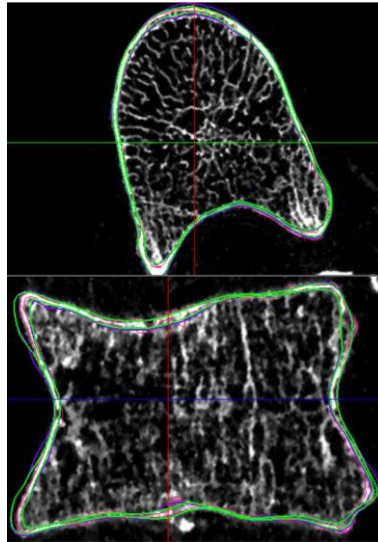


Figure 44: T7. Magenta: CBCT (reference), Purple: $W=0$, Green: $W=4$

Again, we set the smoothing to medium and we didn't change the maximum allowed angle and the maximum offset.

Finally, we tried to reduce again the line length, setting it to 6 mm. This estimation has been done by setting the line width to 4 pixels. The result was not consistently different from the result obtained by setting the line length to 12 mm. the objects are practically superimposed, but there were slight differences in the endplates zone (Figure 45).

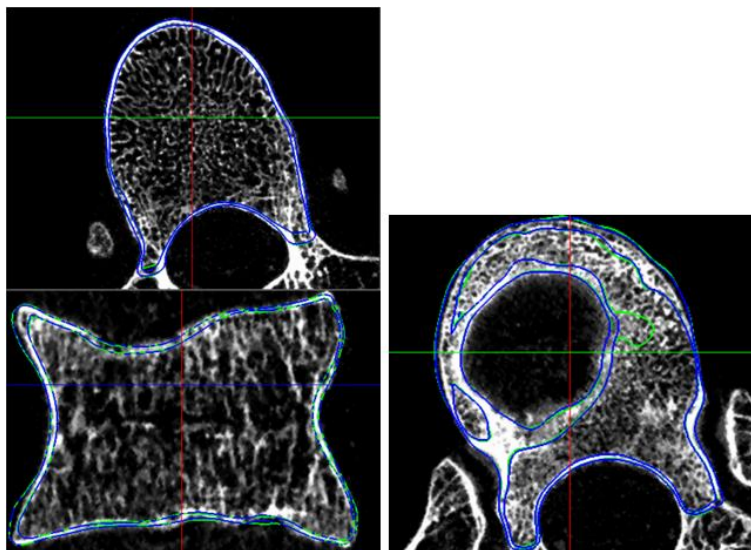


Figure 45: Blue: line length 6 mm, Green: line length 12 mm. Right: cross section of the upper endplate.

These observations allowed us to draw some conclusions. By varying the line thickness, null line thickness leads to an overestimation of the thickness of the cortical bone, regardless of the source of the images. From the results obtained in this study, it is clear that it is appropriate to use a line with a non-zero thickness, unless estimation errors are made in areas with particular geometry or cortical properties. A relevant parameter is the choice of the length of the line. The line length must be 3 times the maximum measured thickness. However, the vertebral cortical bone has a very particular geometry. In some areas, the thickness is sub-millimetric; in other ones, it is clearly greater, e.g. next to the posterior processes or on the endplates. So, it seems appropriate to select a line slightly longer than the maximum measured thickness, in order to avoid overstating the thickness in areas where the latter is very thin. As regards the maximum acceptable distance, it has been observed that, for the same maximum acceptable angle, there is no variation in the results. As for the maximum acceptable angle, it was not possible to find a common thread among the results. In particular, it seems appropriate not to select a much lower angle than the default value. Finally, no significant differences were observed on the vertebral body when the level of smoothing changed from 'medium' to 'very high' in most cases. On the endplates, however, a better estimate was observed in some cases with higher smoothing.

Finally, we choose to create the first model with the object, got from the estimation of cortical density of the L5 vertebra, starting from scans taken with BONE2 kernel and with a 8 mm long and 4 pixels thick line, because it represents the best estimation (Figure 46). Moreover, we chose to start with the L5 vertebra because it was the first specimen to be experimentally test. Therefore, the comparison between the results got from both the simulation and the mechanical tests will be the first attempt of validation.

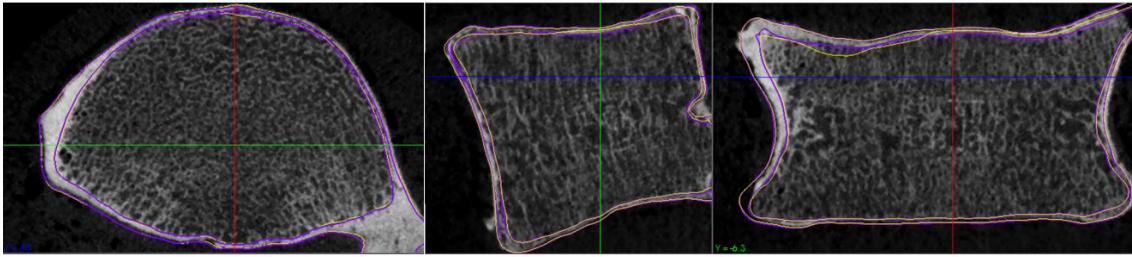


Figure 46: L5 – BONE2. Line width: 4 pixels, Smoothing: Medium, Yellow: Line length: 12 mm, Purple: line length: 8 mm

3.1.5 Patches and NURBS construction

After choosing the object to start from, we imported the wrl file, got from Stradview, in Geomagic Studio (Geomagic Studio v. 7, Raindrop Geomagic, Inc., USA). We first constructed the patches. This network has been realized paying attention to mark the regions and the curvatures of major interest, without an excessive number of patches. This lattice works as base on which generate a mesh, but it hasn't to be too much dense, because it could reduce the mesh quality, forcing it to converge in too many points.

Subsequently, a grid has been realized on the patches. This grid has been modified in some areas to better recover the reconstructed vertebra. Finally, we obtained the NURBS (Non-Uniform Rational Basis Spline) representations of surfaces, which are a mathematical representation, useful to create geometric objects and to define accurately their shape. Definitely, we got the IGES models. An example is shown in Figure 47.

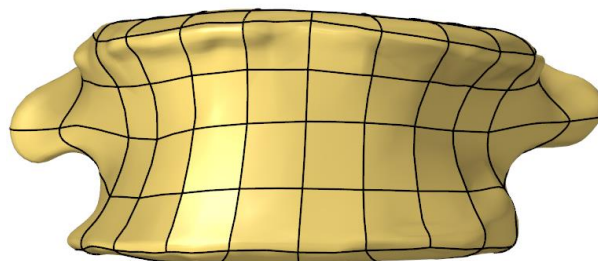


Figure 47: Example of patches and NURBS

3.1.6 Mesh generation

The following step was the generation of the mesh from IGES models. For this purpose, we used the Hypermesh software (Hypermesh 13.0, Altair Engineering Inc., USA).

We chose the size of the elements starting from a convergence analysis, previously carried out by the group. The aim of this analysis was to obtain a mesh as regular as possible, with elements of almost uniform size and finally a good ratio between mesh yield and computational cost. They varied the element size between 1 mm, 1,5 mm, 2 mm and 3 mm. Then, they compared the results of the model solving and verified the convergence of the model, in order to choose the most suitable element size. They observed that the performances were similar when the element size were 1 mm or 1,5 mm. However, the computational time was significantly reduced with 1,5 mm elements. Therefore, they realized the later models setting the element size to 1,5 mm. Starting from these observations, we first generated a two-dimensional mesh for both the trabecular and the cortical compartments. The chosen element size was 0.75 mm. Starting from the trabecular surface mesh, we generated three-dimensional tetrahedral one of the trabecular compartment, by setting a growth factor of 1.2 and the maximum element edge length to extend inward to 2 mm. Starting from the trabecular and cortical surface meshes, we realized the cortical tetrahedral mesh but by setting the growth factor to 1. In fact, we chose an elements size equal to 0.75 mm just to model adequately the submillimetric thickness of cortical bone, although this may require a higher computational cost. We obtained 115669 elements and 193525 elements for the cortical and trabecular compartments respectively. The generation of the cortical volume mesh required more precautions because of the small thickness of the cortical compartment. The risk was of having too distorted elements. However, we set up a mesh quality check and verified its good performance, as shown in the following table and figures.

Checked parameters	Failed elements
<i>Volume aspect ratio</i> > 5	69 of 115669
<i>Volume skew</i> > 0.95	3 of 115669
<i>Tetra collapse</i> < 0.1	0 of 115669

Table 6: Cortical 3D mesh - quality check

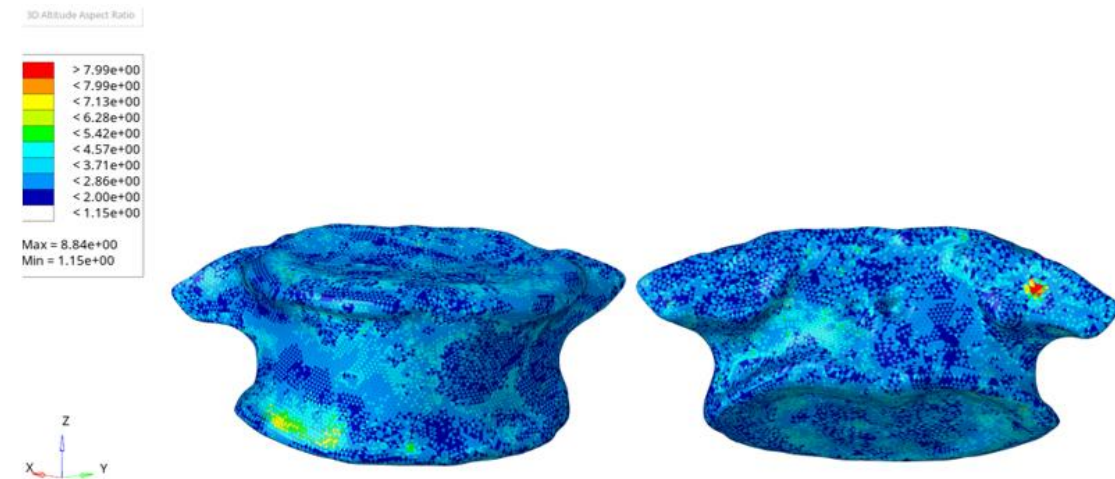


Figure 48: Cortical compartment - 3D Altitude Aspect ratio

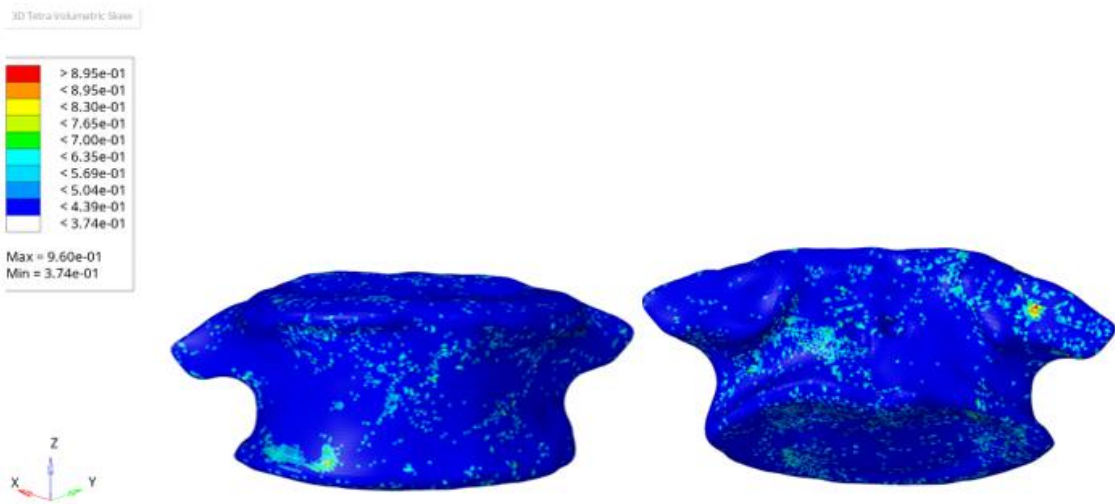


Figure 49: Cortical compartment - Tetra volumetric skew

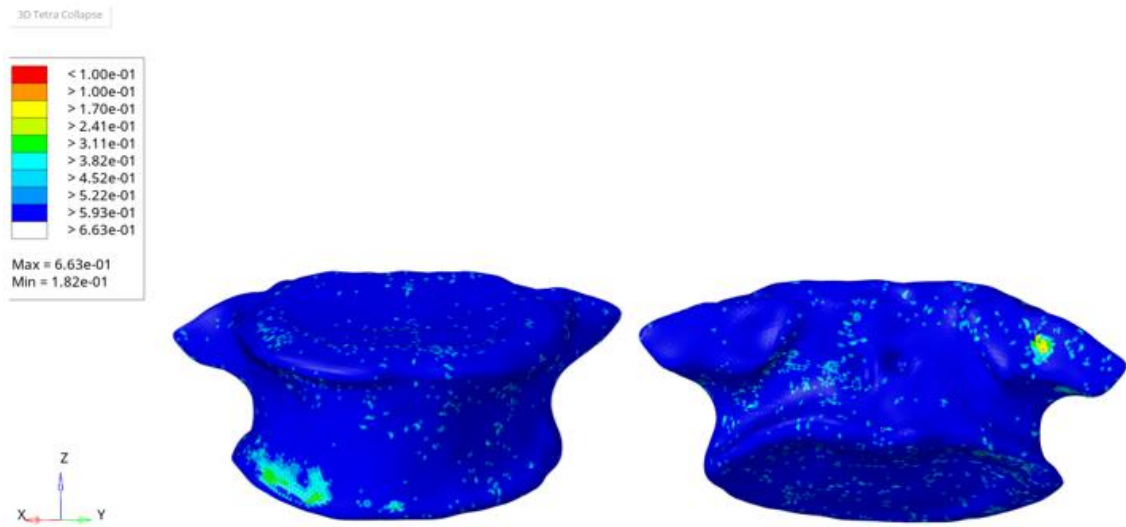


Figure 50: Cortical compartment - 3D Tetra collapse

For both the trabecular and cortical volume mesh, we changed the element order from first to second order. Therefore, the final element had 10 nodes, 4 of them on the vertices of the tetrahedron and the remaining ones on the middle of the edges, as shown in Figure 51.

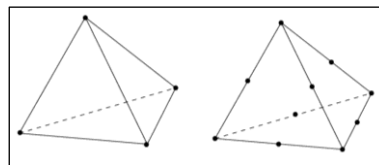


Figure 51: First order element (left) and second order element (right)

So, we obtained 284938 and 210988 nodes for the trabecular and cortical compartments respectively.

Lastly, we assigned an element type to each element, i.e. SOLID187 in Ansys Mechanical APDL, that is characterized by 10 nodes and 3 degrees of freedom, consisting of three components of translations. The resultant meshes are shown in Figure 52.

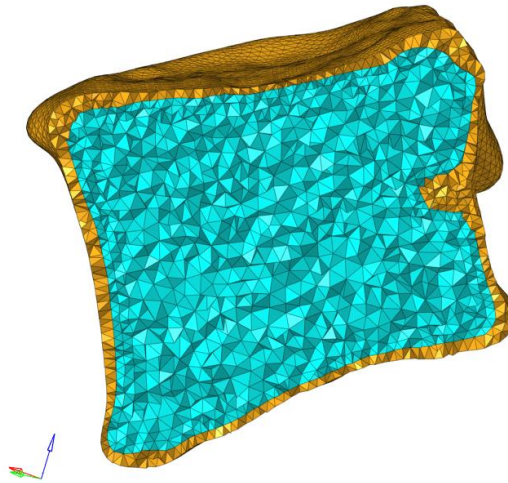


Figure 52: Cortical (orange) and trabecular (ciano) meshes

3.1.7 Assignment of material properties

The following modelling step dealt with the derivation of inhomogeneous elastic bone properties, starting from HU values. For this purpose, we implemented some relationships on Bonemat software (Bonemat v 3.2, BIC laboratory, Istituto Ortopedico Rizzoli in Bologna, Italy).

Bonemat algorithm performs a numerical integration of the voxel-wise properties and assigns a material property to each finite element, deriving it from Hounsfield Unit (HU) of the tissue in the correspondent region. Therefore, a mesh grid with element-wise properties could be then exported to FE solvers, like Ansys. Each element will have an assigned elastic modulus and the elements will be divided in groups by their material card. In the export step, it is also possible to specify the minimum gap between two subsequent material cards, to avoid the definition of too many different materials. The common procedure consists of:

1. Extraction of the density values (ρ_{QCT}) by *the relationship of CT densitometric calibration*:

$$\rho_{QCT} = a + bHU$$

Equation 3.1

The Hounsfield Units (HU) are used to express the grey levels of the voxels of the CT images. The CT scans are usually performed with a calibration phantom; so that, the relationship (above) must be introduced to transform the HU values in radiological density (ρ_{QCT}). The calibration coefficients (a and b) are, respectively, the intercept of the calibration line and the slope.

In our case, for the data set CT-BONE2 (set n. 1 and 7 in Table 3), the relationship is:

$$\rho_{QCT} = -0.008561 + 0.000818 * HU$$

Equation 3.2

This relationship allows to obtain a value of radiological density for each mesh element. The ρ_{QCT} unit of measure is g/cm^3 .

2. **Correction of the densitometric calibration.** This correction has been introduced because it has been shown that densitometric phantoms lead to some errors when mimicking bone characteristic [80].

This deals with a linear relationship between the ρ_{QCT} and the ash density ρ_{Ash} , i.e. the mineral mass of the bone on the total volume of the specimen.

$$\rho_{Ash} = \frac{\rho_{QCT}}{\gamma} + \frac{\delta}{\gamma}$$

Equation 3.3

According to the cited paper, the values of γ are 0.98 and 1.14 for the trabecular and cortical compartments respectively. Therefore, the final relationships are:

$$\rho_{Ash} = 1.02409\rho_{QCT} + 0.051 \text{ for the trabecular compartment}$$

Equation 3.4

$$\rho_{Ash} = 0.934579\rho_{QCT} - 0.009345 \text{ for the cortical compartment}$$

Equation 3.5

3. Calculation of the elastic modulus (E) by applying a ***density-elasticity relationship***, relating the bone density to bone elastic modulus:

$$E = a + b\rho_{Ash}^c$$

Equation 3.6

This relationship can be chosen in the literature.

We selected two different laws, one for the trabecular compartment and another for the cortical compartment.

For the trabecular and the cortical compartments, we introduced the relationship described by Morgan et al., conceived for vertebrae T10-L5 and for $0.11 \leq \rho_{App} \leq 0.3 \left[\frac{g}{cm^3}\right]$ [46]:

$$E = 4730 * \rho_{App}^{1.56}$$

Equation 3.7

These relationships are reported in the papers in terms of wet density ρ_{App} , i.e. the hydrated mass of the tissue on the total specimen volume. We also introduced the ratio $\rho_{Ash}/\rho_{App}=0.6$ to convert the apparent wet density ρ_{App} in ρ_{Ash} , as indicated by Schileo et al. for human femur [80]. The Poisson ratio for the trabecular compartment was set to 0.3. In the latter, we used the ‘Bonemat’ operation, by applying the previous relationships to all CT voxels,

within the correspondent volume mesh. Therefore, we obtained an ‘updated’ FE mesh with elastic properties mapped on each element.

For the cortical layer, the Poisson ratio was set to 0.4. In this compartment, we used the ‘Bonemat from Stradwin surface’ operation. The latter need more inputs, i.e. the BIN file containing the density values got from Stradview and the outer surface of the vertebra reconstruction. Then a numerical integration likewise is carried out but starting from the cortical density estimates from CBM.

Lastly, we introduced a threshold to the estimation of the Young moduli both of the cortical and the trabecular compartments, to avoid unreliable density values. We, firstly, decided to filter all the values of Young modulus (E) lower than 4500 MPa for the cortical, to exclude the possible outliers generated by the non-linear optimisation of the CBM-v2 algorithm[47]. This value was the lower E of the cortical bone measured among a series of specimens, including child bone too [81].

$$E_{MIN_cortical} = 4500 \text{ MPa}$$

We also introduce a filter on the E values of the trabecular compartment to avoid the double-counting of cortical density, that could occur for the data on the interface between cortical and trabecular bone (Figure 53).

$$E_{MAX_trabecular} = 4500 \text{ MPa}$$

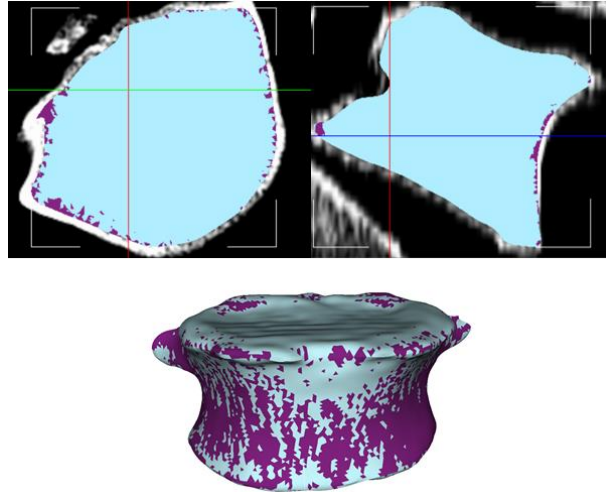


Figure 53: Filtered data on the trabecular surface. Purple: $E > 4500$ MPa, Light blue: $E < 4500$ MPa.

3.1.8 Cortical and trabecular transversal isotropy

In our models, we also decided to assign transverse isotropy properties to the modelled bone, according to the laws provided by Crawford et al. [82] and Dong et al. [83] for the trabecular and cortical compartment respectively. The transversal isotropic materials are included in the class of the anisotropic ones. A transversely isotropic material shows the same properties in all directions on a plane of isotropy and symmetric properties about an axis that is normal to this plane. The elasticity tensor contains five independent constants on twenty-one in the case of a fully anisotropic material. The elastic behaviour of this kind of materials is characterized by [83]:

- E_L = longitudinal Young's modulus
- E_T = transverse Young's modulus
- G_L = longitudinal shear modulus
- G_T = transverse shear modulus
- ν_L = longitudinal Poisson's ratio

So that, after the determination of the Young's modulus ($E_L = E_{yy}$) by the procedure described above, the constants were assigned assuming the transverse isotropy, implementing the following relationships.

For the trabecular compartment, we introduced the equations cited by Crawford et al.:

$$\begin{aligned}
 E_L &= E_{yy}, \\
 E_T &= E_{xx} = E_{zz} = 0.33 * E_{yy}, \\
 \nu_T &= \nu_{xz} = 0.3, \\
 \nu_L &= \nu_{xy} = \nu_{zy} = 0.104, \\
 G_T &= G_{xz} = 0.121 * E_{yy}, \\
 G_L &= G_{xy} = G_{zy} = 0.157 * E_{yy},
 \end{aligned}$$

remembering that, for instance, the Poisson's ratio $\nu_L = \nu_{xy}$ denotes the strain in the y direction divided by the strain in the x direction in response to a load in the x direction[82].

For the cortical layer, we introduced the ratios' value between E_L and the other constants, derived from the studies conducted by Dong et al. [83]:

$$\begin{aligned}
 E_L &= E_{yy}, \\
 E_T &= E_{xx} = E_{zz} = 0.59 * E_{yy}, \\
 \nu_T &= \nu_{xz} = 0.4, \\
 \nu_L &= \nu_{xy} = \nu_{zy} = 0.104, \\
 G_T &= G_{xz} = 0.2 * E_{yy}, \\
 G_L &= G_{xy} = G_{zy} = 0.29 * E_{yy}.
 \end{aligned}$$

These relationships have been inserted in the Ansys Macro Code.

3.2 Experimental set up

As said before, one of the aim of the work was to compare the results of the models with the experimental one. The L5 vertebra has been the first specimen mechanically tested. These tests have been carried on by the researchers' group of the Medical Technology Laboratory of the Rizzoli Orthopaedic Institute. In this section, there will be a brief description of the procedure of the experimental testing.

3.2.1 Specimen preparation

The specimen was cleaned and the soft tissues were removed. The posterior processes were cut. Then, the specimen has been aligned according to the reference system described by Panjabi et al. [84] (Figure 54) and the tangent planes to the lower and upper endplates and the median plane of the vertebra have been identified.

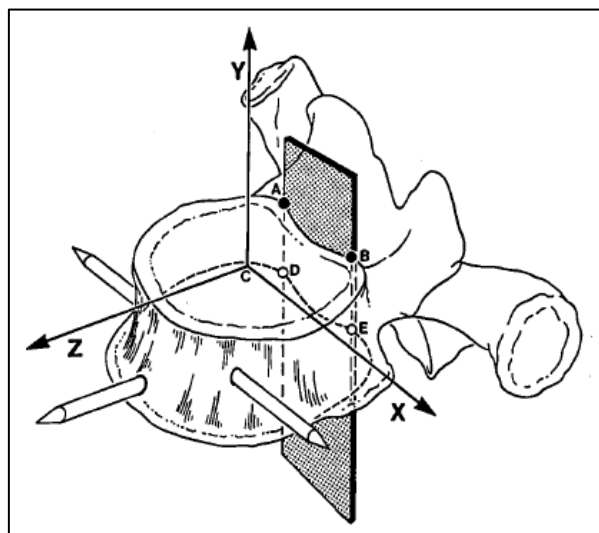


Figure 54: Panjabi Reference system.

Note: Point A, B, D, E: reference points that define the right superior, left superior, right inferior and left inferior edges of the posterior wall of the vertebral body. The best fit-plane passing through these points is the frontal plane. C is the centroid of the superior end-plate and the origin of the local coordinate system. The line perpendicular to the frontal plane formed to the z-axis. The line parallel to line AB and pointing to the left formed the x-axis. The y-axis is defined as the line perpendicular to the z-x plane [84].

After that, the lower endplate was resected flatly. Ten spherical and metallic markers (radius = 0.5 mm) have been positioned on the external surface of the clipped specimen and the specimen was CT-scanned, in order to obtain some reference points on the CT-images too.

3.2.2 Mechanical testing

The goal of the test machine was to approximate a uniformly distributed load, referring on the study of Jackman et al. [85]. Therefore, the hydrostatic pressure had to be imposed on a sufficiently large area compared to the physiologic loading one. This choice is the result of a previous research by the BIC laboratory team, that will be better exposed in section 3.3.2.

For this purpose, the set up in Figure 55 was used. Silicone supports have been used to reproduce the pulposus nucleus, in order to have a yielding material, able to distribute the pressure. To verify the assumption about the distributed pressure, a polyurethane specimen was realized and tested (section 3.5).



Figure 55: Experimental set up

3.2.3 Experimental data recordings

The response has been measured using digital image correlation (DIC) on the external cortex. Two cameras were used to record the displacements and the strains of ‘facets’, i.e. groups of pixels containing characteristic points. For the displacements, square facets of $360\ \mu\text{m} \times 360\ \mu\text{m}$ area were used. Finally, the strain data were calculated on

larger square patches, whose exact dimensions were 11 facets x 11 facets. The dimensions of the strain patches were determined by a noise analyses without any loads. The area has been increased until an acceptable condition was met, i.e. to have a noise at zero strain that was lower than 200 μ strain. In summary, a 4 mm x 4 mm area was set for the strain facets. In terms of comparisons with the FE models: the displacements can be compared node-wise, as the DIC grid is finer than the FE grid; the comparison of the deformations should instead be done by averaging FE strains on patches of 4 mm x 4 mm, to match the DIC patches which are much coarser than the FE element faces.

3.3 Boundary conditions of the model

In order to reproduce the experimental set, we set the boundary conditions. First, we registered the reference system of the model on that of the experimental set up, in order to compare the results obtained from experimental tests with those obtained by the FE simulation in the same reference system. Then, we implemented the loading conditions and the constraints. Finally, the model was solved in ANSYS Mechanical APDL. The simulation was performed in one step.

3.3.1 Registration of the experimental and model reference systems

The first attempt was the identification of the DIC reference system. For this purpose, we started from a first recording of the displacements, carried out on the anterior wall of the L5 vertebra without any load. The points cloud, got from the recording, has been imported in the free software Meshlab, for computing the normals for the points set and for reconstructing the surface by the Ball Pivot Algorithm (BPA). Given a point cloud with normals, the BPA reconstructs a surface, starting with a seed triangle and pivoting a ball around an edge until it touches another point, forming another

triangle. The process continues until all reachable edges have been tried and then starts from another seed triangle, until all points have been considered [86]. Subsequently, we imported the DIC surface on the software Albamaster; so this surface was in the DIC reference system. The DIC surface has been registered on a isosurface of the clipped vertebra, on which landmarks corresponding to the metallic markers had previously been placed. Therefore, we took advantage also of the coordinates of the markers to align the digitized points to the isosurface. For this purpose, the iterative closest point (ICP) algorithm was used. Finally, we moved the two adjacent surfaces back on the origin of the DIC system, resulting in the isosurface and DIC surface, together with the CDB files obtained from Bonemat (section 3.1.7), in the same experimental coordinate system. The registration process is summarised in Figure 56.

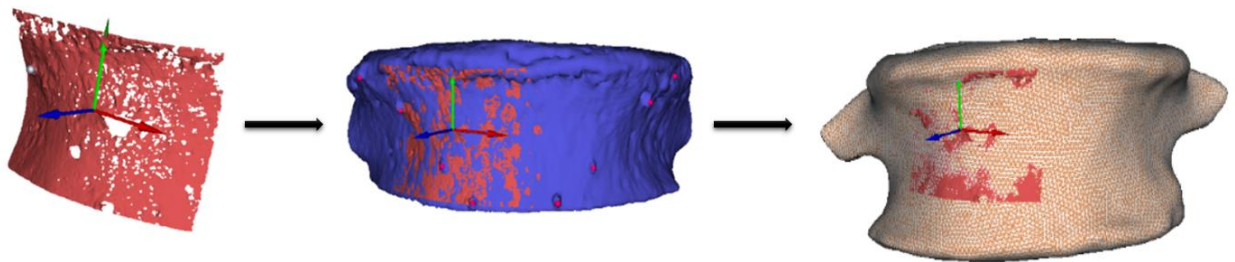


Figure 56: Steps of registration of the DIC and model reference system

3.3.2 Loading and constraint conditions

In order to replicate the clipping of the lower endplate of the vertebra, performed for the experimental tests, we reproduced the cutting plane and constrained all the nodes under this plane in all directions.

As far as loading conditions are concerned, our intent was to reproduce the loading conditions, described by Jackman et al. [85]. This study demonstrated that the intervertebral discs have great influence on the loads distributions on the endplate,

which results in a considerably high displacement of the endplate in the central area and a gradual decrease in intensity approaching the edges of the endplate, as shown in Figure 57.

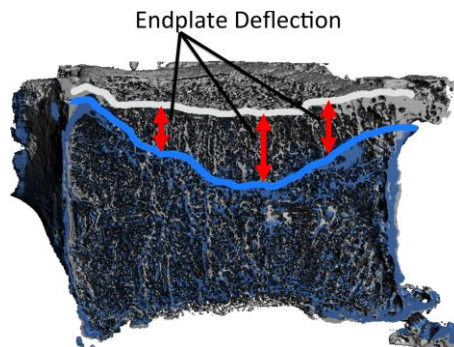


Figure 57: Deflection of the upper endplate. Sagittal half-section of vertebra before loading (gray) and after failure (blue) [85].

A previous study conducted by the group [75], preliminary conducted on computational models, has shown that applying a distributed pressure results in the deflection of the endplate, similarly to what shown by Jackman et al. Therefore, we chose as a simple and reasonable loading solution the application of a hydrostatic pressure on the upper endplate, perpendicular oriented to the faces of the superficial mesh elements, as previously done also in another previous work of the BIC group [75]. The pressure value has been calculated starting from a physiological value of force, according to other studies. The area of the loading surface has been calculated by Ansys, in order to have the same extension both in the simulation and in the experimental tests. The resultant modelled conditions, in the same reference system of the experimental tests, are shown in Figure 58.

In the first part of the modelling procedure, and also for the preliminary trials in the mechanical tests, a force value about two times the body weight of the donor, i.e. 917 N, was chosen (section 3.4). Then, the maxima loading values was changed to 2000 N for the experimental tests and for the CBM-model solving. This is the max vertical load that can be expected from calculations of musculoskeletal models on the lumbar spine. In particular, this is the load to which the lumbar spine is subjected during the

execution of an intense (such as lifting a full box) but not extreme motor task (such as impacts, falls etc.).

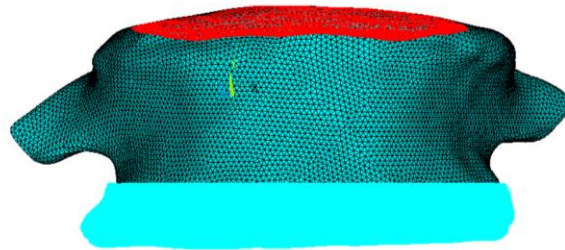


Figure 58: Constraint and loading conditions

3.4 Comparison between CBM-model and Shell-model

Next step was the comparison between the new conceived model, characterized by a patient-specific cortical compartment (CMB-model), and a previous model, conceived by the BIC group in a previous study (Shell-Model). The Shell-model included a uniform shell, characterized by thickness and Young modulus set to 0.4 mm and 10 GPa, respectively. The assignment of the material properties in the Shell-model has been carried out with the same procedure, used for the CBM-model, implementing the Morgan density-elasticity relationship [46] to obtain Young's modules. The 3D mesh of the Shell-model was generated starting from a 2D mesh with 1.5 mm triangular elements, too. However, the growth factor was set to 1. For both the models, the same boundary conditions have been implemented. A hydrostatic pressure has been applied on the upper endplate and the lower endplate has been constrained in all directions, to mimic the clipping of the vertebra of the experimental set up. The pressure value has been calculated as the ratio between the force value and the loading surface area. The force value was chosen by the LTM group during the first trials and it was about two times the body weight of the donor, i.e. 917 N. The area of the loading region on the upper endplate, calculated in Ansys, was around 990 mm².

The aim of the comparison was to evaluate the influence of the patient-specific cortical compartment, rather than a shell with constant properties, on the vertebral

mechanical properties. For this purpose, some significant parameters were analysed, starting from the results of the nodal or element solution:

- *Y- component of displacement*: displacements of the elements along the Y axis of the chosen reference system, resulting from the application of the hydrostatic pressure;
- *Y-component of elastic strain*;
- *Third principal elastic strain*;
- *Hoop strains distribution*;
- *Vertebral body stiffness*: ratio between the resultant force reaction along the Y axis (F_y) and the absolute value of the averaged displacement of the loading surface nodes on the upper endplate ($U_{Y,avg}$), extracted from the reaction and nodal solutions respectively:

$$Stiffness = \frac{F_y [N]}{U_{Y,avg} [mm]}$$

- *Percentage volume deformed more than 1000 μ strain*: we selected the elements more deformed than # μ strain and then we calculated the sum of the volume of these elements in order to obtain the percentage volume on the total one, except the constrained one.

Starting from these observations, we carried out an evaluation of the contribution of the cortical bone on the mechanical behaviour of the vertebra. For this purpose, we solved the CBM-model and the Shell-model, only including the cortical compartment and the shell respectively.

On the other hand, we also analysed other trends to understand the role of the vertebral cortical bone:

- *Thickness distribution in the cortical compartment:* the thickness data were extracted from the Stradview BIN file, that contains the values for each point where the density estimation was carried out. These data have been distributed in classes and then a bar diagram of the centres of the classes versus the percentage of points, included in each class, was realized;
- *Frequency distribution of the Young modulus (E) of the elements in the cortical compartment:* starting from the E values and the volume values of the elements of the cortical compartment, we first chose an optimal number of classes by which to divide the E values and then we got the volume of elements included in a certain class. After that, we calculated the percentage volume of each class on the total one, except the constrained part, finally getting the bar chart of the central values of each class compared to the percentage volume occupied by each class;

3.5 Polyurethane model

The starting idea was to homogeneously load the structure, in order to reproduce the condition described by Jackman et al. [85], by a constant pressure on the upper surface of the vertebra. A first evident problem is that vertebrae are bulky, with a height much less than their width. After checking that the experimental set up worked well on repeated tests, the LTM laboratory team chose to verify that the load was actually uniform. For this purpose, they decided to build a replica in homogeneous material to verify that the applied pressure was actually homogeneously distributed on the specimen-basis (the distal clipping plane just above the distal endplate). To carry out these tests, square-based pressure sensors, which fit the basis of the vertebra, were arranged on the platen of the testing machine. It was expected that, by loading the structure homogeneously, the pressure would also be homogeneous on the base. Therefore, starting from the shape of the upper endplate of the L5 vertebra, a solid

rigid polyurethane foam (30 PCF – Test material product by SAWBONES) prism was built. This material does not mimic the human bone structure but it is a good alternative test medium for the trabecular bone, because of its consistent properties. It is also characterized by uniformity, so that it is suitable for our purposes.

On the other hand, we decided to create a finite elements model of this polyurethane specimen to verify that our boundary conditions were adequate for validation. If the validation of this model is successful, we choose correct boundary conditions, i.e. the load and constraint conditions. Starting from these considerations, if the validation of the vertebra model is unsuccessful, we could expect that other variables of construction of the model are not adequate, rather than the boundary conditions. The polyurethane replica was recovered of barium sulphate and CT-scanned. Then, we extracted an isosurface from the images and clipped it planar.

Next step was the generation of the 2D and 3D meshes, with element size set to 1.5 mm and growth factor set to 1.2. Finally, we assigned the element type SOLID 187 and the material properties suggested by the producers.

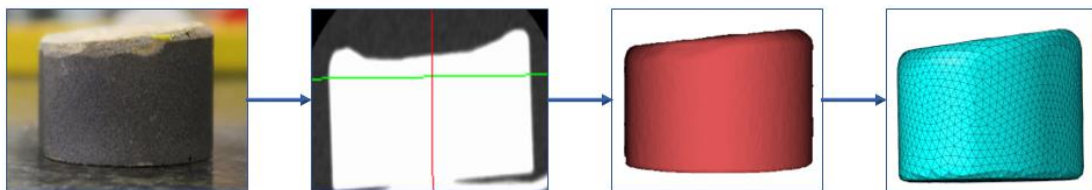


Figure 59: Construction of the polyurethane model

All the nodes on the basis of the model were constrained in all directions. We applied again a hydrostatic pressure. The force value was the maximum one used in the experimental test too, i.e. 500 N. This value derives from an inverse calculation, to obtain more or less the same deformations as on the vertebra. Therefore, the load is scaled by a factor equal to the ratio between the average elastic modulus of the vertebra and the known one of the PU. The loading surface area was selected on the

upper part of the model, starting from the experimental one. The model was solved in Ansys Mechanical APDL. The loading conditions are showed in Figure 60.

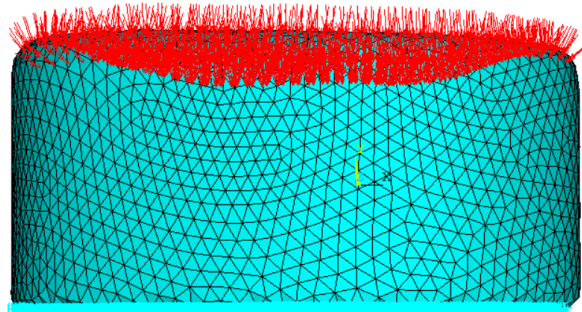


Figure 60: Polyurethane model – loading conditions

4 Results and discussion

In order to define the aims, I analysed the current state of art literature, looking for the most critical variables for realizing a vertebral model. One of the most debated issue is the modelling of the vertebral cortical compartment. Therefore, we constructed a model with a subject-specific cortical layer, obtained by Stradview software, through the Cortical Bone Mapping algorithm, which allows to obtain the estimation of the cortical bone density and then its thickness. Other modelling variable were analysed previously by the BIC laboratory team and were implemented in the CBM-model too, in order to compare it with the ‘Shell-model’, previously conceived with a uniform and a priori defined properties to mimick the cortical compartment. The aim was to assess the influence of the patient-specific cortical layer on the prediction of stiffness, stress and strains. Then, we verified the accuracy in the identification of boundary conditions, constructing a polyurethane replica. Then we compared the results of the modelled replica with the experimental ones. Lastly, we carried out a first validation process, comparing the results of the mechanical tests with the simulations results. In this chapter, all the results are reported.

4.1 Comparison of the CBM-Model with the Shell-Model

In absence of experimental data, the first attempt was to compare the models to assess the role of the subject-specific cortical compartment, rather than a shell with constant properties, on the vertebral mechanical properties. For this purpose, we extracted the outputs summarized in section 3.4.

We first observed the Y-component of the displacement. The comparison shows that the Y-displacement values are similar. Maxima CBM and shell displacements (SMN) results differ only from the fifth significant figure, i.e. in terms of nanometres, and can thus be considered equal. In the front area of the vertebra, the nodes of the Shell-model are slightly more displaced than those of the CBM model; however, the result is reversed in the posterior area of the vertebra. The displacements along the Y axis are shown in Figure 61.

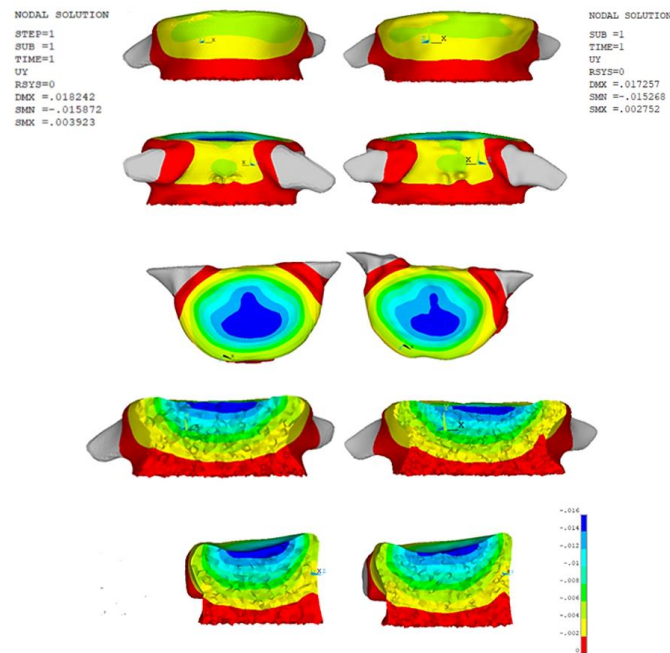


Figure 61: Y displacement [mm]. Left: Shell-model, Right: CBM-model. First row: Front view. Second row: Back view. Third row: Upper view. Fourth row: Sectioned on the frontal plane. Fifth row: Sectioned on the sagittal plane.

Comparing the elastic strain along the Y-axis, the third principal elastic strain and the hoop strain, we observed again no relevant differences, as shown in Figure 62, Figure 63 and Figure 64.

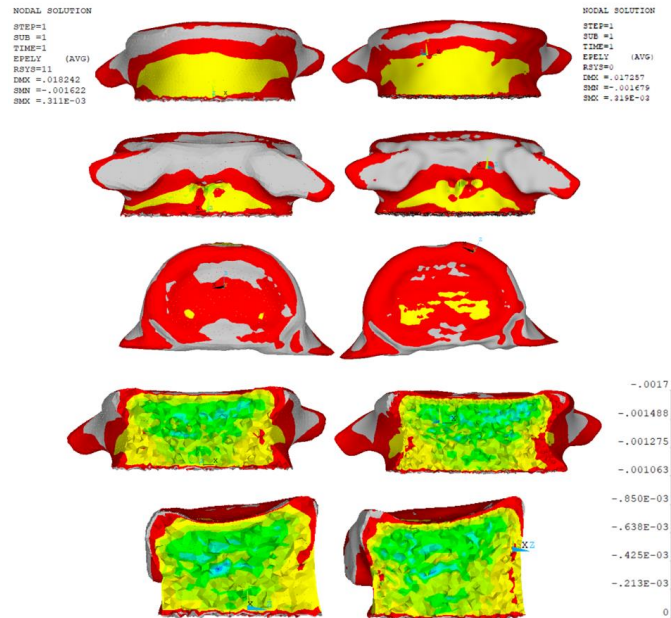


Figure 62: Elastic strain along Y axis [$\times 10^6 \mu\text{strain}$]. Left: Shell-model, Right: CBM-model. First row: Front view. Second row: Back view. Third row: Upper view. Fourth row: Sectioned on the frontal plane. Fifth row: Sectioned on the sagittal plane.

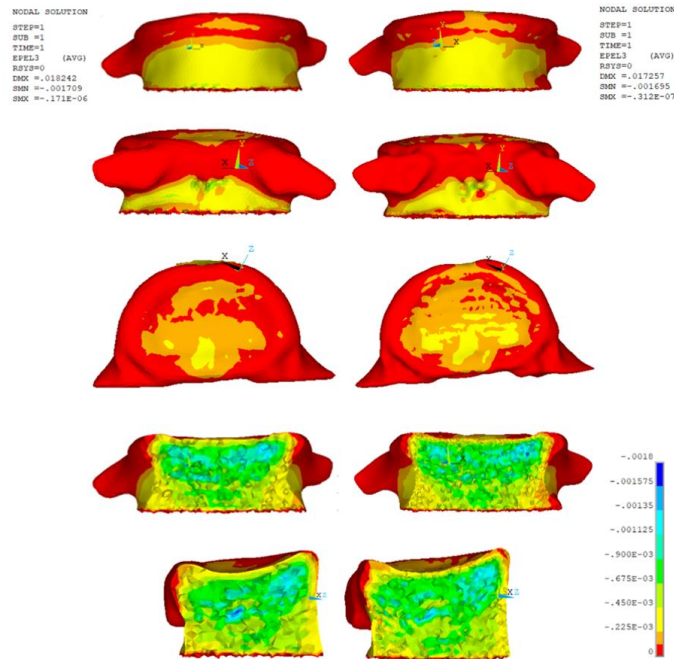


Figure 63: Third principal elastic strain [$\times 10^6 \mu\text{strain}$]. Left: Shell-model, Right: CBM-model. First row: Front view. Second row: Back view. Third row: Upper view. Fourth row: Sectioned on the frontal plane. Fifth row: Sectioned on the sagittal plane.

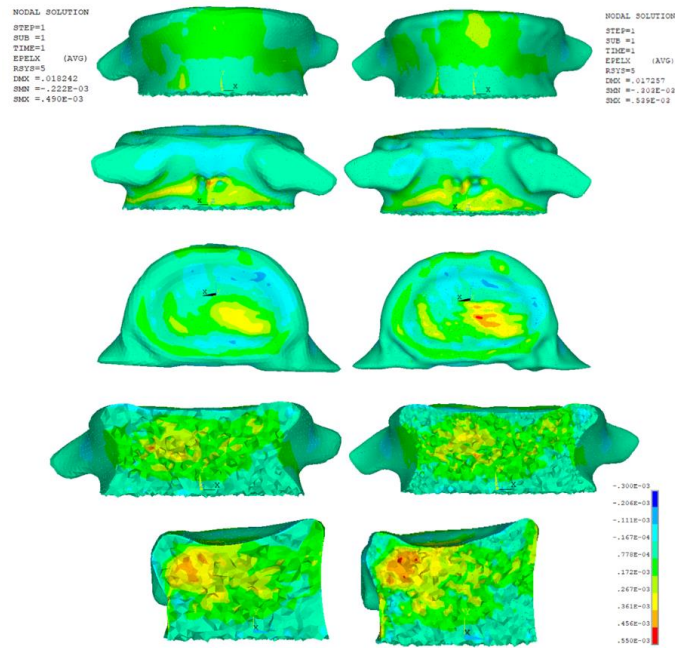


Figure 64: Hoop strain [$\times 10^6 \mu\text{strain}$]. Left: Shell-model, Right: CBM-model. First row: Front view. Second row: Back view. Third row: Upper view. Fourth row: Sectioned on the frontal plane. Fifth row: Sectioned on the sagittal plane.

Actually, differences in the stiffness values were limited to around 3%. In Table 7, the results are reported:

	F_y [N]	$ U_{y,avg} $ [mm]	Stiffness
Shell-model	892	0.0112	79536
CBM-model	891.11	0.0109	81899

Table 7: Stiffness results of the CBM-modell and the Shell-model

The results of the percentage volume deformed more than $1000 \mu\text{strain}$ are shown in Table 8:

	Volume of the elements deformed more than 1000 μ strain [mm ³]	Total volume [mm ³]	% volume deformed more than 1000 μ strain
Shell-model	1399,09	35794	3.91 %
CBM-model	1504,74	32373,9	4.65%

Table 8: % volume deformed more than 1000 μ strain

Starting from these results, we also compared the CBM-model and the Shell-model, including only the cortical layer and the uniform shell, again applying a hydrostatic pressure on the upper endplate.

The Y-displacements are reported in Figure 65:.

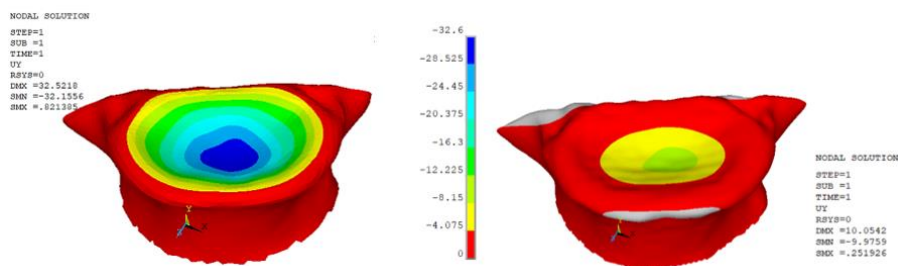


Figure 65: Y displacement [mm]. Left: Shell of the Shell-model, Right: Cortical compartment of the CBM-model.

The uniform and thin shell nodes are highly dislocated, compared to the cortical layer of the CBM-model. Analogously, the shell is much more deformed than the cortical compartment of the CBM-model (Figure 66).

It is clear that the subject-specific cortical layer is far stiffer than the shell. This is apparently contrasting with the results on the whole vertebra, where the CBM and the shell model showed almost identical results. However, the main differences in the cortical-only models were observed in the superior endplate, while the surrounding cortical walls differed less. This result points quite clearly to a significant role of the trabecular bone in the distribution of a uniform pressure over the endplate. We thus envisage that in case of a lytic lesion within the vertebral body, which would bring to

a lack of trabecular bone support, the CBM and shell model of the actual condition would differ substantially. In that case, a subject specific estimate of the cortical compartment could be necessary.

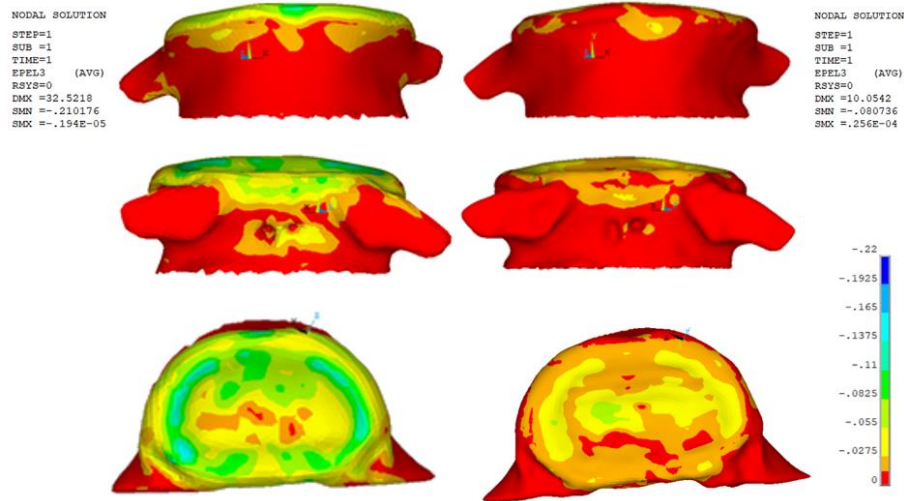


Figure 66: Third principal elastic strain [$\times 10^6 \mu\text{strain}$]. Left: Shell of the Shell-model, Right: Cortical compartment of the CBM-model. First row: Front view. Second row: Back view. Third row: Upper view.

To better understand the structural differences between the shell and the CBM model we also analysed the frequency distribution of the Young's modulus (E) of the elements and thickness distribution in the cortical compartment.

- *Young's modulus distribution*

The bar diagram and the coloured map represent the most significant classes, i.e. the fuller ones. The labels on the x-axis of the diagram and the values in the legend of the coloured map represent the centres of the classes. Each class is 1000 MPa large. The results are reported below (Figure 67 and Figure 68).

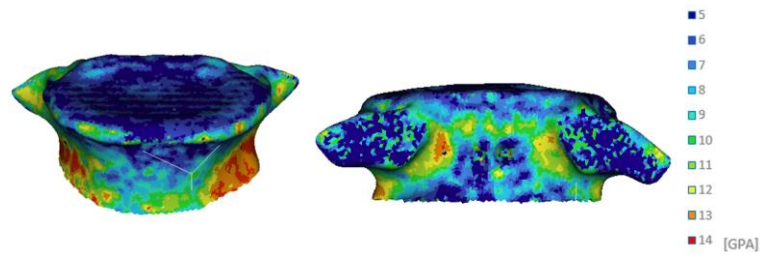


Figure 67: Frequency distribution of the Young modulus in the cortical compartment of the CBM-model – Coloured map.

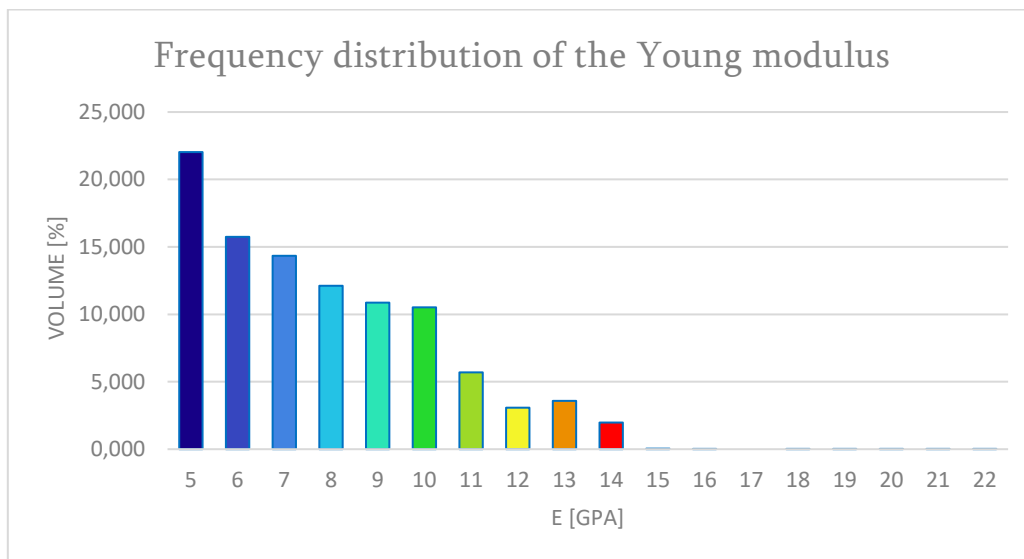


Figure 68: Frequency distribution of the Young modulus in the cortical compartment of the CMB-model – Bar diagram

The averaged Young's modulus (E) is 7785 MPa.

- *Thickness distribution*

The bar diagram and the coloured map (Figure 69 and Figure 70) represent the fuller classes. On the x-axis of the diagram and in the legend of the coloured map, the centres of the classes are indicated. Each class is 0.4 mm large.

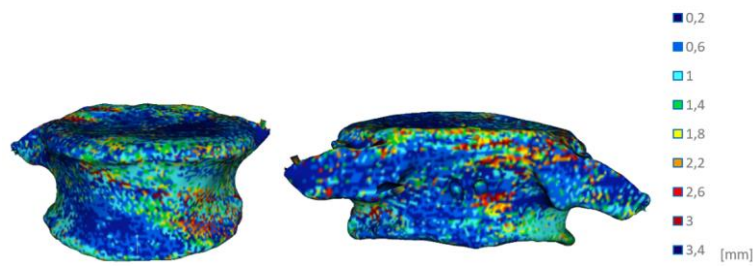


Figure 69: Thickness distribution in the cortical compartment of the CBM-model – Colored map

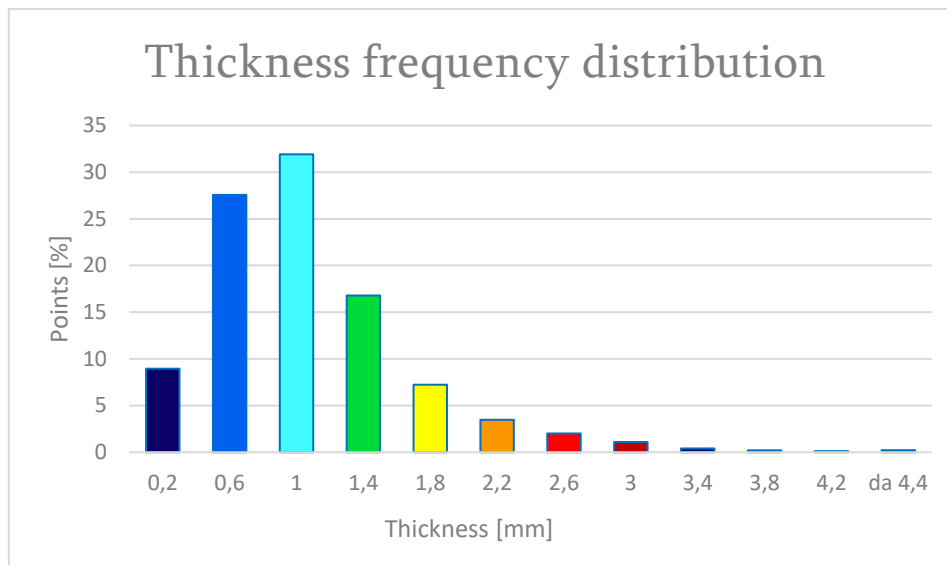


Figure 70: Thickness distribution in the cortical compartment of the CBM-model – bar diagram

The thickness of the cortical compartment of the CBM-model is overall higher than the shell one. Therefore, the results between the two models are similar because on one hand the thin and uniform shell protects the core of the vertebra, on the other hand the cortical layer of the CBM model, which has greater thickness and lower density, is involved by a greater load.

The validation of the model can help to better understand what happens locally.

4.2 CBM-model and Polyurethane model: FE analysis results

In this section, I report the results of the numeric simulations, conducted on both the CBM-model and Polyurethane model (PU-model). In particular, the aim was to show

the differences of the two model because of their different material properties. In both the simulations, we implemented the maximum load, i.e. 500 N and 2000 N respectively.

- **Polyurethane model**

The following figures (Figure 71 and Figure 72) show the Y-component of the displacement and of the strain.

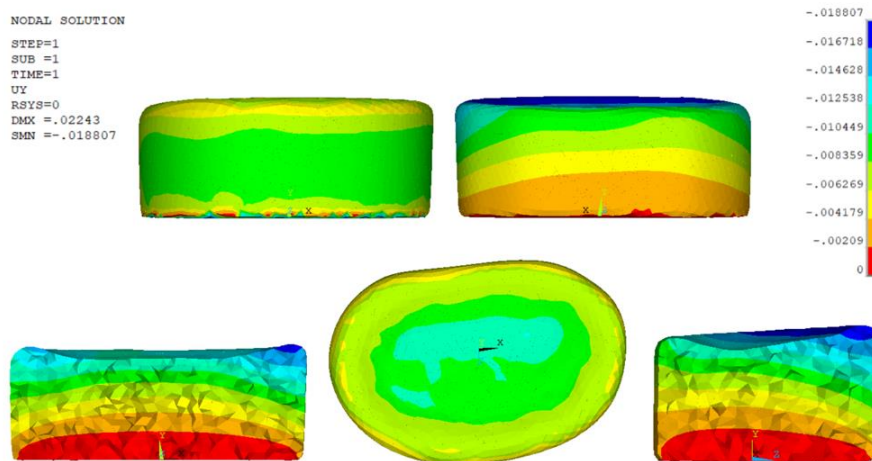


Figure 71: Y displacement [mm]. PU-model. First row: Front view - Back view. Second row: Sectioned on the frontal plane, upper view, Sectioned on the sagittal plane.

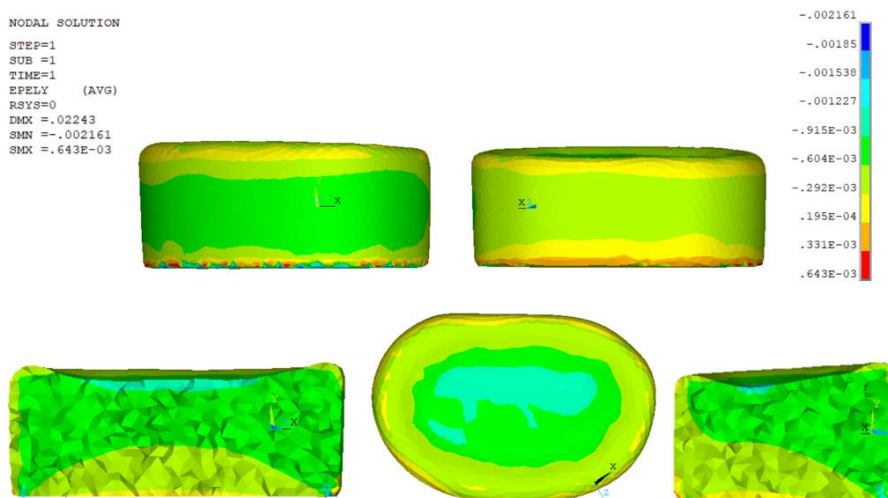


Figure 72: Y strain [$\times 10^6 \mu\text{strain}$]. PU-model. First row: Front view - Back view. Second row: Sectioned on the frontal plane, upper view, Sectioned on the sagittal plane.

- CBM-model

In figure, displacements and strains along y-axis are shown.

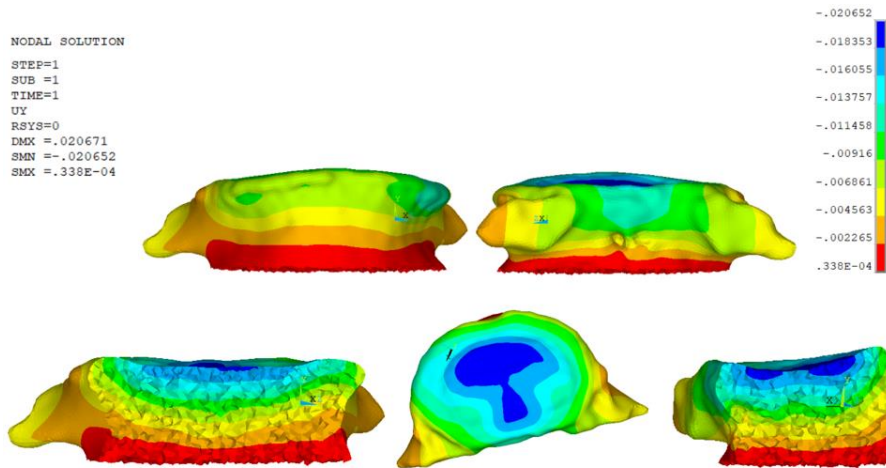


Figure 73: Y displacement [mm]. CBM-model. First row: Front view - Back view. Second row: Sectioned on the frontal plane, upper view, Sectioned on the sagittal plane.

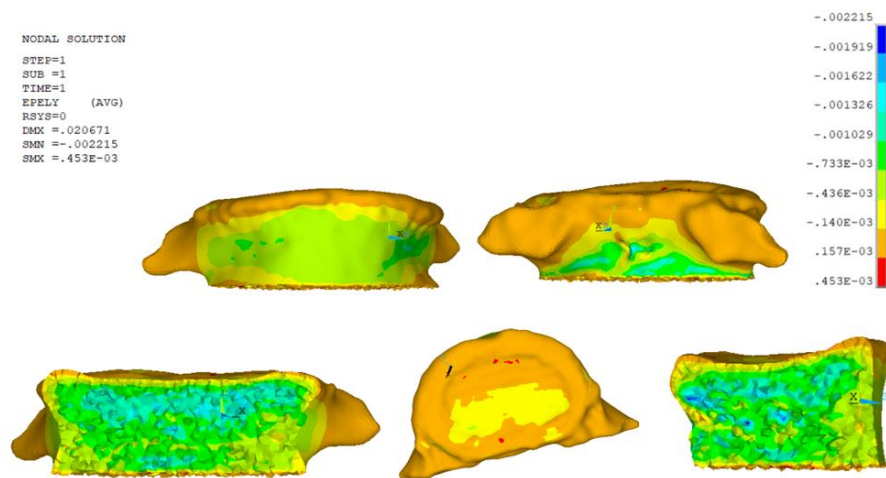


Figure 74 Y strain [$\times 10^6 \mu\text{strain}$]. CBM-model. First row: Front view - Back view. Second row: Sectioned on the frontal plane, upper view, Sectioned on the sagittal plane.

Starting from these results, we observed that both the models reflect our expectations. Indeed, their mechanical behaviour is congruent with the physics of the faced problem. In particular, the predicted displacements along the Y axis are linear and the predicted Y-strains with the polyurethane model are uniform. This is in agreement with the expected prevalence of normal stress due to the small antero-posterior wedge angle and the latero-lateral symmetry, and with the homogeneity of the material. The results of the CBM-model were less smooth, although showing clear linear (for the displacements) and constant (for strain) trends. We attribute the discrepancies with the PU model mostly to the inhomogeneity of the material properties, both of the trabecular compartment, which determines load transfer, and of the cortical one, which directly influence surface strain calculations. To support these observations, I report, as example, the results of the simulations on an anterior-left patch on the modelled vertebra (Figure 79, Figure 80, Figure 81, Figure 82) and on the modelled PU replica (Figure 75, Figure 76, Figure 77, Figure 78). In particular, the selected area reproduced one portion of the vertebra's cortical wall, on which DIC measurements are available.

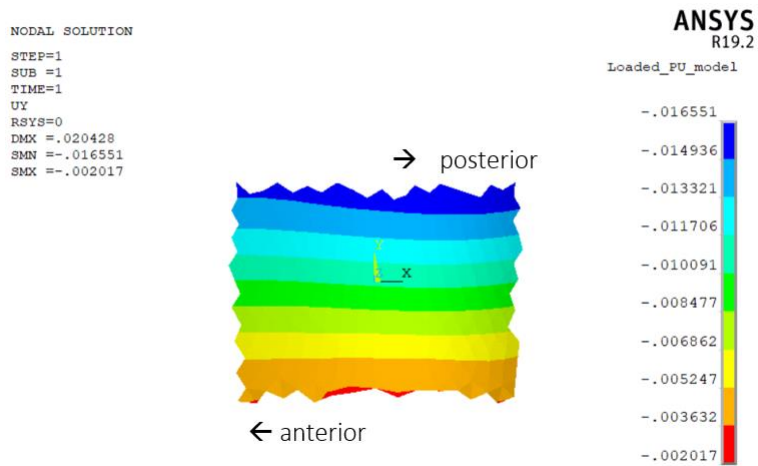


Figure 75: Y-displacement of the Anterior left-patch on the wall of the PU-model [mm].

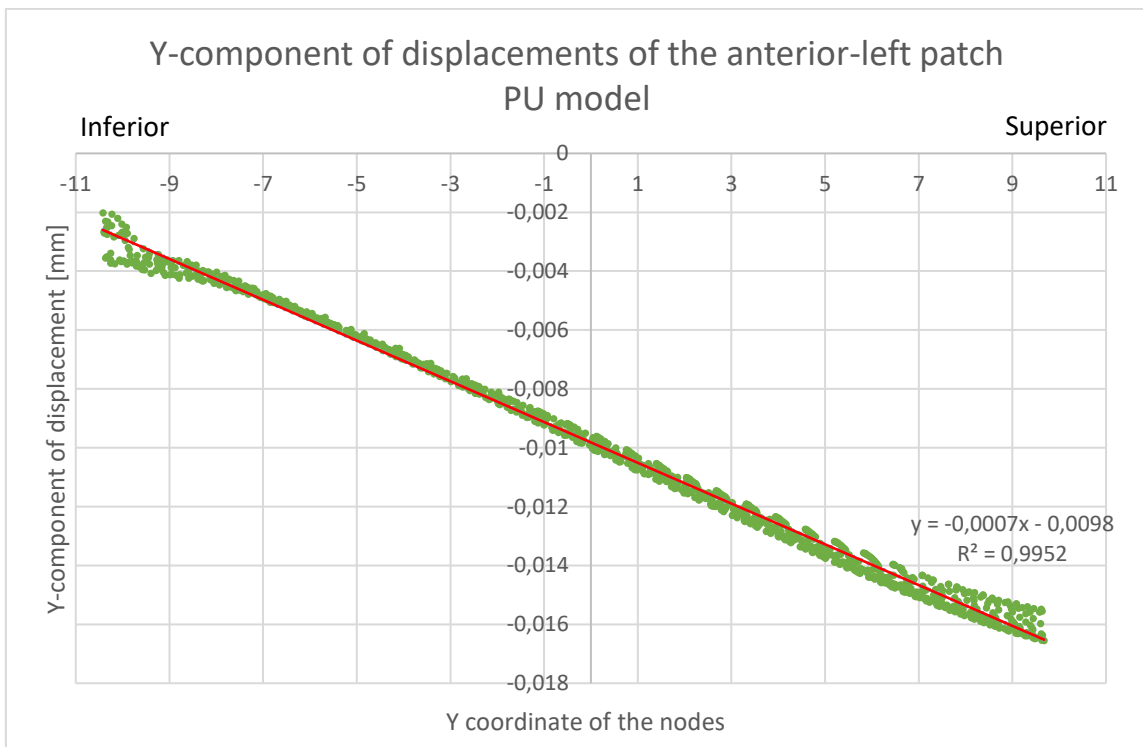


Figure 76: Scatter chart of the Y-displacement of the anterior left-patch on the wall of the PU model

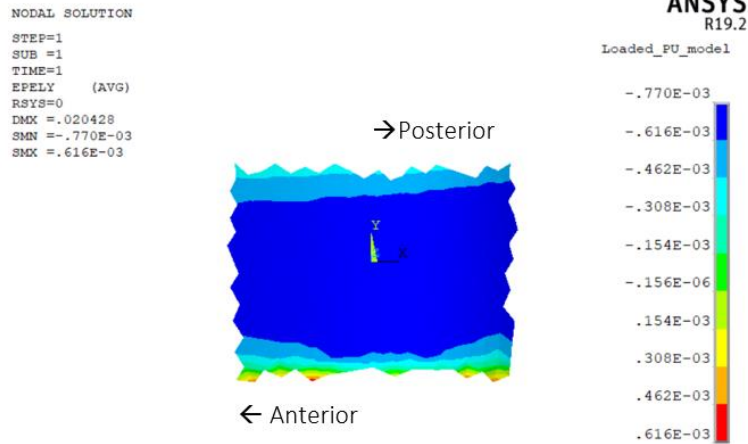


Figure 77: Y-elastic strain of the Anterior left-patch on the wall of the PU-model [$\times 10^6 \mu\text{strain}$]

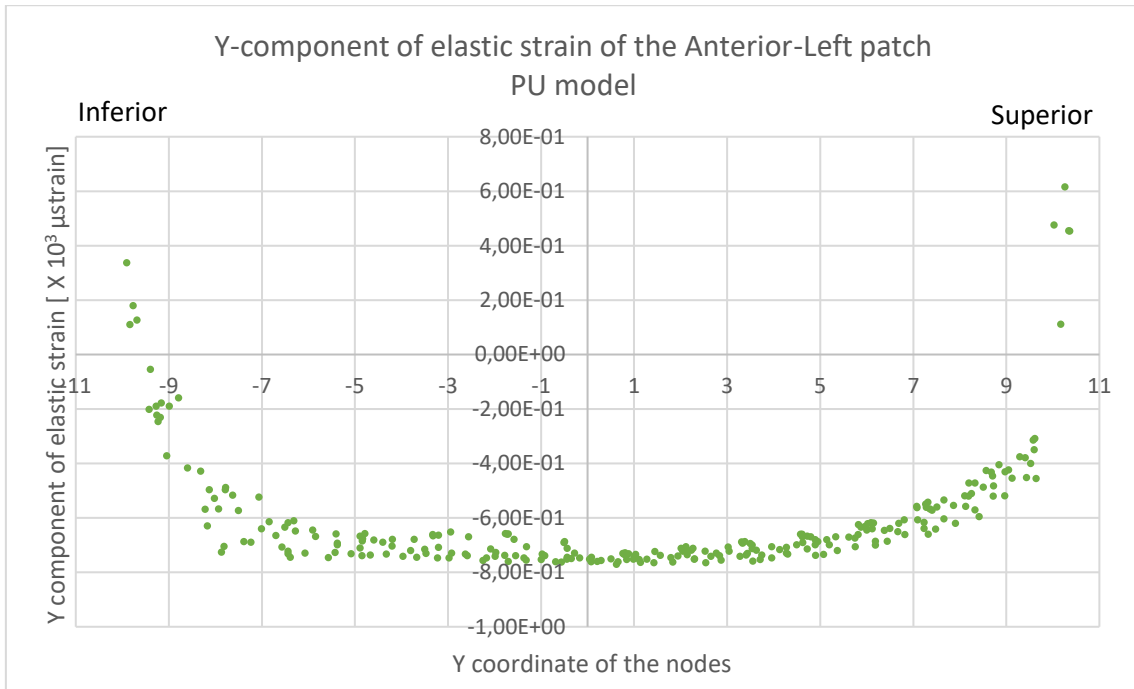


Figure 78: Scatter chart of the Y-elastic strain of the Anterior left-patch on the wall of the PU model

We observed an end effect at the upper extreme value of the Y coordinate. Excluding the value of Y-displacement associated to the Y coordinates adjacent to the upper endplate and to the constraint zone, the strain is constant. Indeed, the average strain in the range between -5 and 5 on the x-axis of the chart is $-721 \mu\text{strain}$ and the standard deviation is $31 \mu\text{strain}$.

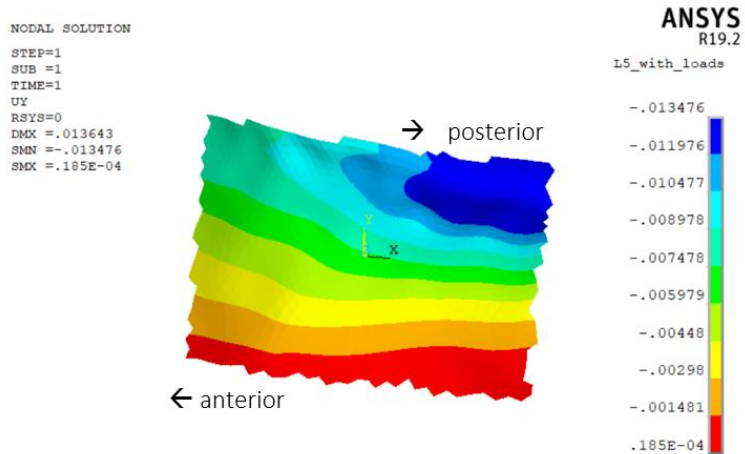


Figure 79: Y-displacement of the Anterior left-patch on the wall of the CBM-model [mm].

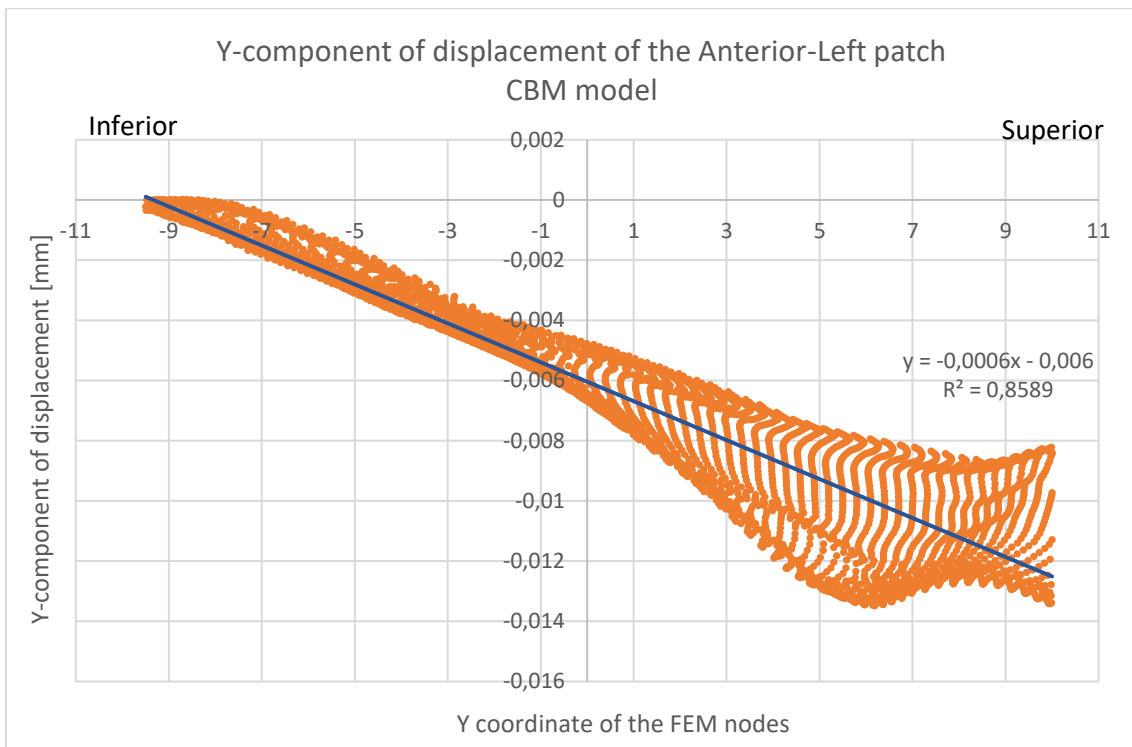


Figure 80: Scatter chart of the Y-displacement of the anterior left-patch on the wall of the CBM-model.

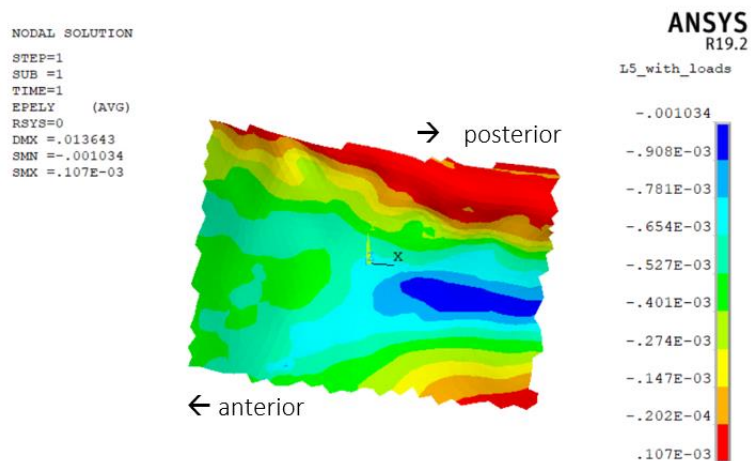


Figure 81: Y-elastic strain of the Anterior left-patch on the wall of the CBM-model [$\times 10^6 \mu\text{strain}$]

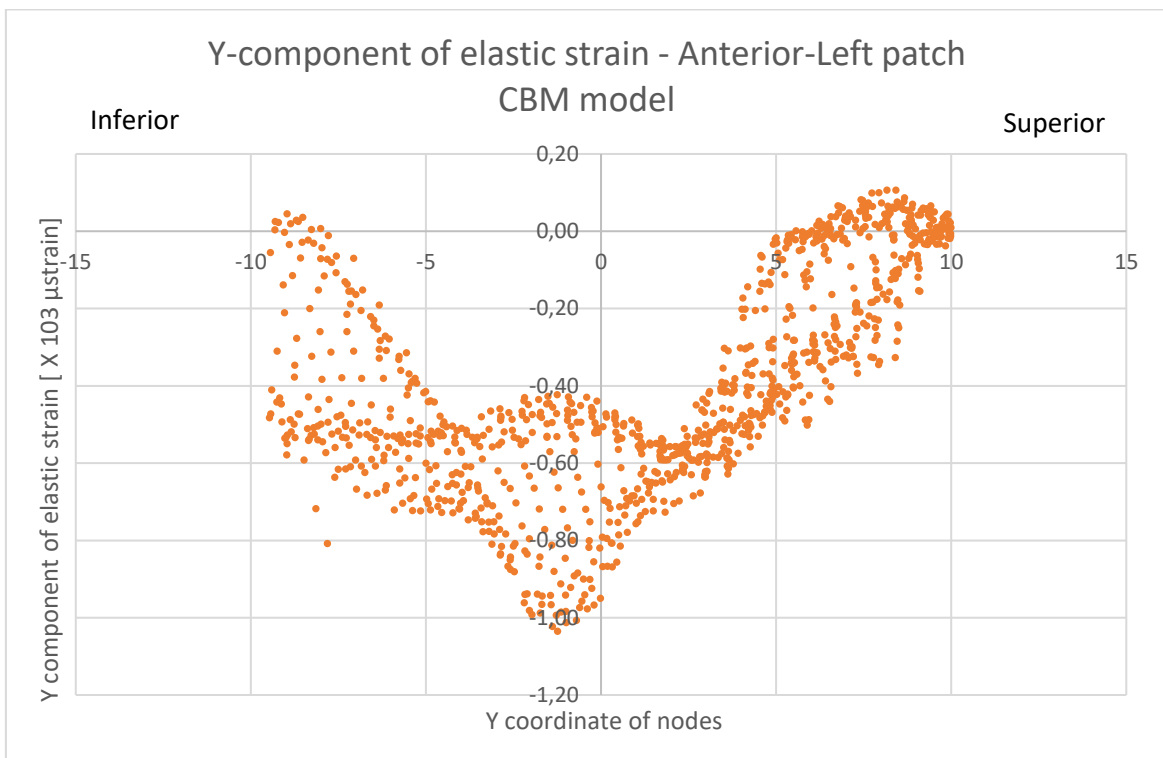


Figure 82: : Scatter chart of the Y-elastic strain of the Anterior left-patch on the wall of the CBM-model

4.3 DIC data analysis

Next step was the analysis of the experimental recordings. First, we observed that

at the constraint coordinate, i.e. where the vertebra and the polyurethane replica are embedded, there is a non-zero displacement. The dynamic range of the three component of displacement, i.e. the x, y and z components of displacement, was not much different. This was not in our expectations given the loading conditions applied during the mechanical tests. Indeed, we observed that the order of magnitude of the 3 displacement components did not vary as much as expected. For this reason, we plotted the Y displacement data in a scatter chart and we extracted the trend line. We noticed a recurrent offset, as shown as example in Figure 83, both in the recordings obtained on the vertebra and the polyurethane replica.

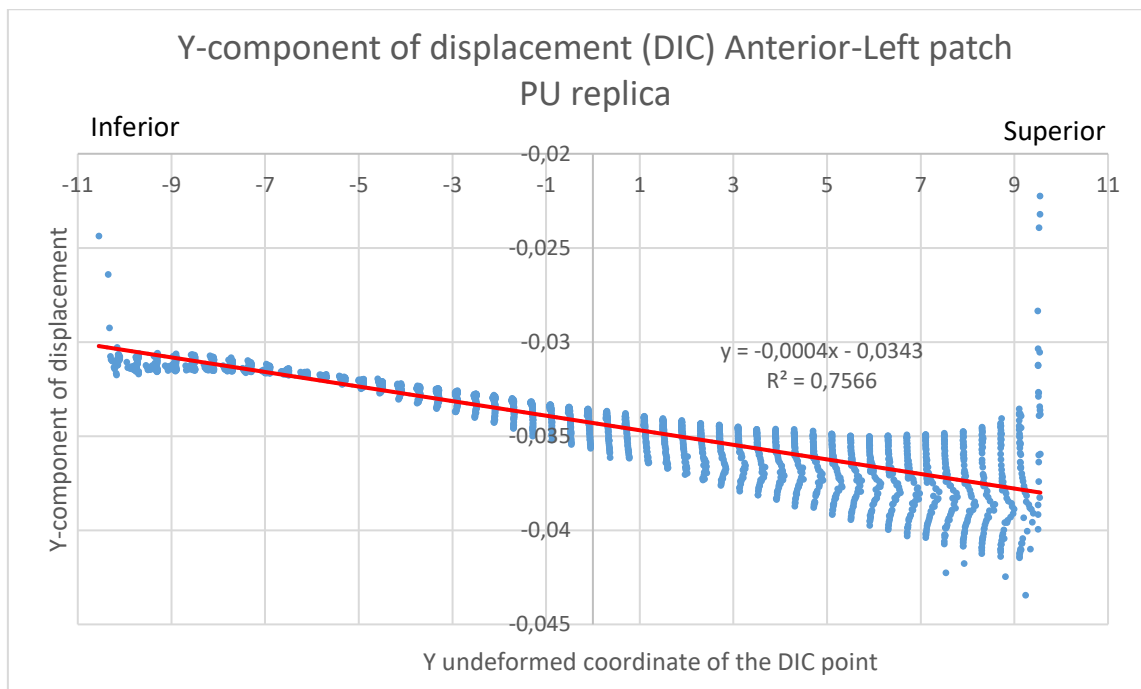


Figure 83: PU replica - Y axis: Y component of displacement, X axis: coordinates of the DIC points.

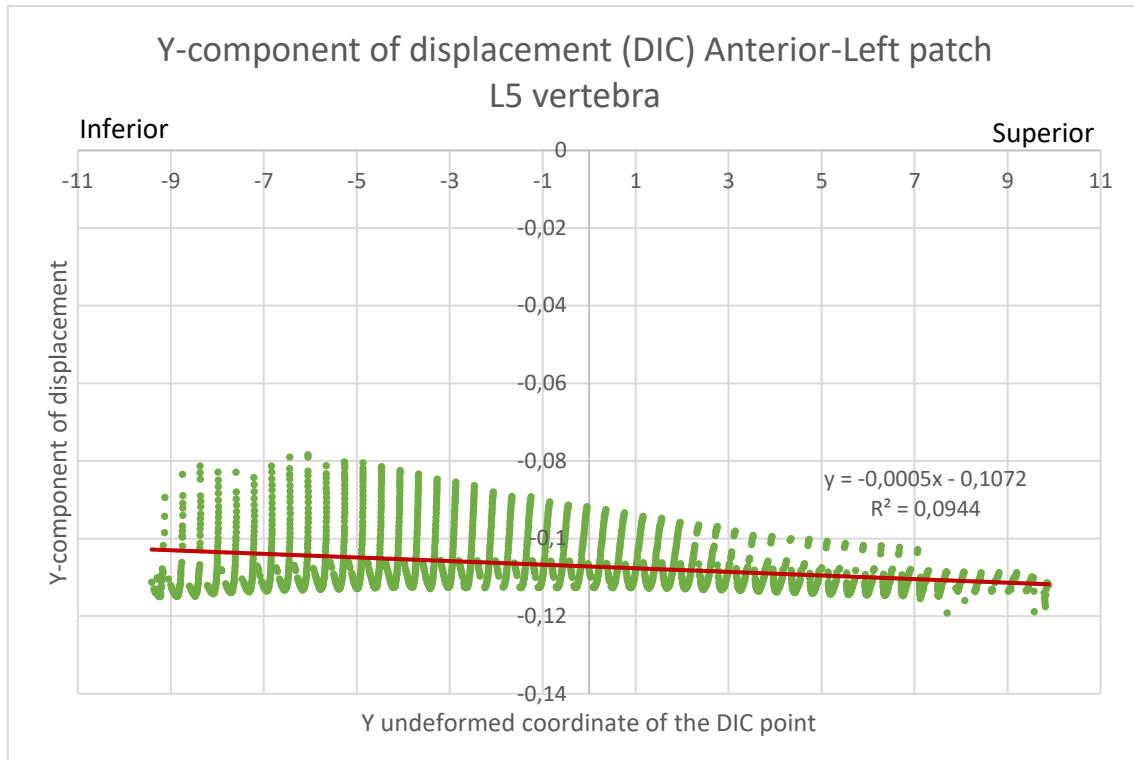


Figure 84: L5 vertebra - Y axis: Y component of displacement, X axis: coordinates of the DIC points.

The offset value was around 30 μm and 110 μm for the polyurethane replica and for the clipped vertebra respectively. However, subtracting the offset, the tendency of the displacements is almost linear.

Then, we decided to plot the Y component of elastic strain too, because it should not be affected by the offset, as it is the derivative of the displacement. The plot of the data of the same repetition and of the same patch shown in Figure 83 and Figure 84 is represented in Figure 85 and Figure 86 (below).

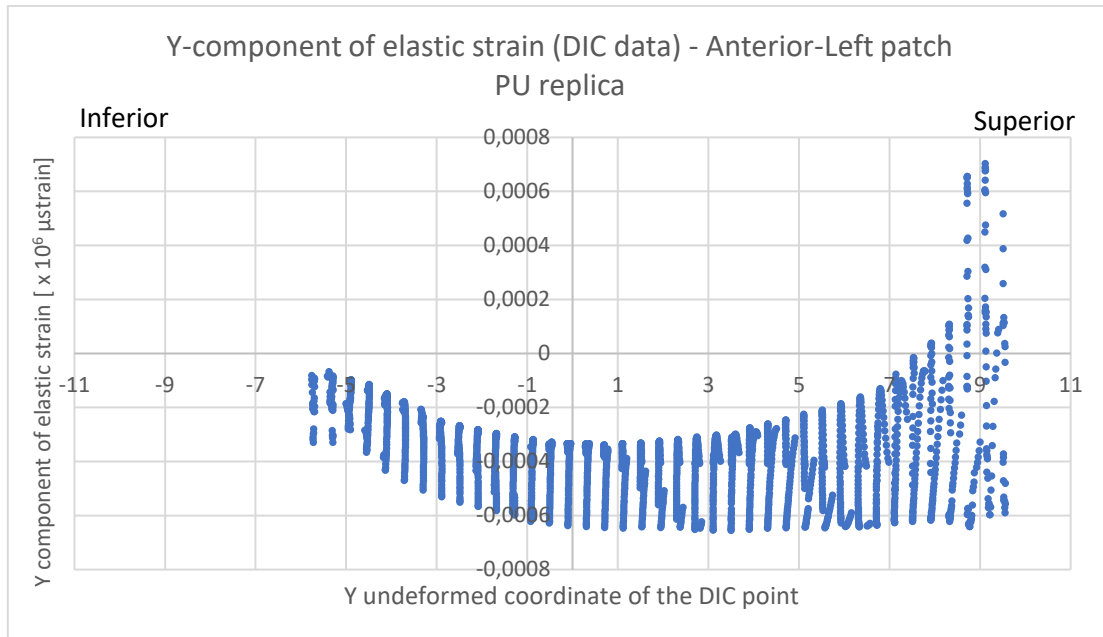


Figure 85: Scatter chart of the Y-elastic strain of the Anterior left-patch (DIC data) on the wall of the PU replica.

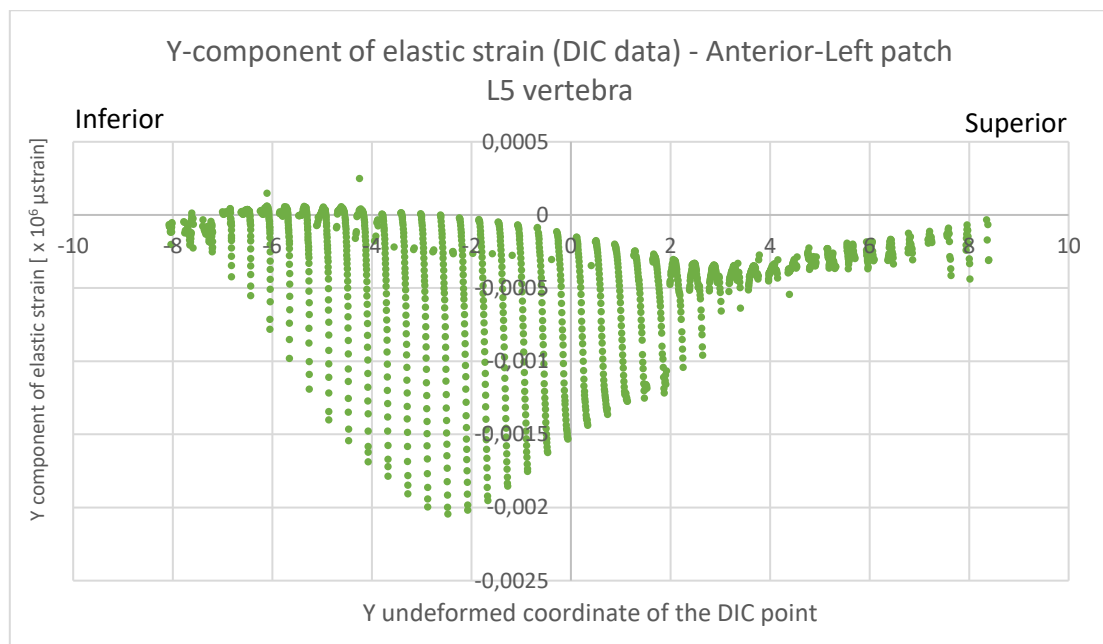


Figure 86: Scatter chart of the Y-elastic strain of the Anterior left-patch (DIC data) on the wall of the L5 vertebra

In the polyurethane replica data of Y-elastic strain (Figure 85), we noticed that there were some board end-artefacts. However, in the central portion of the PU sample, from -5 to 5 on the x-axis of the chart in Figure 85, the Y-strain is quite constant, as expected, although there is a large scatter. The averaged value of Y component of the strain in the considered range is $-420 \mu\text{strain}$ and the standard deviation is $110 \mu\text{strain}$.

In order to verify if the scatter amplitude was due to a trend of the strain along the x coordinate, i.e. the latero-lateral coordinate, we cut the extreme data. Starting from the data of the central portion of the sample, i.e. a portion of 8 mm, we plotted the strain along the y axis with respect to the x coordinate (Figure 87).

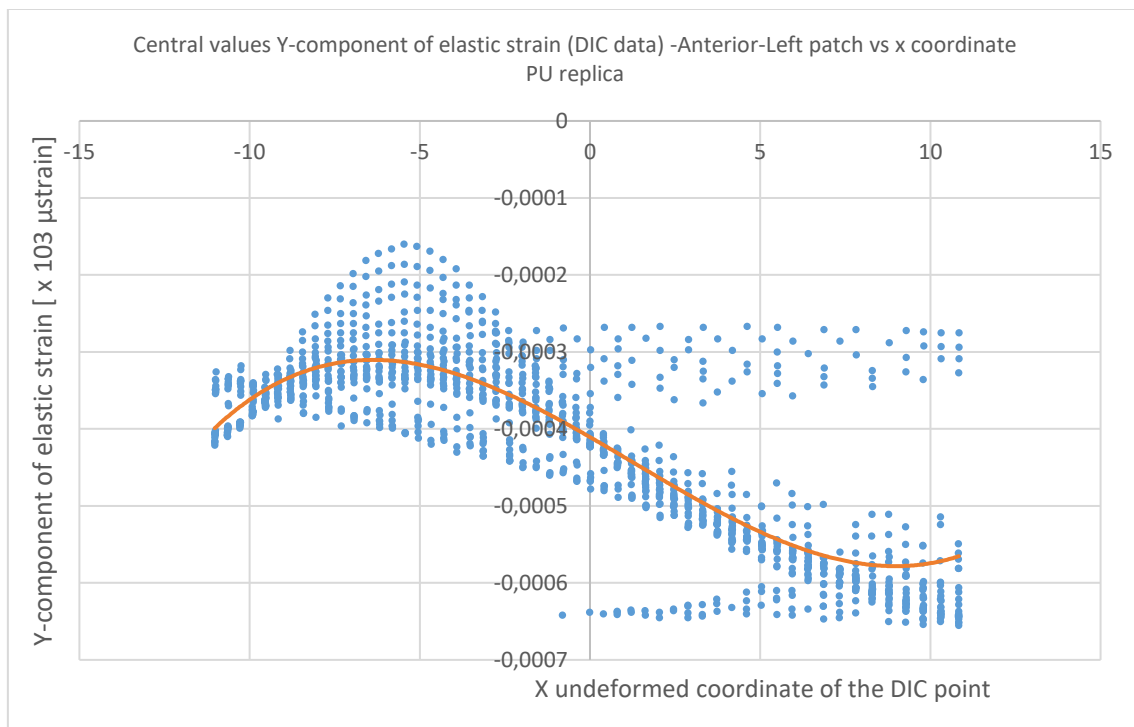


Figure 87: Scatter chart of the central values of Y-elastic strain of the Anterior left-patch (DIC data) on the wall of the PU replica vs X coordinate of the DIC point

Actually, excluding the outlier, there is a polynomial trend.

4.4 Check of the applied boundary conditions: preliminary validation of the PU model

Starting from the analysis of the DIC and FEM data, we decided to attempt a preliminary validation of the polyurethane model. For this purpose, we have subtracted the previously identified offset from all the data, in order to have zero displacement at the minimum y coordinate, where it is expected (Figure 88).

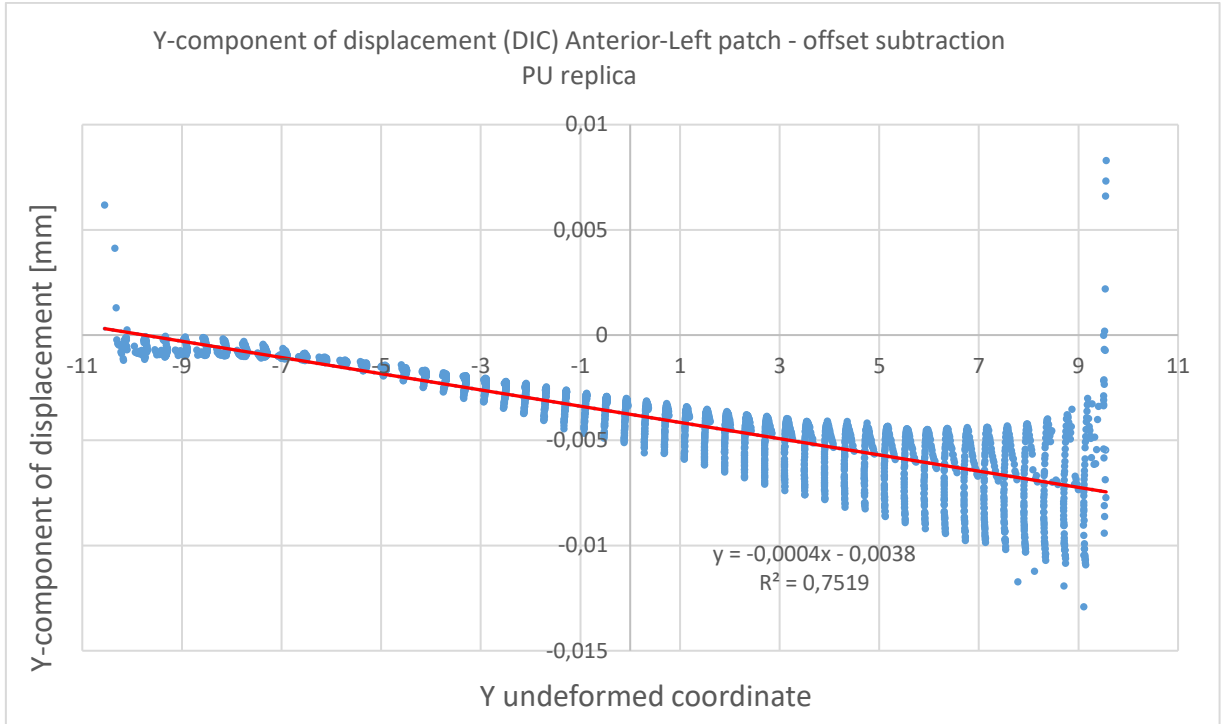


Figure 88: Scatter chart of Y-component of displacement of the Anterior left-patch (DIC data) on the wall of the PU replica after the subtraction of the founded offset.

After that, we imported the experimental data on Matlab®. We compared these values with the data obtained from the solving of the PU model, in order to assess their correlation. The result of the comparison is shown in Figure 89.

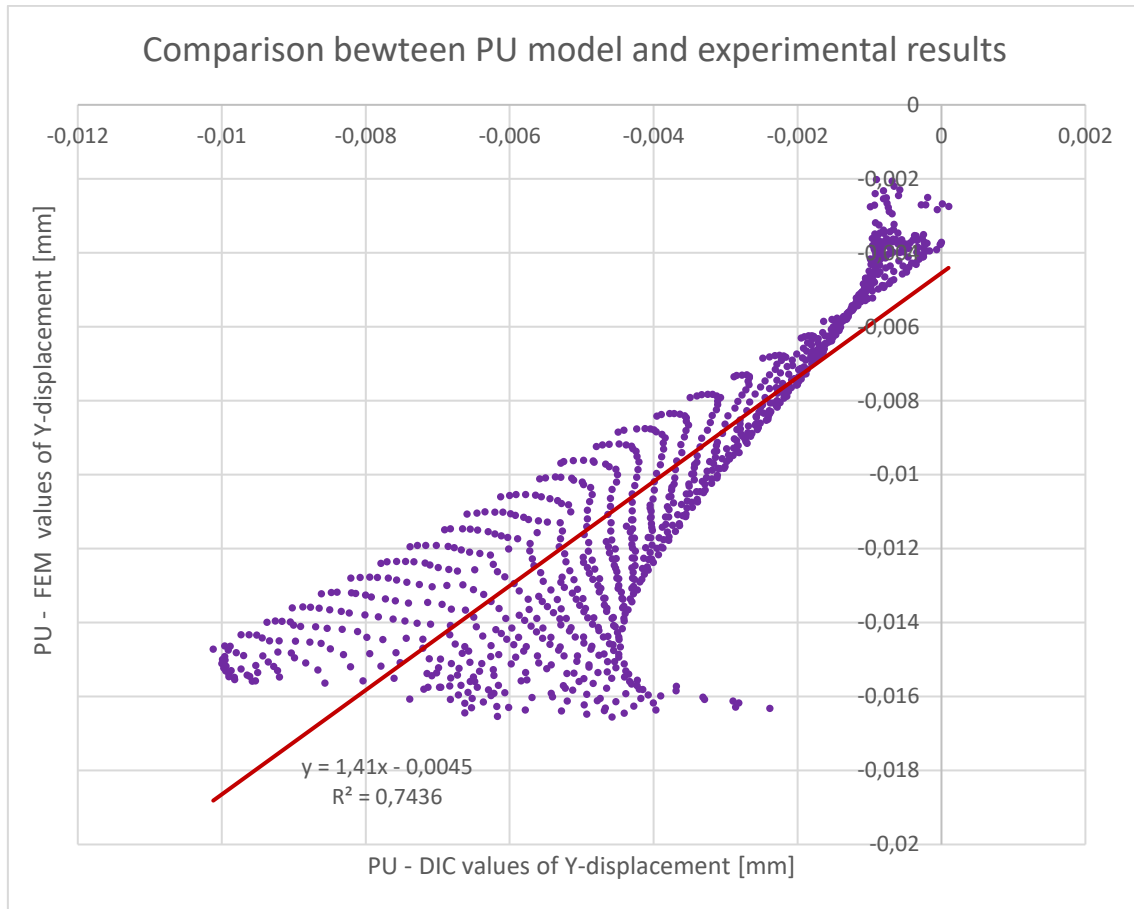


Figure 89: Comparison between Y component of displacements results of the PU model and experimental ones.

The coefficient of determination (R^2) is around 0.75, therefore there is a good correlation between the experimental data and the simulation ones.

It seems that the model has lower stiffness than the PU replica. Indeed, the higher FE values of Y-displacement are approximately double compared to the DIC values. This could be due the larger modelled loading surface, compared to the experimental one. An attempt could be to better modelling the loading surface, in order to deny or confirm this hypothesis. Anyway, the disposition of the data, like a 'fan', is due to the experimental scatter, that is higher near the higher displacement, i.e. near the upper endplate (higher Y-coordinates) and almost zero near the constrained zone. The deformations were instead compared in the range between -3 and 5 of the vertical coordinate (Y), calculating the mean value and the standard deviation. The results are

shown in the Table 9. The selected range was chosen because the strain values, provided by the DIC records, were almost constant.

	Mean value	Standard deviation
SSFE data	-725 μ strain	30 μ strain
DIC data	-420 μ strain	110 μ strain

Table 9: Y-Strain comparison between FE and DIC data

The mean value of the Y-strain, obtained from the numeric FE simulation, is also double compared to the DIC data recordings. This confirms the importance of the identification of the modelling variable to be corrected.

5 Conclusions and future attempts

This work was developed starting from the preliminary results about vertebral SSFE modelling already obtained at the BIC lab. The new defined aim was the exploration of a subject-specific modelling of cortical compartment, the development of the validation procedure to compare model results against experimental measurements on real vertebrae, checking also the correct identification of experimentally applied boundary conditions.

The exploration of a SSFE model of an L5 intact vertebra, with a patient-specific cortical layer (CBM-model) obtained from estimates of cortical bone thickness and density from clinical CT images, leads to the assessment of the influence of subject-specific cortical compartment on stiffness, strain and strength prediction. In absence of experimental data, the CBM-model was first compared with a literature-based model (Shell-model) that mimicked the cortical bone with a uniform shell. Results on the whole vertebra showed were almost identical. So that, we analysed only-cortical-models to better assess the role of the subject-specific cortical layer and the uniform shell. The patient-specific cortical layer is clearly stiffer than the shell and that seemed in contrast with the results obtained on the whole vertebra. However, the main differences are observed on the upper endplate, showing that the trabecular bone has a significant role in the distribution of the hydrostatic pressure on the endplate.

For this reason, despite the greater complexity of the CBM model compared to the Shell model, the modelling of a patient-specific cortex may be necessary when vertebral body is involved in a lytic metastasis, which would bring to a lack of trabecular bone integrity and support. Indeed, the patient-specific cortical compartment, which has greater thickness and lower density than the shell, seems to be involved in a greater load.

The second aim was to ensure an accurate model replication of the boundary conditions applied in the experimental tests, as the experimental setup is novel, so to

avoid bias in model validation, in particular to exclude the effect of vertebral bone inhomogeneity on the actual boundary conditions. For this purpose, a polyurethane replica of the L5 vertebra was built, mechanically tested and FE modelled (PU-model). Last aim was to compare SSFE computed displacements and strains, obtained both from the simulations on the CBM-model and the PU-model, with those measured on donor L5 vertebra by Digital Image Correlation (DIC) technique.

In order to get these aims, we analysed the SSFE results and the data of the DIC recordings. The FE analysis showed that both the models reflected our expectations. Indeed, the Y component of displacements has a linear trend and the Y elastic strains were constant, although the results of the CBM-model were less smooth. The diversification between the models has been mostly associated to the different material properties; indeed, the PU model includes a homogeneous material, while the CBM-model includes both the trabecular and the cortical compartments.

Then, we proceeded analysing the DIC data. First, we noticed an unexpected component of Y-displacement near the constrained zone, i.e. where both the vertebra and the polyurethane replica were embedded. Moreover, the dynamic range of the components of displacement, along the 3 axis of the DIC reference system, was quite similar. For these reasons, we plotted the Y-displacement data in a scatter chart, together with the Y-coordinates of the DIC points and we noticed a recurrent offset, both in the L5-vertebra data and in the polyurethane replica ones. In order to attempt a preliminary validation, we decided to subtract the value of the offset to the Y-displacement values and compare the resultant data with the FE ones for the PU model. The data showed a good correlation ($R^2=0.75$), despite the large scatter of the experimental data. However, the model is less stiff than the PU replica. Indeed, the maximum Y-displacement obtained through the simulation is about two times the experimental one. We also compare the Y-strain distribution in a selected range of the vertical coordinate. We founded that the model higher Y-strain value is twice the

experimental one. This result is compatible with the results obtained for the movements.

In conclusion, this work conducted to the realization of a model with a subject-specific cortical compartment, that can lead to a more custom prediction of strength, strain and stiffness, above all in presence of a metastatic lesion. Another achieved goal was the development of the whole validation procedure. Despite this, the whole validation process could not be carried out because of the dubious quality of the experimental data, in which we identified a large scatter and a recurring offset, that we supposed to be due to a superimposed noise or a non-subtracted rigid motion.

We communicated these observations to the laboratory which conducted the mechanical tests, so that we can solve the problem and proceed with new attempts.

An evident limitation of the work is the use of a single specimen in the lumbar region of the spine; it is certainly advisable to use a greater number of specimens to assess both the inter-subject variability and the position in the spine. This will be surely necessary in the next phase of the project.

References

- [1] F. Galbusera *et al.*, 'The Role of the Size and Location of the Tumors and of the Vertebral Anatomy in Determining the Structural Stability of the Metastatically Involved Spine: a Finite Element Study', *Transl. Oncol.*, vol. 11, no. 3, pp. 639–646, Jun. 2018, doi: 10.1016/j.tranon.2018.03.002.
- [2] C. G. Fisher *et al.*, 'A Novel Classification System for Spinal Instability in Neoplastic Disease', p. 9.
- [3] S. Y. Chang, J. H. Ha, S. G. Seo, B.-S. Chang, C.-K. Lee, and H. Kim, 'Prognosis of Single Spinal Metastatic Tumors: Predictive Value of the Spinal Instability Neoplastic Score System for Spinal Adverse Events', *Asian Spine J.*, p. 8.
- [4] G. Fraterrigo, 'Analysis of different subject-specific finite element modeling strategies to predict human vertebral strains, stiffness and strength to be used in clinical applications: the first step of a novel validation experiment'. Dec. 2019.
- [5] Drake, Richard L.; Vogl, Wayne; Tibbitts, Adam W.M. Mitchell; illustrations by Richard; Richardson, Paul, 'Gray's anatomy for students.', Philadelphia: Elsevier/Churchill Livingstone., 2005.
- [6] Gray, Henry, 'Gray's Anatomy.', 1977th ed., New York: Crown Publishers, Inc., p. 34.
- [7] Panjabi, M. M., & White, A. A., 'Basic Biomechanics of the Spine', in *Neurosurgery*, vol. 7, 1 vols, 1980, pp. 76–93.
- [8] F. H. Martini, M. J. Timmons, R. B. Tallitsch, e L. Cocco, 'Anatomia umana.', Napoli: SES, 2012.
- [9] V. Mahadevan, '«Anatomy of the vertebral column»', vol. 36, 7 vols, Surgery (Oxford), 2018, pp. 327–322.
- [10] R. Aquarius, J. Homminga, N. Verdonschot, and E. Tanck, 'The Fracture Risk of Adjacent Vertebrae Is Increased by the Changed Loading Direction After a Wedge Fracture', *Spine*, vol. 36, no. 6, pp. E408–E412, Mar. 2011, doi: 10.1097/BRS.0b013e3181f0f726.
- [11] S. E. Roth, P. Mousavi, J. Finkelstein, E. Chow, H. Kreder, and C. M. Whyne, 'Metastatic Burst Fracture Risk Prediction Using Biomechanically Based Equations', *Clin. Orthop.*, vol. 419, pp. 83–90, Feb. 2004, doi: 10.1097/00003086-200402000-00015.
- [12] M. Aebi, 'Classification of thoracolumbar fractures and dislocations', *Eur. Spine J.*, vol. 19, no. S1, pp. 2–7, Mar. 2010, doi: 10.1007/s00586-009-1114-6.
- [13] A. R. Vaccaro *et al.*, 'AOSpine Thoracolumbar Spine Injury Classification System: Fracture Description, Neurological Status, and Key Modifiers', *Spine*, vol. 38, no. 23, pp. 2028–2037, Nov. 2013, doi: 10.1097/BRS.0b013e3182a8a381.
- [14] E. A. Nicoll, *Fractures of the dorso-lumbar spine*, vol. 31, 3 vols. J Bone Joint Surg Am, 1949.
- [15] Holdsworth FW, 'Fractures, dislocation, and fracture dislocations of the spine.', Br, 1963.

- [16] Denis F., ‘The three column spine and its significance in the classification of acute thoracolumbar spinal injuries.’, in *Spine.*, vol. 8, 8 vols, Phila Pa 1976, 1983, pp. 817–831.
- [17] McAfee PC, Yuan HA, Fredrickson BE, Lubicky JP, ‘The value of computed tomography in thoracolumbar fractures. An analysis of one hundred consecutive cases and a new classification.’, *Am*, pp. 461–479, 1983.
- [18] F. MagerP, M. Aebi, S. D. Gertzbein, J. Harms, and S. Nazarian, ‘A comprehensive classification of thoracic and lumbar injuries’, p. 18.
- [19] Whitesides TE Jr, ‘Traumatic kyphosis of the thoracolumbar spine.’, *Clin Orthop.*, 1977, p. 128:78–92.
- [20] M. Mansoorinasab and H. Abdolhoseinpour, ‘A review and update of vertebral fractures due to metastatic tumors of various sites to the spine: Percutaneous vertebroplasty’, *Interv. Med. Appl. Sci.*, vol. 10, no. 1, pp. 1–6, Mar. 2018, doi: 10.1556/1646.10.2018.03.
- [21] M. Burke, M. Akens, A. Kiss, T. Willett, and C. Whyne, ‘Mechanical behavior of metastatic vertebrae are influenced by tissue architecture, mineral content, and organic feature alterations: METASTATIC TISSUE CHANGES IMPACT SPINE MECHANICS’, *J. Orthop. Res.*, Aug. 2018, doi: 10.1002/jor.24105.
- [22] C. M. Whyne, S. S. Hu, K. L. Workman, and J. C. Lotz, ‘Biphasic Material Properties of Lytic Bone Metastases’, *Ann. Biomed. Eng.*, vol. 28, no. 9, pp. 1154–1158, Sep. 2000, doi: 10.1114/1.1313773.
- [23] ‘Nonoperative management of femoral, humeral, and acetabular metastases in patients with breast carcinoma’, vol. 45, p. 5.
- [24] J. H. Keyak, I. Y. Lee, and H. B. Skinner, ‘Correlations between orthogonal mechanical properties and density of trabecular bone: Use of different densitometric measures’, *J. Biomed. Mater. Res.*, vol. 28, no. 11, pp. 1329–1336, Nov. 1994, doi: 10.1002/jbm.820281111.
- [25] M. J. Ciarelli, S. A. Goldstein, J. L. Kuhn, D. D. Cody, and M. B. Brown, ‘Evaluation of orthogonal mechanical properties and density of human trabecular bone from the major metaphyseal regions with materials testing and computed tomography’, *J. Orthop. Res.*, vol. 9, no. 5, pp. 674–682, Sep. 1991, doi: 10.1002/jor.1100090507.
- [26] Von Stechow, D., Nazarian, A., Zurakowski, D., Muller, R., Snyder, B.D., ‘METASTATIC CANCER BONE TISSUE BEHAVES MECHANICALLY AS A RIGID POROUS FOAM’, *Trans. Orthop. Res. Soc.* 28 995, p. 1, 2003.
- [27] J. A. Hipp, A. E. Rosenberg, and W. C. Hayes, ‘Mechanical properties of trabecular bone within and adjacent to osseous metastases’, *J. Bone Miner. Res.*, vol. 7, no. 10, pp. 1165–1171, Dec. 2009, doi: 10.1002/jbmr.5650071008.
- [28] T. S. Kaneko, J. S. Bell, M. R. Pejcic, J. Tehranzadeh, and J. H. Keyak, ‘Mechanical properties, density and quantitative CT scan data of trabecular bone with and without metastases’, *J. Biomech.*, vol. 37, no. 4, pp. 523–530, Apr. 2004, doi: 10.1016/j.jbiomech.2003.08.010.

- [29] J. Antoniou, L. M. Epure, A. J. Michalek, M. P. Grant, J. C. Iatridis, and F. Mwale, 'Analysis of quantitative magnetic resonance imaging and biomechanical parameters on human discs with different grades of degeneration: Quantitative MRI of Degenerated Human Discs', *J. Magn. Reson. Imaging*, vol. 38, no. 6, pp. 1402–1414, Dec. 2013, doi: 10.1002/jmri.24120.
- [30] A. M. Cheung *et al.*, 'High-Resolution Peripheral Quantitative Computed Tomography for the Assessment of Bone Strength and Structure: A Review by the Canadian Bone Strength Working Group', *Curr. Osteoporos. Rep.*, vol. 11, no. 2, pp. 136–146, Jun. 2013, doi: 10.1007/s11914-013-0140-9.
- [31] D. H. Pahr, E. Dall'Ara, P. Varga, and P. K. Zysset, 'HR-pQCT-based homogenised finite element models provide quantitative predictions of experimental vertebral body stiffness and strength with the same accuracy as μ FE models', *Comput. Methods Biomech. Biomed. Engin.*, vol. 15, no. 7, pp. 711–720, Jul. 2012, doi: 10.1080/10255842.2011.556627.
- [32] H. Li, H. Zhang, Z. Tang, and G. Hu, 'Micro-computed tomography for small animal imaging: Technological details', *Prog. Nat. Sci.*, vol. 18, no. 5, pp. 513–521, May 2008, doi: 10.1016/j.pnsc.2008.01.002.
- [33] A. J. Fields, S. K. Eswaran, M. G. Jekir, and T. M. Keaveny, 'Role of Trabecular Microarchitecture in Whole-Vertebral Body Biomechanical Behavior', *J. Bone Miner. Res.*, vol. 24, no. 9, pp. 1523–1530, Sep. 2009, doi: 10.1359/jbmr.090317.
- [34] G. Guglielmi, 'Quantitative Computed Tomography', *Semin. Musculoskelet. Radiol.*, vol. 6, no. 3, p. 10, 2002.
- [35] R. P. Crawford, C. E. Cann, and T. M. Keaveny, 'Finite element models predict in vitro vertebral body compressive strength better than quantitative computed tomography.', *Bone*, vol. 33, no. 4, pp. 744–750, Oct. 2003, doi: 10.1016/S8756-3282(03)00210-2.
- [36] K. Imai, I. Ohnishi, M. Bessho, and K. Nakamura, 'Nonlinear finite element model predicts vertebral bone strength and fracture site.', *Spine*, vol. 31, no. 16, pp. 1789–1794, Jul. 2006, doi: 10.1097/01.brs.0000225993.57349.df.
- [37] J. Choise, J. M. Valiadis, C. Travert, S. Kolta, C. Roux, and W. Skalli, 'Vertebral strength prediction under anterior compressive force using a finite element model for osteoporosis assessment', *Comput. Methods Biomech. Biomed. Engin.*, vol. 18, no. sup1, pp. 1900–1901, Oct. 2015, doi: 10.1080/10255842.2015.1069562.
- [38] J. M. Buckley, K. Loo, and J. Motherway, 'Comparison of quantitative computed tomography-based measures in predicting vertebral compressive strength.', *Bone*, vol. 40, no. 3, pp. 767–774, Mar. 2007, doi: 10.1016/j.bone.2006.10.025.
- [39] R. Zebaze and E. Seeman, 'Cortical Bone: A Challenging Geography: A CHALLENGING GEOGRAPHY', *J. Bone Miner. Res.*, vol. 30, no. 1, pp. 24–29, Jan. 2015, doi: 10.1002/jbmr.2419.

- [40] M. A. K. Liebschner, D. L. Kopperdahl, W. S. Rosenberg, and T. M. Keaveny, 'Finite Element Modeling of the Human Thoracolumbar Spine', *Spine*, vol. 28, no. 6, pp. 559–565, Mar. 2003, doi: 10.1097/01.BRS.0000049923.27694.47.
- [41] A. Maloul, J. Fialkov, and C. Whyne, 'The Impact of Voxel Size-Based Inaccuracies on the Mechanical Behavior of Thin Bone Structures', *Ann. Biomed. Eng.*, vol. 39, no. 3, pp. 1092–1100, Mar. 2011, doi: 10.1007/s10439-010-0215-z.
- [42] A. Zeinali, B. Hashemi, and S. Akhlaghpour, 'Noninvasive prediction of vertebral body compressive strength using nonlinear finite element method and an image based technique.', *Phys. Medica PM Int. J. Devoted Appl. Phys. Med. Biol. Off. J. Ital. Assoc. Biomed. Phys. AIFB*, vol. 26, no. 2, Apr. 2010, doi: 10.1016/j.ejmp.2009.08.002.
- [43] T. S. Keller, 'Predicting the compressive mechanical behavior of bone', *J. Biomech.*, vol. 27, no. 9, pp. 1159–1168, Sep. 1994, doi: 10.1016/0021-9290(94)90056-6.
- [44] D. L. Kopperdahl and T. M. Keaveny, 'Yield strain behavior of trabecular bone', *J. Biomech.*, vol. 31, no. 7, pp. 601–608, Jul. 1998, doi: 10.1016/S0021-9290(98)00057-8.
- [45] B. Helgason, E. Perilli, E. Schileo, F. Taddei, S. Brynjólfsson, and M. Viceconti, 'Mathematical relationships between bone density and mechanical properties: A literature review', *Clin. Biomech.*, vol. 23, no. 2, pp. 135–146, Feb. 2008, doi: 10.1016/j.clinbiomech.2007.08.024.
- [46] E. F. Morgan, H. H. Bayraktar, and T. M. Keaveny, 'Trabecular bone modulus–density relationships depend on anatomic site', *J. Biomech.*, vol. 36, no. 7, pp. 897–904, Jul. 2003, doi: 10.1016/S0021-9290(03)00071-X.
- [47] E. Schileo, J. Pitocchi, C. Falcinelli, and F. Taddei, 'Cortical bone mapping improves finite element strain prediction accuracy at the proximal femur', *Bone*, vol. 136, p. 115348, Jul. 2020, doi: 10.1016/j.bone.2020.115348.
- [48] D R Carter, W C Hayes, 'The Compressive Behavior of Bone as a Two-Phase Porous Structure', *J Bone Jt. Surg Am.*
- [49] S. Bernard, J. Schneider, P. Varga, P. Laugier, K. Raum, and Q. Grimal, 'Elasticity–density and viscoelasticity–density relationships at the tibia mid-diaphysis assessed from resonant ultrasound spectroscopy measurements', *Biomech. Model. Mechanobiol.*, vol. 15, no. 1, pp. 97–109, Feb. 2016, doi: 10.1007/s10237-015-0689-6.
- [50] J. C. Lotz, T. N. Gerhart, and W. C. Hayes, 'Mechanical properties of metaphyseal bone in the proximal femur', *J. Biomech.*, vol. 24, no. 5, pp. 317–329, Jan. 1991, doi: 10.1016/0021-9290(91)90350-V.
- [51] N. Brandolini, L. Cristofolini, and M. Viceconti, 'EXPERIMENTAL METHODS FOR THE BIOMECHANICAL INVESTIGATION OF THE HUMAN SPINE: A REVIEW', *J. Mech. Med. Biol.*, vol. 14, no. 01, p. 1430002, Feb. 2014, doi: 10.1142/S0219519414300026.

- [52] Y. Chevalier *et al.*, ‘A patient-specific finite element methodology to predict damage accumulation in vertebral bodies under axial compression, sagittal flexion and combined loads’, *Comput. Methods Biomech. Biomed. Engin.*, vol. 11, no. 5, pp. 477–487, Oct. 2008, doi: 10.1080/10255840802078022.
- [53] M. Zhang, J. Gao, X. Huang, H. Gong, M. Zhang, and B. Liu, ‘Effects of Scan Resolutions and Element Sizes on Bovine Vertebral Mechanical Parameters from Quantitative Computed Tomography-Based Finite Element Analysis’, *J. Healthc. Eng.*, vol. 2017, pp. 1–14, 2017, doi: 10.1155/2017/5707568.
- [54] M. Kinzl, U. Wolfram, and D. H. Pahr, ‘Identification of a crushable foam material model and application to strength and damage prediction of human femur and vertebral body.’, *J. Mech. Behav. Biomed. Mater.*, vol. 26, pp. 136–147, Oct. 2013, doi: 10.1016/j.jmbbm.2013.04.026.
- [55] E. Dall’Ara, D. Pahr, P. Varga, F. Kainberger, and P. Zysset, ‘QCT-based finite element models predict human vertebral strength in vitro significantly better than simulated DEXA.’, *Osteoporos. Int. J. Establ. Result Coop. Eur. Found. Osteoporos. Natl. Osteoporos. Found. USA*, vol. 23, no. 2, pp. 563–572, Feb. 2012, doi: 10.1007/s00198-011-1568-3.
- [56] L. Cristofolini, N. Brandolini, V. Danesi, M. M. Juszczuk, P. Erani, and M. Viceconti, ‘Strain distribution in the lumbar vertebrae under different loading configurations’, *Spine J.*, vol. 13, no. 10, pp. 1281–1292, Oct. 2013, doi: 10.1016/j.spinee.2013.06.014.
- [57] H. Ahn, P. Mousavi, S. Roth, D. Reidy, J. Finkelstein, and C. Whyne, ‘Stability of the Metastatic Spine Pre and Post Vertebroplasty’., *J. Spinal Disord. Tech.*, vol. 19, no. 3, pp. 178–182, May 2006, doi: 10.1097/01.bsd.0000172362.15103.e8.
- [58] J. M. Buckley, L. Cheng, K. Loo, C. Slyfield, and Z. Xu, ‘Quantitative Computed Tomography-Based Predictions of Vertebral Strength in Anterior Bending’., *Spine*, vol. 32, no. 9, pp. 1019–1027, Apr. 2007, doi: 10.1097/01.brs.0000260979.98101.9c.
- [59] M. Mirzaei, A. Zeinali, A. Razmjoo, and M. Nazemi, ‘On prediction of the strength levels and failure patterns of human vertebrae using quantitative computed tomography (QCT)-based finite element method’, *J. Biomech.*, vol. 42, no. 11, pp. 1584–1591, Aug. 2009, doi: 10.1016/j.jbiomech.2009.04.042.
- [60] G. Maquer, J. Schwiedrzik, and P. K. Zysset, ‘Embedding of human vertebral bodies leads to higher ultimate load and altered damage localisation under axial compression.’, *Comput. Methods Biomech. Biomed. Engin.*, vol. 17, no. 12, pp. 1311–1322, 2014, doi: 10.1080/10255842.2012.744400.
- [61] E. Dall’Ara *et al.*, ‘A nonlinear finite element model validation study based on a novel experimental technique for inducing anterior wedge-shape fractures in human vertebral bodies in vitro.’, *J. Biomech.*, vol. 43, no. 12, pp. 2374–2380, Aug. 2010, doi: 10.1016/j.jbiomech.2010.04.023.

- [62] X. G. Cheng *et al.*, 'Prediction of Vertebral Strength In Vitro by Spinal Bone Densitometry and Calcaneal Ultrasound', *J. Bone Miner. Res.*, vol. 12, no. 10, pp. 1721–1728, Oct. 1997, doi: 10.1359/jbmr.1997.12.10.1721.
- [63] Y. Chevalier, D. Pahr, and P. K. Zysset, 'The Role of Cortical Shell and Trabecular Fabric in Finite Element Analysis of the Human Vertebral Body', *J. Biomech. Eng.*, vol. 131, no. 11, p. 111003, 2009, doi: 10.1115/1.3212097.
- [64] M. A. Haidekker, R. Andresen, and H. J. Werner, 'Relationship Between Structural Parameters, Bone Mineral Density and Fracture Load in Lumbar Vertebrae, Based on High-Resolution Computed Tomography, Quantitative Computed Tomography and Compression Tests', *Osteoporos. Int.*, vol. 9, no. 5, pp. 433–440, Apr. 1999, doi: 10.1007/s001980050168.
- [65] D. Burklein *et al.*, 'Correlation of thoracic and lumbar vertebral failure loads with in situ vs. ex situ dual energy X-ray absorptiometry', *J. Biomech.*, vol. 35, pp. 579–587, 2001.
- [66] J.-P. Roux *et al.*, 'Contribution of Trabecular and Cortical Components to Biomechanical Behavior of Human Vertebrae: An Ex Vivo Study', *J. Bone Miner. Res.*, vol. 25, no. 2, pp. 356–361, Feb. 2010, doi: 10.1359/jbmr.090803.
- [67] E.-M. LOCHMULLER *et al.*, 'Mechanical Strength of the Thoracolumbar Spine in the Elderly: Prediction From In Situ Dual-energy X-ray Absorptiometry, Quantitative Computed Tomography (QCT), Upper and Lower Limb Peripheral QCT, and Quantitative Ultrasound', *Bone*, vol. 31, no. 1, pp. 77–84, 2002, doi: 10.1016/S8756-3282(02)00792-5.
- [68] A. J. Fields, G. L. Lee, X. S. Liu, M. G. Jekir, X. E. Guo, and T. M. Keaveny, 'Influence of vertical trabeculae on the compressive strength of the human vertebra', *J. Bone Miner. Res.*, vol. 26, no. 2, pp. 263–269, Feb. 2011, doi: 10.1002/jbmr.207.
- [69] R. Rotter *et al.*, 'Vertebral body stenting: a new method for vertebral augmentation versus kyphoplasty', *Eur. Spine J.*, vol. 19, no. 6, pp. 916–923, Jun. 2010, doi: 10.1007/s00586-010-1341-x.
- [70] C. M. Whyne, S. S. Hu, and J. C. Lotz, 'Burst Fracture in the Metastatically Involved Spine: Development, Validation, and Parametric Analysis of a Three-Dimensional Poroelastic Finite-Element Model', *Spine*, vol. 28, no. 7, pp. 652–660, Apr. 2003, doi: 10.1097/01.BRS.0000051910.97211.BA.
- [71] S. E. Roth, P. Mousavi, J. Finkelstein, E. Chow, H. Kreder, and C. M. Whyne, 'Metastatic Burst Fracture Risk Prediction Using Biomechanically Based Equations', *Clin. Orthop.*, vol. 419, pp. 83–90, Feb. 2004, doi: 10.1097/00003086-200402000-00015.
- [72] C. M. Whyne, S. S. Hu, and J. C. Lotz, 'Parametric finite element analysis of vertebral bodies affected by tumors', *J. Biomech.*, p. 8, 2001.
- [73] C. E. Tschirhart, A. Nagpurkar, and C. M. Whyne, 'Effects of tumor location, shape and surface serration on burst fracture risk in the metastatic spine', *J.*

- Biomech.*, vol. 37, no. 5, pp. 653–660, May 2004, doi: 10.1016/j.jbiomech.2003.09.027.
- [74] C. E. Tschirhart, J. A. Finkelstein, and C. M. Whyne, ‘Biomechanics of vertebral level, geometry, and transcortical tumors in the metastatic spine’, *J. Biomech.*, vol. 40, no. 1, pp. 46–54, Jan. 2007, doi: 10.1016/j.jbiomech.2005.11.014.
- [75] Pierpaolo Romano, ‘VALIDAZIONE DI MODELLI PERSONALIZZATI AD ELEMENTI FINITI PER LA PREDIZIONE DEL COMPORTAMENTO MECCANICO DI VERTEBRE UMANE: STUDIO PRELIMINARE PER L’OTTIMIZZAZIONE DEL DISEGNO NUMERICO-SPERIMENTALE.’, 2019 2018.
- [76] ‘Stradview web address’. <http://mi.eng.cam.ac.uk/~gmt11/stradview>.
- [77] R. T. Armstrong and B. Jp, ‘Acceptability of Cone Beam CT vs. Multi- Detector CT for 3D Anatomic Model Construction’, p. 1.
- [78] G. M. Treece, A. H. Gee, P. M. Mayhew, and K. E. S. Poole, ‘High resolution cortical bone thickness measurement from clinical CT data’, *Med. Image Anal.*, vol. 14, no. 3, pp. 276–290, Jun. 2010, doi: 10.1016/j.media.2010.01.003.
- [79] G. M. Treece and A. H. Gee, ‘Independent measurement of femoral cortical thickness and cortical bone density using clinical CT’, *Med. Image Anal.*, vol. 20, no. 1, pp. 249–264, Feb. 2015, doi: 10.1016/j.media.2014.11.012.
- [80] E. Schileo *et al.*, ‘An accurate estimation of bone density improves the accuracy of subject-specific finite element models’, *J. Biomech.*, vol. 41, no. 11, pp. 2483–2491, Aug. 2008, doi: 10.1016/j.jbiomech.2008.05.017.
- [81] C. Öhman *et al.*, ‘Compressive behaviour of child and adult cortical bone’, *Bone*, vol. 49, no. 4, pp. 769–776, Oct. 2011, doi: 10.1016/j.bone.2011.06.035.
- [82] R. P. Crawford, ‘Quantitative Computed Tomography-Based Finite Element Models of the Human Lumbar Vertebral Body: Effect of Element Size on Stiffness, Damage, and Fracture Strength Predictions’, *J. Biomech. Eng.*, vol. 125, no. 4, p. 434, Aug. 2003, doi: 10.1115/1.1589772.
- [83] X. Neil Dong and X. Edward Guo, ‘The dependence of transversely isotropic elasticity of human femoral cortical bone on porosity’, *J. Biomech.*, vol. 37, no. 8, pp. 1281–1287, Aug. 2004, doi: 10.1016/j.jbiomech.2003.12.011.
- [84] M. M. Panjabi *et al.*, ‘Thoracic human vertebrae. Quantitative three-dimensional anatomy’, *Spine*, vol. 16, no. 8, pp. 888–901, Aug. 1991.
- [85] T. M. Jackman, A. I. Hussein, A. M. Adams, K. K. Makhnejia, and E. F. Morgan, ‘Endplate deflection is a defining feature of vertebral fracture and is associated with properties of the underlying trabecular bone: ENDPLATE DEFLECTION AND VERTEBRAL FRACTURE’, *J. Orthop. Res.*, vol. 32, no. 7, pp. 880–886, Jul. 2014, doi: 10.1002/jor.22620.
- [86] Bernardini F., Mittleman J., Rushmeier H., Silva C, Taubin G., ‘The Ball-Pivoting Algorithm for Surface Reconstruction’, in *IEEE TRANSACTIONS ON VISUALIZATION AND COMPUTER GRAPHICS*, 1999.